University of Southampton Research Repository

ePrints Soton

Copyright © and Moral Rights for this thesis are retained by the author and/or other copyright owners. A copy can be downloaded for personal non-commercial research or study, without prior permission or charge. This thesis cannot be reproduced or quoted extensively from without first obtaining permission in writing from the copyright holder/s. The content must not be changed in any way or sold commercially in any format or medium without the formal permission of the copyright holders.

When referring to this work, full bibliographic details including the author, title, awarding institution and date of the thesis must be given e.g.

AUTHOR (year of submission) "Full thesis title", University of Southampton, name of the University School or Department, PhD Thesis, pagination

http://eprints.soton.ac.uk

UNIVERSITY OF SOUTHAMPTON

Ultrafast High Power Fiber Lasers and their Applications

by

Luis Alonso Vazquez Zuniga

A thesis submitted in partial fulfillment for the
degree of Doctor of Philosophy

in the
Faculty of Physical and Applied Sciences
Optoelectronics Research Centre

February 2012

UNIVERSITY OF SOUTHAMPTON

ABSTRACT

FACULTY OF PHYSICAL AND APPLIED SCIENCES
OPTOELECTRONICS RESEARCH CENTRE

Doctor of Philosophy

by Luis Alonso Vazquez Zuniga

In this thesis I report experimental studies toward developing versatile, compact, and reliable ultrafast sources in the 1.5 micron wavelength region, and their power scalability. The first part of the thesis reports on the development of a stable all-fiberized wavelength-tunable frequency-shifted feedback (FSF) picosecond laser. Stability of the passive mode-locking mechanism is achieved by combining the effects of nonlinear polarization evolution and a frequency shifting mechanism carried out by an acousto-optic modulator. The novel configuration generates pulses in the range of $\sim$ 34 to 66 ps, depending on the value of the frequency shift applied in the cavity. The cavity allows for continuous wavelength-tuning over 30 nm of the erbium gain bandwidth via a fiberized tunable filter. The stability of the laser cavity allows pulse analysis as a function of different parameters of the laser cavity. Additional extensive numerical analysis, combined with the experimental results, provide novel insights for understanding the dynamics of FSF lasers in the mode-locking regime, which have not been addressed in the literature before.

The second part of the thesis reports on the development of a versatile, stable, compact mode-locked fibre laser using nonlinear polarization evolution and a semiconductor saturable absorber mirror(SESAM). The novel cavity can generate pulses with widths between $\sim$ 2.7 and 11 ps over 25 nm of erbium gain bandwidth. This is achieved by integrating in the cavity state-of-the-art optical filters. The performance of this laser is compared to that of the FSF laser in terms of pulse energy, amplitude noise, timing jitter and power scaling.

The third part of the thesis reports on the direct amplification of a mode-locked $\sim$ 10 picosecond bandwidth-tunable laser source that I made by means of large-mode area (LMA) erbium-ytterbium co-doped and erbium-doped fibres. While cladding pumping amplification schemes have become a standard option for pulse amplification in the 1.5 μm region, core-pumped amplification in LMA erbium-doped fibres has been less studied. In this thesis, in addition to the amplification of picosecond pulses in an erbium-ytterbium co-doped fibre; I present a novel scheme that uses a hybrid co-propagation core-pumped (1480 nm) and counter-propagation cladding-pumped (980 nm) scheme, which compensates for the low cladding absorption at 980 nm of the erbium-doped fibre. Picosecond pulses are amplified up to 1.5 W with peak powers exceeding 11 kW.

The last part of this thesis reports on the study of a stable operating regime found in passive mode-locked lasers called noise-like pulses, which can generate broadband spectra directly from the main oscillator. Here, I report the record of a 135-nm bandwidth lineraly polarized noise-like pulse generation in an erbium-doped fibre laser by exploiting the birefringence of the cavity and the Raman gain of a highly nonlinear fibre (HNLF). Noise characterization of the source is carried out and compared to other commercial broadband sources in order to see its applicability in areas such as optical coherence tomography.

Contents

List of Figures

List of Tables

Nomenclature

α_k	Fibre absorption in dB/m
α_{loss}	Fibre loss coeffficient in dB/m
β_2	Group velocity dispersion parameter
β_3	Third order dispersion
$\Delta\lambda$	Laser signal bandwidth measured at FWHM
$\Delta\lambda_{BPF}$	Band-pass filter bandwidth measured at FWHM
E	Electric field
E_s	Soliton pulse energy
E_g	Gaussian pulse energy
efl	Effective focal length
Er^{3+}	Erbium ions
f_{AOM}	Driving frequency of the acousto-optic modulator
γ	Nonlinear coefficient
g_k	Fibre gain coefficient in dB/m
L_{EDF}	Erbium-doped fibre length
L_{smf}	Single mode fibre length
λ_c	Filter central wavelength
λ_p	Pump wavelength
ν_{BPF}	Band-pass filter bandwidth measured at FWHM
ν_c	Filter central frequency
P_{in}	Intracavity power
P_{out}	Output power
P_{pump}	Pump power
ϕ_{NL}	Nonlinear phase
ϕ_s	Soliton phase
$sech^2$	Hyperbolic-secant-squared pulse shape

List of Abbreviations

AOM	Acousto-Optic Modulator
ASE	Amplified Spontaneous Emission
CPA	Chirped Pulse Amplification
cw	Continuous-Wave
DCA	Digital Communication Analyzer
DCF	Double-Clad Fibre
DC-PCF	Double Clad-Photonic Crystal Fibre
DFB	Distributed Feedback
EDFA	Erbium Doped Fibre Amplifier
EFL	Effective Focal Length
FP	Fabry-P*é*rot
FSF	Frequency-Shifted Feedback
FBG	Fibre Bragg Grating
FRIP	Fibre Refractive Index Profile
FWHM	Full Width Half Maximum
GVD	Group Velocity Dispersion
LMA	Large Mode Area
MCVD	Modified Chemical Vapor Deposition
ML	Mode-Locked or Mode-Locking
NA	Numerical Aperture
NALM	Nonlinear Amplifying-Loop Mirror
NLSE	Nonlinear Schrödinger Equation
OCR	Output Coupling Ratio
PCF	Photonic Crystal Fibre
PD	Photodetector
PM	Polarisation Maintaining
RE	Rare-Earth
RIP	Refractive Index Profile
DBR	Distributed Bragg Reflector
SESAM	Semiconductor Saturable Absorber Mirror
SHG	Second Harmonic Generation
SPM	Self-Phase Modulation

TBP	Time Bandwidth Product

Acknowledgements

I would like to take this opportunity to thank my supervisor Professor Johan Nilsson and co-supervisor Dr. Yoonchan Jeong for their constant support and guidance during the course of my research work. I am particularly indebted to Dr. Yoonchan Jeong for introducing me to the field of fibre lasers and for his useful advices in the preparation of this thesis.

My special thanks go to Dr. Christophe Codemard for getting me started in the laboratory and for his valuable support and suggestions for my experiments. I am grateful to Dr. Shaif-ul-Alam, and Dr. Trevor Newson for sharing a vast amount of equipment with me (erbium-doped fibres, acousto-optic modulators, Raman laser, and the list goes on). I am also thankful to Dr. Morten Ibsen for providing the fibre Bragg gratings used in different experiments and for useful discussions on optoelectronics. My expression of gratitude also goes to Dr. Periklis Petropoulos and Dr. Francesca Parmigiani for sharing their autocorrelator and fast-photodetectors for my experiments. I would also like to extend my gratitude to my co-workers in the high power fibre laser group: Carl Farrell, Junhua Ji, and Gysbert van der Westhuizen, for their help, and support.

I would like to give a very special thanks to my friends and co-workers Dr. Mohammed Bilal, Dr. Ananth Subramanian, and Dr. Jedrzej Szelc for sharing with me the good and bad days of a postgraduate student life and providing me many enjoyable times.

I want to express my gratitude to my sponsor, CONACyT (National Council for Science and Technology of Mexico) for providing me with a scholarship to pursue this degree at the Optoelectronics Research Centre.

A big thanks to all my friends in the UK and specially the ones in Southampton for providing me homely atmosphere and support.

A very special thanks to my family Beatriz, Jose Luis and Yuriria for their love, support, and encouragement.

Finally, my sincere thank you to my habibi Lucy, for sharing with me her pure and endless happiness.

To my grandmother Elvira, and
my parents Beatriz and Jose Luis.

Chapter 1

Introduction

In this thesis I report experimental studies toward developing versatile, compact, low cost, and reliable ultrafast sources in the 1.5 micron region and their power scalability. In addition I also report on the study of a stable operating regime found on passive mode-locked lasers called noise-like pulses, which can generate broadband spectra directly from the main oscillator.

1.1 Motivations

Over the last decade tremendous progress in generating picosecond and femtosecond pulses using solid state lasers has been done. These pulsed laser systems have revolutionized many areas of science and technology, finding widespread use in applications such as micromachining, optical sampling, metrology, biological imaging, nonlinear frequency conversion, terahertz generation, etc. However, the inherent problems associated with solid state laser systems such as long-term stability, thermal management, beam quality and compactness have forced the search of alternative laser systems. One such alternative rely on Rare-Earth (RE) doped fibre systems. Optical fibres offer practical advantages such as high single pass gain, power independent beam quality (when using single mode fibres), excellent heat dissipation and high optical efficiencies. Furthermore, with the introduction of cladding pumping technology, and the development of high power and low brightness pump laser diodes, nowadays, it is possible to scale the average powers of these systems to the kW level [10], [11]. All these features have motivated substantial research in the area of ultrafast fibre-based lasers and amplifiers, especially for Ytterbium (Yb^{3+})-based fibre technology. However, despite the important progress done in this area, fibre sources are still behind their solid state counterparts in key performance parameters like: pulse energy, pulse duration and peak powers, limiting their impact in different applications. Therefore the development of high-power ultrafast fibre based sources is still of great interest.

Yb-doped fibre based systems have led the way in the development of high-power ultrafast fibre based sources over the last years due to their excellent efficiency, which can go over 80% when pumped at $\sim$ 975 nm and their small quantum defect [12]. This characteristic is of great advantage over Nd^{3+} or Er^{3+}-doped fibre lasers, as well as Er^{3+}/Yb^{3+}co-doped fibres. Yet, Er^{3+}-doped fibres offers other advantages compared to Yb^{3+} like the operation in the eye-safe spectral window near 1.5 μm which is suitable for a number of industrial sensing, medical and nonlinear optics applications (i.e., coherent infrared generation). Furthermore, operation at these wavelengths is compatible with a multitude of photonics devices used for telecommunication systems. Additional profits to work at these wavelengths include the cost effectiveness that is a priority for this research. For high-power fibre systems operating in the 1.5 μm region, Er^{3+}/Yb^{3+} co-doped fibres present better optical properties than Er^{3+}-doped fibre [13], [14]. Er^{3+}/Yb^{3+}co-doped fibres present a larger absorption cross-section than Er^{3+} around 975 nm and higher Er^{3+}-doping concentration. These properties enable strong core absorption and gain, which is essential for high-power fibre systems. Nevertheless, Er^{3+}/Yb^{3+}co-doped fibres presents more challenges in controlling the fibre refractive index profile (RIP) during the fabrication process. Such difficulties arise from the addition of phosphorus to the modified chemical vapor deposition (MCVD) fibre fabrication process to enhance the energy transfer of Yb^{3+} to Er^{3+}. Phosphorus presents a highly volatile behaviour during the collapse phase of the MCVD process, reducing its presence in the fibre core. This reduction of phosphorus causes a change in the refractive index, which is commonly observed as a central dip in the fibre core, limiting the formation of diffracted-limited beams with LMA fibres. In addition to this, Er^{3+}/Yb^{3+} co-doped fibres can decrease their efficiency at high pump power, due to spurious emissions in the Yb^{3+}-band and to excessive thermal load due to the quantum defect [15, 16]. Fabrication of Er^{3+} fibres does not present such difficulties, and step index profiles are possible to generate diffraction-limited beams, even with very large mode area (VLMA) fibres [17]. However, as mentioned above, due to the low pump absorption, it is necessary to increase the absorption of the fibre by increasing its length. Still, the development of Raman lasers at 1480 nm with output powers up to 10 W delivered in single mode fibres [18], has facilitated to core pump LMA Er^{3+} fibres, hence, allowing to reduce the fibre length and, therefore, the onset of nonlinearities. In addition, this configuration helps reducing the problem of large quantum defect and thermal loading observed in Er^{3+}/Yb^{3+} co-doped fibres [2].

A common challenge in the development of high power ultrafast fibre amplifier systems resides in avoiding pulse distortions generated by fibre nonlinearities. Fibre nonlinearities are boosted in optical fibres due to the large product of intensity and interaction length inside the small fibre core. Chirped pulse amplification (CPA) is the most common technique to reduce peak power in fibres and consequently reduce nonlinear effects. This method is well suited for increasing the energy of the pulses but typically involves complex optical arrangements. Therefore, in practice the direct amplification of pulses is preferable. Different techniques based on the enlargement of the mode-field diameter and on the fibre length, are now well established to reduce nonlinearities in fibre amplifier systems. Large-mode area (LMA), Photonic Crystal Fibres (PCF) and Double Clad-Photonic Crystal Fibres (DC-PCF) offer a significant potential for power or energy scaling. CPA systems together with these fibre technologies have enabled amplification of femtosecond pulse trains to very high average powers of several hundred watts and hundreds of megawatt peak power [19].

Progress in ultrafast pulse amplification goes together with the availability of the sources to generate ultrafast pulses. In most of the cases, the sources are solid state or fibre lasers using semiconductor saturable-absorbers (SESAM) or Nonlinear Polarization Rotation (NPR) as passive mode-locking (ML) mechanisms. However, for the first part of this research work, it was decided to implement a frequency shifted feedback (FSF) mechanism as an interesting alternative to the use of SESAM or NPR to generate picosecond pulses. The theory behind these lasers is similar to that used for soliton communication systems making use of sliding-frequency guiding filters to increase the losses seen by the c.w. light in comparison to the losses seen by a pulse. In this way, an acousto-optic modulator (AOM) acts as a saturable absorber allowing the laser to emit mode-locked pulses. Although a main disadvantage for this technique is the use of RF sources to drive the AOM, the modulation of the AOM through the RF can lead to generate controlled Q-switched mode-locking to increase the pulse peak power generated by the source. Therefore, the source can offer versatile solutions for different applications.

1.2 Thesis synopsis

Chapter 2 is intended to provide the background theory for Er^{3+}-doped and Er^{3+}/Yb^{3+} co-doped fibre technology as well as the basic theory of nonlinear effects for pulse propagation in optical fibres. Chapter 3 gives a review of passive mode-locking techniques, including the different cavity configurations to generate high energy pulses. Chapter 4 gives an introduction of the operating principles of frequency-shifted feedback (FSF) lasers operating in the mode-locking regime. In addition, a brief summary of former theoretical and experimental works is given. This Chapter also presents the experimental results of two all-fibre Er^{3+}-doped laser configurations using an acousto-optic modulator (AOM) as a frequency shifter inside the cavity. Experimental results obtained in this chapter, in addition to the numerical simulations of Chapter 5, provide a better understanding of the dynamics of FSF lasers in the ML regime, which has not been addressed in previous works. The study of the characteristics of the signal allows enumerating the advantages and disadvantages of this technique for mode-locking pulses and its possible applications as versatile pulse sources. Chapter 5 present numerical simulation studies on pulse formation in an Er^{3+}-doped frequency-shifted feedback (FSF) fibre laser in a ring cavity configuration. In particular, I focus on the development and behaviour of the pulse spectra and its relation with its pulse shape in the time domain for different parameters of the laser cavity. The numerical results shown here are compared with the experimental data of Chapter 4 allowing a better understanding of the formation and asymmetry of the optical pulses presented in FSF lasers. In Chapter 6 I present the characterization of three mode-locked fibre lasers based on a semiconductor saturable absorber mirror (SESAM), operating at 1.5 μm. The simple, compact and stable design of the cavity allowed me, by simply changing the intracavity filter, to generate either femtosecond or wavelength tunable picosecond pulses. Results obtained with these lasers are compared with the ones shown in Chapter 4 for a mode-locked FSF laser. In Chapter 7, I describe the implementation and characterization of two master oscillator power amplifiers (MOPAs) used in the direct amplification of the 10 picosecond bandwidth-tunable laser source described in Section 6.3.2. Two large mode area (LMA) fibres were tested for the high power amplifier stage and their performance was compared in terms of efficiency and beam quality. The first fibre tested was a home-made double-clad Er^{3+}/Yb^{3+} co-doped LMA fibre with a core diameter of 27 μm, while the second one is a commercial double-cladding Er^{3+}-doped LMA fibre with a core diameter of 35 μm. In this chapter a hybrid pumping configuration is proposed in order to compensate for the low cladding absorption at 980 nm of the LMA Er^{3+}-doped fibre. In Chapter 8 I propose and characterize a linearly-polarized Er^{3+}-doped fibre ring laser generating 135-nm bandwidth picosecond noise-like pulses with excellent spectral power stability. The pulse energy and width are readily reconfigurable via controlling the laser cavity finesse and/or pumping power. I also carried out RIN measurements of the source and compare it with a commercial supercontinuum source. Finally, I summarize the conclusions of this thesis and propose future research directions of the works described here.

Chapter 2

Erbium-doped fibre technology and nonlinear effects in optical fibres

The work presented in this thesis is focussed on developing ultra-fast optical sources operating in the eye-safe wavelengths around 1550 nm. To this end, Er^{3+}-doped fibres and Er^{3+}/Yb^{3+} co-doped fibres are used as gain media for the generation and/or amplification of ultra-fast pulses in this spectral region. This Chapter is intended to provide the background theory for Er^{3+}-doped and Er^{3+}/Yb^{3+} co-doped fibre technology as well as the basic theory of nonlinear effects for pulse propagation in optical fibres. This Chapter is structured as follow: Section 2.2 and 2.3 describe the principles and spectroscopy of Er^{3+}-doped and Er^{3+}/Yb^{3+} co-doped fibres. Section 2.4 describe the different fibre technologies for pulse amplification and techniques to achieve single mode or low order mode operation in high power fibre amplifiers. Finally, section 2.5 reviews the basic theory for pulse propagation in fibres and the nonlinear phenomena related to it.

2.1 Introduction

The invention of the first fibre laser and amplifier is attributed to Elias Snitzer for his works published in the early 60s [20–22]. Regarding his fibre laser work [20], a barium crown glass was doped with Neodymium Nd^{3+} , and transversally pumped with a flash lamp. The laser emitted a number of spatially multimode sharp lines centred at around 1060 nm, however due to the transverse pumping scheme, the laser had a low pumping efficiency. The development in forthcoming years of laser sources allowed experiments with longitudinal pump schemes in fibre lasers improving the pumping efficiency [23]. A renewed interest in fibre lasers came in the mid-80s, when the group of D.N. Payne and co-workers at Southampton University developed an extended modified chemical vapour deposition (MCVD) process to fabricate low-loss optical fibres containing rare-earth ions [24]. The novel process allowed pumping an active fibre with low power and achieving, at the same time, high signal gain [25]. Further research with this fibre fabrication technique led to the first erbium doped fibre amplifier (EDFA) in 1987 [26]. Since then, fibre laser technology has been constantly improving in terms of power scalability [10, 27, 28] and wavelength operating regime [1, 29].

Glass-based fibres doped with rare-earth ions offer several advantages over their counterparts "bulk" solid-state lasers. Such advantages come as a result of the host glass and waveguide properties of fibre lasers. Regarding the former, fused silica offers a wide range of good optical transparency, with low absorption and scattering losses in the near-infrared region. Therefore, silica fibres offer a good amplification medium with low losses. In addition, silica glass can offer wider spectral lasing transitions compared to their crystal-host counterparts, allowing for ultra-short pulse amplification [2]. The high thermal damage threshold of silica glass is also a feature which makes it an excellent candidate for high power fibre amplifiers. Although silica glass is not a good heat conductor [30], this is compensated by the high surface area to volume ratio of the fibre, therefore, allowing for easier heat dissipation and thermal management.

The waveguide nature of fibre lasers, also offers advantages such as power independent beam quality (in single mode fibres), and high single pass gain, which makes them great contenders for power scalability. Furthermore, advances in fibre splice technology can provide all-fiberized laser systems, making them compact, alignment-free and robust. All these attributes have made fibre lasers to grow in the commercial market and gain space in applications where other laser types dominate the market.

2.2 Principles of Erbium-doped silica fibres

Since the invention of the first erbium-doped fibre amplifier (EDFA) at the University of Southampton in 1987 [26], Er^{3+}-doped fibre technology gained considerable attention to satisfy the demands of the telecommunication industry. Although most of the works carried out, in the beginning, for Er^{3+}-doped fibres were related to telecom applications, in the last 10 years research has proved the potential of these lasers for various applications ranging from industrial applications (drilling, cutting, defence) to medicine (optical ranging, optical coherence tomography, microscopy, etc) [2, 18].

In the following subsections I give a summary of the basic physics and principles of operation of EDF technology which forms the base of my research in this Thesis.

2.2.1 Spectroscopy of Erbium-doped silica fibres

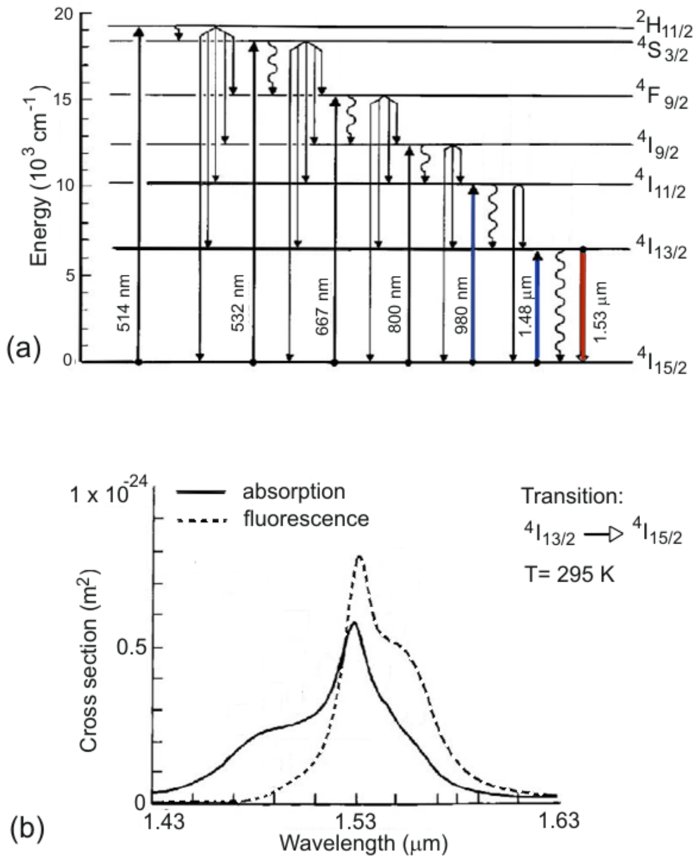

Figure 2.1: (a) Energy level diagram of Er^{3+}:glass. Upward arrows show the pump absorptions bands, while downward arrows show the radiative and nonradiative transitions. (b) Absorption and emission cross section spectra for an aluminosilicate fibre for the transition $^4I_{15/2} \rightarrow {}^4I_{13/2}$ [1].

Er^{3+} is a rare-earth ion that belongs to the lanthanides group, which are characterised by the filling of the $4f$ electronic shell. In the lanthanides group, the $4f$ shell is shielded from the host lattice by the optically passive outer electronic shells [1]. Therefore, interactions between energy levels are relatively insensitive to the host lattice. Electron transitions between the $4f$ states are responsible for the observed infrared (IR) and visible optical spectra of Er^{3+}. Fig. 2.1 (a) shows the energy level structure of Er^{3+} with the optical transitions of the $4f$ shell. The most common laser transition used for EDFA is the $^4I_{13/2} \rightarrow {}^4I_{15/2}$, which correspond to the wavelength region around 1530 nm to 1600 nm. This transition is 100% radiative and has a fluorescence lifetime of approximately 10 ms. For pumping the active medium, two laser transitions are commonly used. The first one is the $^4I_{15/2} \rightarrow {}^4I_{11/2}$ transition with a wavelength $\sim$ 980 nm. The second one is the in-band pumping transition $^4I_{15/2} \rightarrow {}^4I_{13/2}$ with wavelength $\sim$ 1480 nm. The relaxation process between the $^2H_{11/2}$ and $^4I_{13/2}$ energy levels presents fast (microseconds) nonradiative decay. Therefore, EDFAs can be described as a quasithree-level level system.

Figure 2.1 (b) shows the absorption and emission cross-sections of Er^{3+} for an aluminosilicate fibre for the transition $^4I_{15/2} \rightarrow {}^4I_{13/2}$ [1]. The absorption band in the 1450 to 1530 nm region offers the possibility to achieve high power efficiency due to the proximity between the pump and the signal wavelengths (low quantum defect). Efficiencies of $\sim$ 90% with respect to absorbed pump power can be experimentally achieved [2]. Yet, stimulated emission by pump light limits the achievable excitation level, and maximum gain occurs at longer wavelengths. On the other hand, pumping in the 980 nm region, gives low power efficiency due to the large quantum defect. Still, the quick non-radiative transfer from the $^4I_{11/2}$ manifold to the upper laser level $^4I_{13/2}$ can generate high excitation levels to achieve high gain efficiency (10 dB/mW) and low noise figures [31].

2.3 Principles of Er/Yb co-doped silica fibres

A way for power scaling fibre lasers uses double-cladding configurations [2] to facilitate side-pumping with high power laser diodes with large NA. The low pump absorption coefficient in pure Er $^{3+}$-doped fibres impose a limitation for efficient pump absorption and therefore power scaling. To overcome this issue, co-doping techniques have been invented to improve the low pump absorption of Er $^{3+}$-doped fibres.

2.3.1 Spectroscopy of Er/Yb co-doped silica fibres

Co-doping of Yb^{3+} ions, added to the core as a synthesizer in phosphosilicate double-clad fibres, is the standard approach for power-scaling EDFLs [32, 33]. In Er $^{3+}$/ Yb^{3+} co-doped fibres pump light is absorbed by the Yb^{3+} ions through the transition $^4F_{7/2} \rightarrow {}^4F_{5/2}$, which covers the 910 to 980 nm wavelength region. The Er^{3+} are later excited through the non-radiative transfer of energy from the Yb^{3+} ions (See. Fig. 2.2 (a)). The absorption and emission cross-section spectra of an in-house fabricated phosphosilicate Er^{3+}/Yb^{3+} co-doped silica fibre (identification number: F195-LF59) is shown in Fig. 2.2 (b). The substantial increment in the absorption cross-section in the 910 to 980 nm wavelength region due to the Yb^{3+} ions (typically 10 to 20 times larger than that of Er^{3+} ions), allows one to choose a wider choice of high-power laser diodes within this spectral region. Typically, efficiencies for cladding-pumped Er^{3+}/ Yb^{3+} co-doped fibre lasers can reach between $\sim$ 40% and 45%, which can decrease at high pump powers due to spurious Yb^{3+} emission between 1000 nm and 1100 nm, excessive thermal load, and inefficient transfer between the Yb^{3+} ions and Er^{3+} ions [34].

---

[1] Note that absorption and emission cross-section spectra vary depending on the fibre composition

[2] Section 2.4 gives a summary of fibre technology, including double-clad fibres.

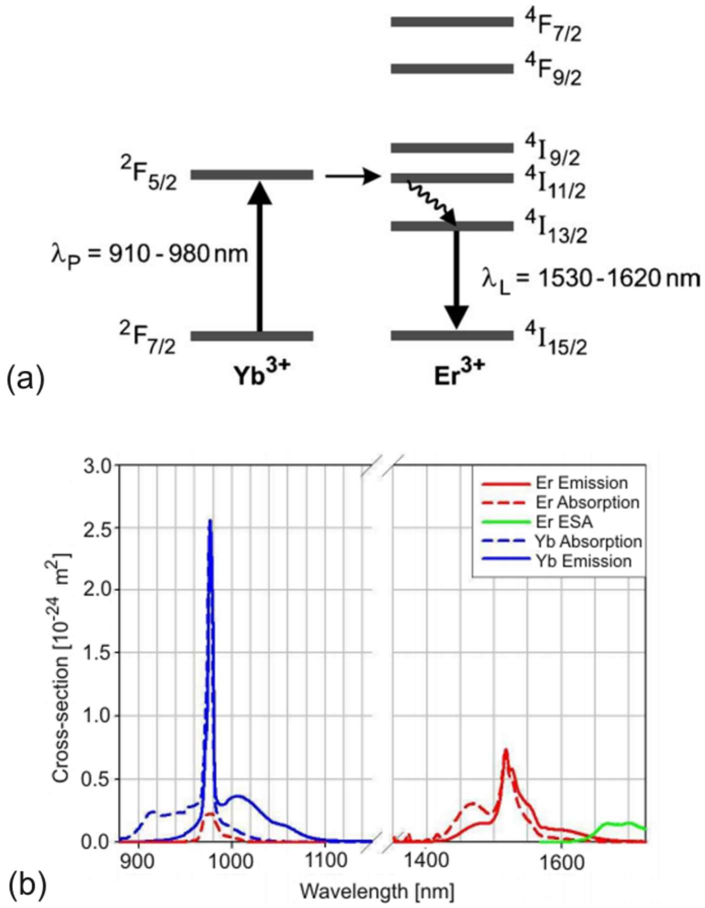

FIGURE 2.2: (a) Energy level diagram of Er^{3+}/Yb^{3+} co-doped silica [2]. (b) Absorption and emission cross section spectra for a phosphosilicate Er^{3+}/Yb^{3+} co-doped silica fibre [3].

2.4 Fibre technology

In this thesis, there are two types of pumping configurations used in the experiments: core and cladding pumping. In the next subsections I will describe briefly the properties and applications of each configuration.

2.4.1 Core-pumped single-mode fibre amplifier

Core-pumped fibre amplifiers are formed of active single-mode fibres that can generate diffraction-limited beam outputs. In these configurations, pump and signal light are guided in the core of the fibre. Therefore, pump sources are restricted to those with single mode output, which mainly are low power (hundreds of miliwatt). Core-pumped amplifiers present several advantages such as low-noise operation, high stability, and robustness. For this reason, they are often used as pre-amplifiers in fibre-based master oscillation power amplifier (MOPA) configurations. The amplification system described in Chapter 7 includes a core-pump amplifier in its first amplification stage. The fibre used for this pre-amplifier has an NA of 0.23, with a mode field diameter MFD = 5.5 μm and a peak absorption of 37.5 dB/m at 1530 nm. The high absorption coefficient of the fibre is useful for pulse amplification (in this case, picosecond pulses) because it allows for shorter fibres that avoid excessive growth of nonlinear effects.

2.4.2 Cladding-pumped fibre amplifiers

Double-clad rare-earth fibres have proven to be a solution to power-scale fibre lasers. Double-clad fibres (DCF) are formed of an active singlemode (or multimode) core, where the signal light is guided. The core is surrounded by an inner cladding with lower-refractive index where pump light propagates. The pump light is able to propagate in this region due to a second cladding (outer cladding) with lower refractive index that surrounds the inner cladding. In a typical DCF, the NA of the core is low ($\sim$ 0.1) while the NA between the inner cladding and the outer cladding is high ($\sim$ 0.6), thus facilitating the efficient launching of light from multimode high-power lasers (see Fig. 2.3). Therefore, one of the main advantages of DCFs is that it allows diffraction-limited output signals from multimode pump lasers with poor beam quality.

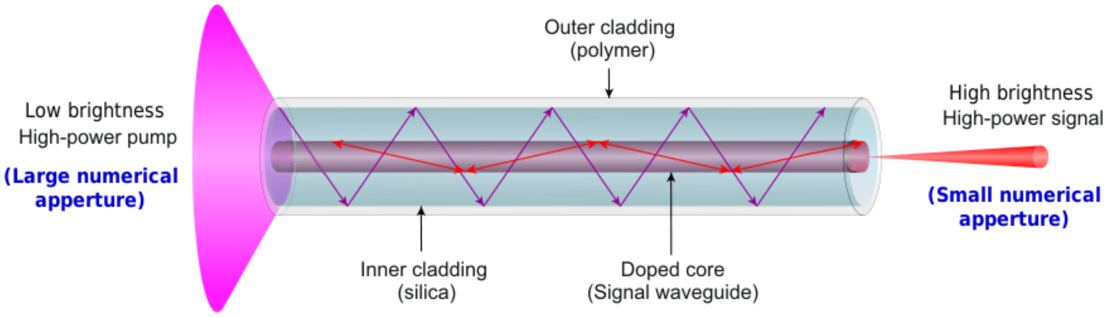

FIGURE 2.3: Schematic of a double-clad fibre.

Pump absorption in DCFs is relatively low compared to core-pump fibres. For example, the large mode area (LMA) Er^{3+} fibre used in Chapter 7 has an absorption coefficient of 5 dB/m at 1530 nm. Therefore, efficient pump absorption per unit length is a prerequisite to obtain good performance in double-clad fibre amplifier systems. Different techniques have been developed in order to improve the pump absorption in fibres. One of these techniques consists of breaking the axial symmetry of the core and the inner cladding to avoid helical rays (see. Fig. 2.4 (a)). Helical rays propagate in the inner cladding in spiral trajectories without crossing the fibre core. As a result, helical rays propagate practically without being absorbed, reducing the gain and power efficiency of the amplifier. Figs. 2.4 (b)-(e) show various designs of DCFs with off-centred core and non-circular claddings. The LMA Er^{3+}/Yb^{3+} co-doped and LMA Er^{3+}-doped fibre use in Chapter 7 for the

MOPA configuration have D-shape and flower shape inner claddings, respectively.

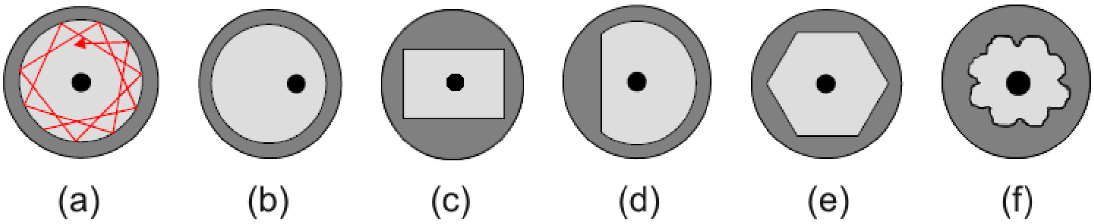

FIGURE 2.4: Various designs of double-clad fibres with different inner cladding shapes to break the axial symmetry of the waveguide: (a) circular (helical rays are represented by the red arrows), (b) off-centred core, (c) rectangular-shaped cladding, (d) D-shaped cladding, (f) hexagonal-shaped cladding, and (e) flower-shaped cladding

In DCFs the small-signal cladding pumped fibre absorption α_{clad} can be approximated by [35]:

$$\alpha_{clad} = \alpha_{core} \cdot A_{core}/A_{clad}, \tag{2.1}$$

where α_{core} is the core absorption, A_{core}, A_{clad} are the core and cladding areas, respectively. Therefore, the efficiency of pump absorption in DCFs can be improved by either increasing the doping level in the fibre core or by scaling the core/clad area ratio of the fibre. Nevertheless, these two options are restricted by factors such as quenching (especially for Er^{3+}-doped fibres) or background loss. Regarding the former, efficiency in Er^{3+}-doped fibres drops at high Er^{3+} ions concentrations due to pair-induced quenching [36, 37]. The typical concentration limit for aluminosilicate Er^{3+}-doped fibres is $\sim$ 1000 ppm [37]. In the case of Er^{3+}/Yb^{3+} co-doped fibres, higher concentration of Yb^{3+} ions is possible without affecting the laser efficiency. However, background loss in these fibres is generally higher than in Er^{3+}-doped fibres. Typical values for background loss in Er^{3+}/Yb^{3+} co-doped fibres lie between 100 to 200 dB/km regardless of Er^{3+} concentration [3]. Therefore, to avoid degradation of the fibre efficiency, it is convenient to keep the background signal loss below $\sim$ 1 dB [3]. For example, for a fibre with a background signal loss of 100 dB/km, the active fibre length should be no more than 10 metres. Yet, the fibre length should still provide enough pump absorption.

Scaling the core to cladding area ratio of the DCFs is another method to increase the pump absorption efficiency of the fibre. This is usually carried out by increasing the core diameter and reducing at the same time the core NA in order to keep the V-parameter relatively small. Yet, bending losses in a single mode fibre place an upper limit on the size of the core area. In the case of multimode fibres, larger areas worsen the quality of the fundamental beam [38]. For optimum cladding pump absorption and efficient pump launching, fibre fabricators design fibres with cross-sectional areas with ratios of at least ten. The Er^{3+}/Yb^{3+} co-doped and Er^{3+}-doped fibres used in Chapter 6 have area ratios of 44 and 12, respectively.

A good launching efficiency into the inner cladding of the DCF will also determine the performance of the DCF laser or amplifier. Different techniques have been proposed to maximize the launching efficiency of the pump signal, and are divided in two categories depending on the position of the launching point along the DCF: end-pumping and side-pumping. In end-pumping techniques, pump light is injected along the laser beam, while in side-pumping techniques, light is pumped into the inner cladding without access to the fibre ends. This can be done with V-shaped grooves located at different locations along the active fibre or with GT-wave fibres [39] where the pump light is launched into passive multimode pump fibres which are closely bundled to a signal fibre with an active core. The fibres have similar refractive indices and are surrounded with a low index coating, allowing the pump light to couple in the active fibre. For end-pumping, tapered fibre bundles (TFP) [40] and free-space end-pumping are the most common techniques for injecting light into DCFs. The MOPA configuration described in Chapter 7 uses a free-space end-pumping technique to inject light into the active DCFs. This technique was chosen due to its simplicity and high efficiency. Furthermore, the fibre pigtailed output of the pump diode contributed to avoid complicated optics for coupling light into the DCFs.

2.5 Nonlinear effects in optical fibres

The advantages offered by the waveguide geometry of fibre lasers, in terms of power-scalability (tight beam confinement and long interaction lengths with the gain media) enhance at the same time nonlinear effects. Nonlinear effects in optical fibres originate from the third-order susceptibility $\chi^{(3)}$ [41] and can be classified in two groups. The first one includes effects related to the intensity dependence of the refractive index (Kerr nonlinearity). Phenomena such as self-phase modulation (SPM), cross-phase modulation (XPM) and four-wave-mixing (FWM) belong to this group. The second group includes effects resulting from stimulated inelastic scattering (transfer of energy to the nonlinear medium). Phenomena such as stimulated Raman scattering (SRS), and stimulated Brillouin scattering (SBS) belong to this second group. All nonlinearities commented above scale with intensity and interaction length. Therefore, they impose important limitations to pulse propagation and amplification in optical fibres. In this section I give a brief summary of such nonlinearities in the presence of pulse propagation in dispersive media.

2.5.1 Pulse-propagation equation

The basic equation describing the propagation of pulses in optical fibres is the nonlinear Schrödinger equation (NLSE) and it is given by [5]:

$$\frac{\partial A}{\partial z} = -\frac{\alpha_{loss}}{2} A - \beta_1 \frac{\partial A}{\partial t} - \frac{i}{2}\beta_2 \frac{\partial^2 A}{\partial t^2} + \frac{1}{6}\beta_3 \frac{\partial^3 A}{\partial t^3} + i\gamma \left|A\right|^2 A \tag{2.2}$$

where A denotes the slowly-varying complex-envelope of the optical field propagating in the z direction at a time t, β_1 is the inverse group velocity υ_g (rate of change of time with respect to distance), β_2 is the group-velocity dispersion (GVD) coefficient, β_3 is the third order dispersion coefficient, α_{loss} is the fiber loss, and γ is the nonlinear parameter of the fibre at the carrier angular frequency ω_0.

Equation 2.2 can be simplified by using a frame of reference moving with the pulse at the group velocity $\upsilon_g = 1/\beta_1$. Furthermore, for picosecond pulses, dispersive effects higher than second order can be neglected. Assigning $T = t - \beta_1 z$, Eq. 2.2 takes the form:

$$\frac{\partial A}{\partial z} = -\frac{\alpha_{loss}}{2} A - \frac{i}{2}\beta_2 \frac{\partial^2 A}{\partial T^2} + i\gamma \left|A\right|^2 A. \tag{2.3}$$

The nonlinear parameter in Eq. 2.2 and 2.3 is defined as

$$\gamma = \frac{\omega_0 n_2(\omega_0)}{c A_{eff}} \tag{2.4}$$

where n_2 is the nonlinear-index coefficient, c the speed of light and A_{eff} is the effective mode area defined as:

$$A_{eff} = \frac{\left[\int\int \left|F(x,y,\omega_0)\right|^2 dxdy\right]^2}{\int\int \left|F(x,y,\omega_0)\right|^4 dxdy} \tag{2.5}$$

where $F(x, y, \omega_0)$ is the spatial distribution of the fibre mode.

Equation 2.3 is mainly governed by the dispersion parameter β_2 and the nonlinear effects represented by γ. For analysis of pulse propagation, it is always useful to identify which of the two parameters governs pulse evolution in an optical fibre. For an input pulse with peak power P_0 and pulse width T_0, it is possible to define two length scale parameters: the dispersion length $L_D = T_0^2/\left|\beta_2\right|$, and the nonlinear length $L_{NL} = (\gamma P_0)^{-1}$. A dispersion-dominant regime occurs whenever $L_D/L_{NL} << 1$, and a nonlinearity-dominant regime is applicable whenever $L_D/L_{NL} >> 1$.

2.5.2 Group-velocity dispersion

In the dispersion-dominant regime it is possible to neglect the nonlinear parameter by setting $\gamma = 0$ in Eq.2.3. If fibre loss is also neglected Eq. 2.3 takes the form:

$$\frac{\partial A}{\partial z} = -\frac{i}{2}\beta_2 \frac{\partial^2 A}{\partial T^2}. \tag{2.6}$$

Eq. 2.6 can be solved in the frequency domain and its general solution is:

$$\tilde{U}(z,\omega) = \tilde{U}(0,\omega)e^{-i\beta_2\omega^2 z/2} \tag{2.7}$$

where U is the normalized amplitude given by $U = A/P_0^{1/2}$. The form of the general solution shows that the dispersive term does not add new frequency components but just rearranges the phase relations among existing frequency components [41]. Considering an unchirped Gaussian pulse with amplitude

$$U(0,T) = exp(-\frac{T^2}{2T_0^2}) \tag{2.8}$$

where T_0 is related to the full width at half maximum (FWHM) of the pulse by $T_{FWHM} = 2(ln2)^{1/2}T_0$. The amplitude evolution of the pulse along the fibre is given by [41]

$$U(z,T) = \frac{T_0}{\sqrt{T_0^2 - i\beta_2 z}} exp\left(-\frac{T^2}{2(T_0^2 - i\beta_2 z)}\right) \tag{2.9}$$

Eq. 2.9 shows that the Gaussian pulse maintains its shape but its width changes with distance. Furthermore, the transmitted pulse acquires a chirp as it propagates along the fibre. For the Gaussian pulse, the phase evolution at any point in the fibre is given by

$$\phi(z,T) = -\frac{sgn(\beta_2)(z/L_D)T^2}{1+(z/L_D)^2T_0^2} + \frac{1}{2}tan^{-1}\left(\frac{z}{L_D}\right) \tag{2.10}$$

Equation 2.10 shows a time dependence of the pulse phase, whose time derivative imposes a linear chirp across the pulse and is given by

$$\delta\omega(T) = -\frac{\partial\phi}{\partial T} = \frac{sgn(\beta_2)(2z/L_D)T}{1+(z/L_D)^2T_0^2} \tag{2.11}$$

The chirp $\delta\omega(T)$ depends on the sign of β_2. In the normal dispersion regime ($\beta_2 > 0$), the pulse will be upchirped, which means that the leading edge of the pulse is red-shifted while the trailing edge of the pulse is blue-shifted. The opposite occurs in the anomalous dispersion regime ($\beta_2 < 0$).

2.5.3 Self-phase modulation

In the nonlinearity dominated regime, the dispersion term in Eq. 2.3 is set to $\beta_2 = 0$:

$$\frac{\partial U}{\partial z} = \frac{ie^{-\alpha_{loss} z}}{L_{NL}} |U|^2 U, \tag{2.12}$$

The general solution for Eq.2.12 is given by

$$U(L, T) = U(0, T) exp \left[i\phi_{NL}(L, T) \right] \tag{2.13}$$

where $U(0, T)$ is the slowly-varying field amplitude at position $z = 0$ and $\phi_{NL}(L, T)$ is the nonlinear phase shift defined as: $\phi_{NL}(L, T) = |U(0, T)|^2 \left(L_{eff} n_2 k P_0 / A_{eff} \right)$, where A_{eff} is the effective area defined in Eq. 2.5, $k = 2\pi/\lambda$, and L_{eff} is the effective length defined as $L_{eff} = \left[1 - exp(-\alpha_{loss/gain} L) \right] / \alpha_{loss/gain}$; the subscripts represent loss or gain of the fibre of length L. Equation 2.13 shows that SPM induces an intensity dependent phase change across the pulse that increases with the length of the fibre and pulse intensity. The time dependence of $\phi_{NL}(L, T)$ leads to a broadening of the pulse spectrum and to a frequency chirp given by:

$$\delta\omega(T) = -\frac{\partial \phi_{NL}}{\partial T} = -\frac{L_{eff} n_2 k P_0}{A_{eff}} \frac{\partial}{\partial T} |U(0, T)|^2 \tag{2.14}$$

2.5.4 Stimulated Raman scattering

Stimulated Raman scattering (SRS) is related to the transfer of a small fraction of power from an optical field to another field with a frequency downshift determined by the vibrational mode of the medium [41]. SRS occurs when a pump beam is sufficiently intense (Raman threshold) to generate a frequency-shifted radiation called the Stokes wave. Although SRS can be useful to design Raman based fibre amplifiers and lasers, it can also impose limitations in pulse amplification at high peak powers. Therefore, it is important to understand and calculate the Raman threshold with the parameters of the amplification systems used in Chapter 6, in order to avoid the onset of SRS.

An important parameter to understand the behaviour of SRS is the Raman gain coefficient g_R, whose spectrum is shown in Fig. 2.5. The graphic shows the measurement of g_R as a function of the frequency shift between the Stokes wave and the pump light for fused silica with a pump light at 1 μm. The maximum gain of the Raman spectrum is $g_R \sim 1\text{x}10^{-13}$ m/W and is located at a frequency shift of $\sim$ 13.3 THz. In the 1550 nm wavelength, this shift corresponds to a wavelength shift of $\sim$ 105 nm.

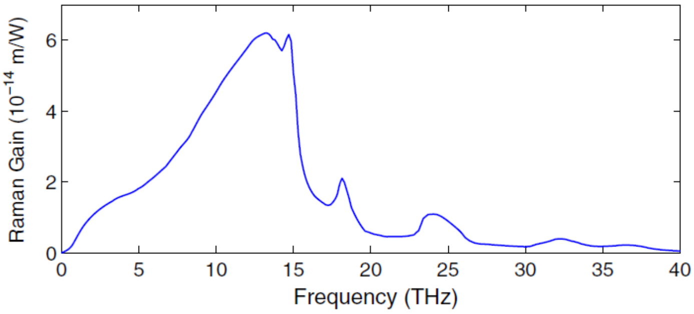

FIGURE 2.5: Raman gain spectrum of silica fibres [4].

The input power at which the Stokes power becomes equal to the pump power at the fibre output is known as the Raman threshold or critical power. It can be calculated by analysing the interaction between the pump and the Stokes signals represented by a set of two coupled equations:

$$\frac{\partial I_s}{\partial z} = g_R I_p I_s - \alpha_s I_s, \tag{2.15}$$

$$\frac{\partial I_p}{\partial z} = -\frac{\omega_p}{\omega_s} g_R I_p I_s - \alpha_p I_p, \tag{2.16}$$

where I_s and I_p are the Stokes and the pump intensities, respectively, g_r is the Raman gain coefficient, and α_s and α_p are the fibre losses at the Stokes and pump frequency, respectively. Solving the above equations and without considering pump depletion, the critical input pump power to reach the Raman threshold is given by [41]

$$\frac{g_R P_0^{cr} L_{eff}}{A_{eff}} \approx 16. \tag{2.17}$$

Equation 2.17 shows that SRS is proportional to the effective length of the active fibre and inversely proportionally to the fibre effective area. Therefore, a way of reducing the onset of SRS is by reducing the fibre length or increasing the core area of the fibre.

2.6 Conclusions

In this Chapter, I presented the background theory to understand the performance of Er^{3+}-doped and Er^{3+}/Yb^{3+} co-doped fibre technology. The concepts of core-pumped and cladding-pumped optical fibre amplifiers were also discussed. In particular, the advantages and disadvantages of DCF technology for power-scalability are highlighted. The advantages offered by the waveguide geometry of fibre lasers in terms of power-scalability, enhance at the same time nonlinear effects, which are detrimental for the laser signal. Accounting for these nonlinear effects is more important in pulsed regime due to the high peak intensities that can be reached. Therefore, this Chapter also presented a brief review of the most relevant nonlinear effects observed in the experiments carried out in the Thesis. For example, in Chapter 4 and 6 GVD parameter β_2 and SPM play a fundamental role for picosecond pulse formation. In Chapter 7 pulse amplification of picosecond pulses in DCF amplifiers leads to pulse spectral broadening due to SPM. Controlling excessive SPM in pulse amplification is foremost to avoid pulse distortions that can lead to pulse break-up. In Chapter 8 SRS is exploited with help of a highly nonlinear fibre (HNLF) to generate a broadband source of $\sim$ 135 nm in the 1550 nm region.

Chapter 3

Mode-locked fibre lasers

Ultrafast lasers have become important tools for a variety of industrial and scientific applications [42, 43]. In particular, fibre-based ultrafast sources can benefit from the major advantages offered by fibre laser technology in terms of power scalability, large spectral bandwidth, and good spatial mode quality. Furthermore, the flexibility of fibre laser technology has generated ultrafast fibre lasers covering a broad range of pulse widths (ns to fs) and pulse repetition frequencies (kHz to GHz). In particular, for the fs to tens of ps, passive mode-locking (ML) techniques have proved useful with pulse repetition frequencies ranging from hundreds of kHz to GHz [2].

In this thesis, two different passive ML techniques are used to generate picosecond pulses with pulse repetition rates in the MHz regime. Therefore, in order to provide some background in this field, this Chapter gives a brief summary of the passive ML techniques most commonly used to generate ultrashort pulses. In addition, the second part of the chapter is focused on discussing the different pulse-shaping mechanism in the fibre cavity to obtain higher pulse energies straight from the oscillator.

3.1 Passive mode-locking techniques

The output spectrum of a fibre laser is formed of discrete components generated by constructive interference at specific wavelengths, also known as longitudinal modes. Such modes are determined by the length of the cavity and, in the case of cw lasers, are independent and random in phase among them [44]. ML ocurrs when the phases of the longitudinal modes of a laser are locked to a constant value ϕ and the laser output is formed of a pulse train spaced by the fundamental frequency retition rate. ML techniques for fibre lasers can be divided in two groups: active ML and passive ML. Regarding the former, the technique is based on active modulation of the intracavity losses or of the round-trip phase change. This is usually carried out through electro-optic devices. Pulse formation occurs whenever the modulation is synchronized with the intracavity round trip. Passive ML, on the other hand, is an all-optical technique that relies on the interaction of intensity fluctuations and fibre nonlinearities to modulate the cavity loss without an external signal or control [5]. Passive ML fibre lasers have been achieved using different methods such as: nonlinear polarization rotation [45, 46], nonlinear amplifying loop mirror [47, 48], semiconductor saturable absorbers (SESAMs) [49, 50] , carbon nanotubes [51, 52], frequency-shifted feedback lasers [8, 53], etc. The first two methods rely on artificial saturable absorbers generated by the interaction of a Kerr effect in an optical fibre and a polarizer. One of the main advantages of these techniques is that its artificial saturable absorber provides a fast recovery time allowing the formation of sub-100 femtosecond pulses [42]. Nevertheless, a constant problem shown with these techniques is that ML most of the times is not self-starting. A solution for this problem is the inclusion of “bulk” saturable absorbers into the cavity to enhance the self-starting ML operation of the laser.

3.1.1 Nonlinear amplifying loop mirror

The nonlinear amplifying-loop mirror (NALM) is a technique that consists of a fibre Sagnac interferometer with a gain medium located asymmetrically in the loop [54]. Due to the asymmetry in the position of the amplifier, the two signals propagating in opposite direction in the loop acquire different nonlinear phase shifts. With a proper phase bias the NALM can transmit higher intensities (pulse peak) and reflect lower intensities (pulse wings). The structure can be integrated into figure-8 lasers (see Fig. 3.1) where a pulse exiting the NALM section is narrower than to the same pulse before entering the NALM.

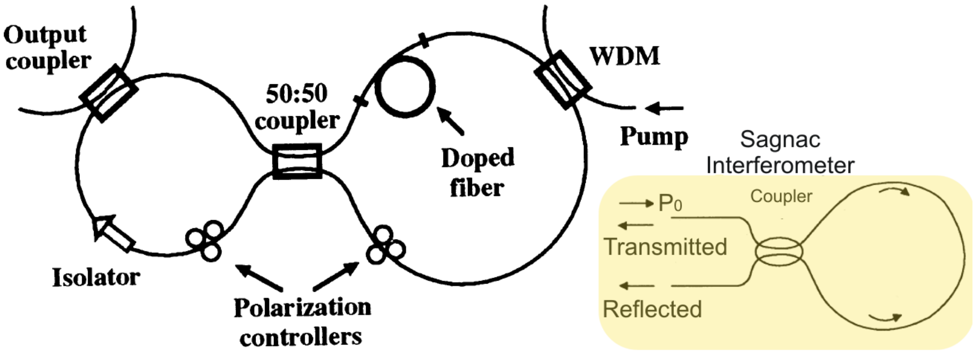

FIGURE 3.1: Schematic of a figure-8 cavity. The ring cavity on the right acts as a nonlinear amplifying-loop mirror, whose basic structure (Sagnac interferometer) is represented by the diagram on the bottom right of the figure. [5].

3.1.2 Nonlinear polarization evolution

This technique was first used in 1992 for passive ML of fibre lasers [55, 56]. Nonlinear polarization evolution is related to the intensity dependent changes of an elliptical polarized pulse propagating in an optical fibre. This phenomenon can be better understood by referring to Fig. 3.2. Here, an optical fibre is located between two polarization controllers (quarter-wave plate and half-wave plate), and two linear polarizers. Considering an initial linearly polarized pulse, its polarization changes to elliptical after leaving the quarter-wave plate. The polarization state evolves nonlinearly during propagation of the pulse in the optical fibre (represented in the figure by the Kerr medium) due to SPM- and XPM- induced phase shifts [6]. At the output of the fibre, the pulse has a non-uniform state of polarization due to the intensity dependence of the nonlinear phase shift. The half-wave plate placed at the output of the fibre orients the polarization state of the pulse peak to pass through the second polarizer, while the wings are blocked due to the different polarization state. The net result is that the pulse is shortened after one round trip through these optical devices. This is similar to the action produced by a fast saturable absorber.

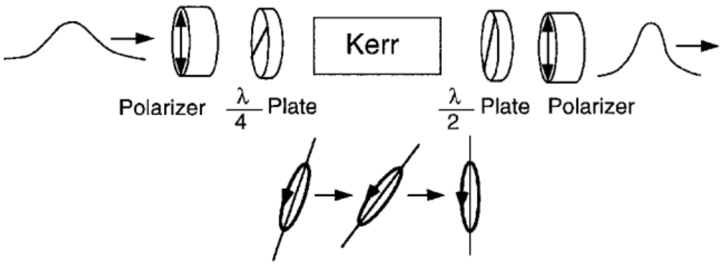

FIGURE 3.2: Representation of nonlinear polarization evolution. [6].

3.1.3 Semiconductor Saturable absorbers

SESAMs have become essential intracavity components for passively ML lasers, due to their optical properties that can be engineered over a broad range, thus allowing their use in wider cavity laser designs [57]. A SESAM is a mirror structure, typically formed of a semiconductor Bragg reflector (DBR), and additional top layers producing saturable absorption (usually a quantum well absorber) [58]. The basic mechanism of these devices can be understood as follows. When an optical pulse propagates through the SESAM, the absorption of the device will change accordingly to the pulse intensity. In this regard, the central part of the pulse, with higher intensities, will saturate the absorber and consequently the net losses of the device will be reduced. On the contrary, the wings of the pulse, with lower intensity, cannot saturate the device and will experience more losses. The net result is a shortening of the pulse during its passage through the absorber and the removal of cw radiation that could built up in the laser and make it unstable.

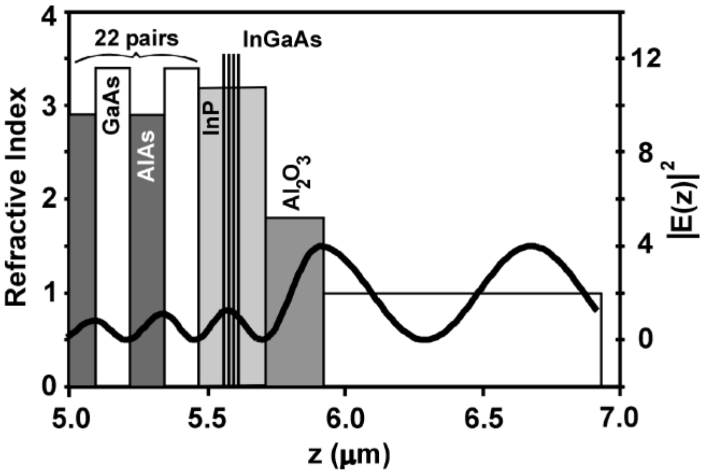

FIGURE 3.3: Schematic of an anti-reflection coated semiconductor saturable absorber mirror containing two quantum wells [7].

Figure 3.3 shows a schematic of a typical anti-reflection coated SESAM grown on a GaAs substrate containing a group of 22 pair GaAs/AlAs quarter wavelength DBR stack quantum wells as high reflectors, a half wavelength layer of InP with two InGaAs quantum wells as the saturable material, and a quarter-wavelength layer of Al_2O_3 acting as an antireflection coating [7]. In particular, for fibre lasers, SESAMs offer several advantages such as, self-starting mode locking, enhancement in the ML stability [58], and easy implementation in relatively simple and compact cavity designs [50, 59–62]. In Chapter 6 a SESAM is used in combination with nonlinear polarization evolution to ML several fibre lasers to generate picosecond pulses. Chapter 6 gives a detailed description of the SESAM used in the experiments of that chapter.

3.2 Ultrafast fibre laser oscillators

During the past decade substantial research has been done to develop fibre-based ML oscillators that can support higher pulse energies and peak powers. In this section, I give a brief overview of the recent advances in fibre based ML oscillators that have led to pulse energies up to 20 nJ with peak powers in excess of 100 kW [63].

In general, the evolution of a pulse in a ML laser depends on the interplay between the cavity GVD parameter β_2, the nonlinear phase accumulation of the pulse in one cavity roundtrip, and the amplitude modulation generated by a saturable absorber [43]. In this regard, the development of novel pulse fibre laser configurations is focused on avoiding excessive nonlinear phase shifts that can significantly distort the pulse profile evolution, and lead to its eventual break up (wave-breaking). Fig. 3.4 shows a qualitative description of the interplay between pulse duration, cavity dispersion map and pulse chirp for four stable pulse solutions in ML fibre lasers: soliton, stretched-pulse, self-similar pulse, and all-normal pulse.

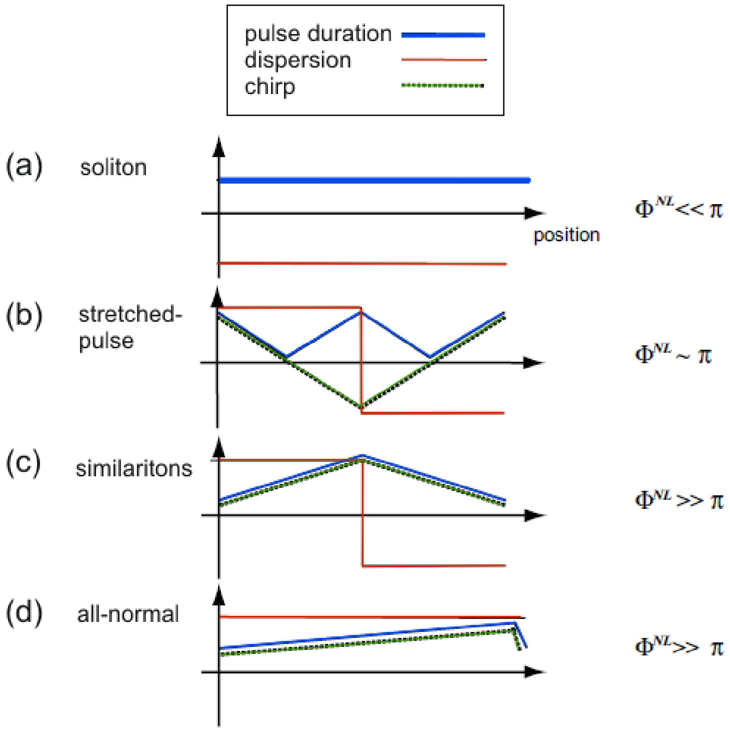

FIGURE 3.4: Description of different pulse evolutions as functions of the cavity dispersion map (solid red line) of a fibre laser: (a) soliton, (b) stretched-pulse, (c) self-similar pulse, and (d) all-normal pulse. The blue solid line represents the pulse duration, while the dotted green line represents pulse chirp. The maximum nonlinear phase shift that each pulse can tolerate before wave-breaking is indicated on the right side of each diagram.

3.2.1 Soliton fibre lasers

Soliton fibre lasers (see Fig. 3.4 (a)) are cavities formed with anomalous-dispersion that can support pulse solutions of the form:

$$A(t) = A_0 sech(t/\tau) exp(i\phi_s), \tag{3.1}$$

where $\tau^s_{FWHM} = 1.763\tau$ is the FWHM pulsewidth and $\phi_s = |\beta_2| / 2\tau^2$, is the soliton phase. Here β_2 represents the group velocity dispersion (GVD) parameter. Solitons are chirp-free solutions (bandwidth-limited) formed by the cancelation of negative dispersive and positive nonlinear phase shifts. Their $sech^2$ pulse-shape is always characterized by long extended temporal wings and spectral side bands, called Kelly bands [64]. In terms of the amount of extractable energy that one can get from these lasers, the main drawback comes from the soliton area theorem which fixes the product of the peak amplitude A_0 and pulse width τ^s_{FWHM} to the average intracavity dispersion D_2 and the nonlinearity γ of the laser cavity [65]. D_2 is defined as $D_2 = \beta_2 z$, where z is the length of the laser cavity. The pulse energy E_s and τ^s_{FWHM} in a soliton laser can be calculated by [42]:

$$E_s = \frac{3.53\sqrt{|D_2|}}{\gamma L} \tag{3.2}$$

where $\tau^s_{FWHM} = \sqrt{|D_2|}$ and γ is the nonlinear coeffiecient of the fibre L is the intracavity fibre length. As a result of the energy limitation per pulse, the total energy per pulse becomes quantized. Energies achievable in such laser systems are often between tens of picojoules and a few nanojoules [66].

3.2.2 Dispersion-managed fibre lasers

An approach to avoid soliton formation is to include in the laser cavity a section of normal-dispersion fibre to control the amount of nonlinear phase shift accumulated in the pulse (see Fig. 3.4 (b))[6]. These cavities support Gaussian-shaped pulses of the form $A(t) = A_0 \, exp\left[-(t/2\tau)^2\right]$, and are formed when self-phase modulation spectral broadening is compensated by self-phase modulation spectral compression after one round trip in the laser cavity. Fig. 3.5 shows the experimental setup carried out by Tamura et.al. [67] to generate 77 fs pulses with 90 pJ energy. The different dispersions (positive and negative) in the cavity forced the pulse to stretch and compress as it travels along the laser cavity. This pulse breathing helps to reduce the average peak power inside the laser cavity, and thus decreases the net nonlinear phase shift per round trip. Fig. 3.4 (b) depicts the pulse width and chirp evolution of a pulse along the dispersion map of a stretched-pulse laser cavity. A pulse traveling in this type of cavity generally stretches and compress twice per cavity round-trip, reaching nearly transform-limited pulses at the middle of each segment and acquire both positive and negative chirp. Stretched-pulses have a maximum nonlinear phase accumulation of $\sim \pi$.

The pulse energy generated for a specific dispersion-managed configuration is given by [42]:

$$E_g = \frac{4.47\sqrt{|D_2|}}{\gamma L}, \tag{3.3}$$

where the pulse width at FWHM is given by $\tau^g_{FWHM} = 0.66\sqrt{|D_2|}$. Pulse energy and

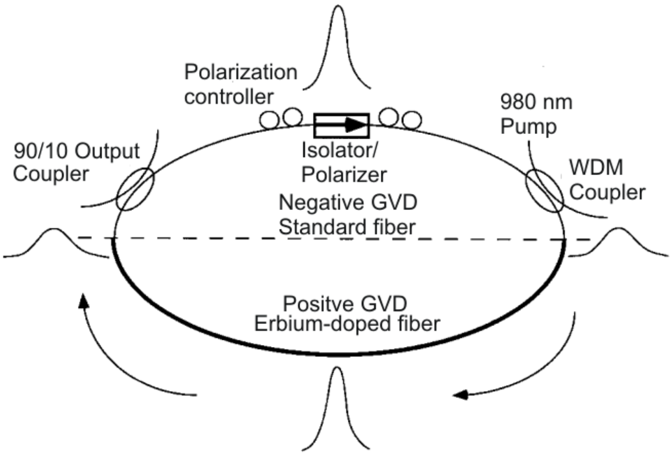

FIGURE 3.5: Schematic of an all-fibre dispersion-managed fibre laser [6].

pulsewidth of dispersive-managed cavities, contrary to soliton pulses, are governed by the total amount of positive dispersion $D_2 = \beta_2 z$ [42] and not by the net dispersion in the cavity.

3.2.3 Similariton fibre lasers

Efforts to increase the pulse energy from fibre oscillators also led to the development of similariton fibre lasers. Similaritons are highly-chirped parabolic-shaped pulses of the form $A(t) = A_0\left[1-(t/\tau)^2\right]^{1/2} exp\left(-iC(t^2/2\tau^2)\right)$ that operate in fibre laser cavities with slight positive dispersion. Such pulses evolve self-similarly, which means that pulses are always a scaled version of themselves. Fig. 3.4 (c) shows a conceptual model of the pulse width evolution of a similariton along the dispersion map of a cavity laser. Generally, in these cavities similariton pulses stretch and compress once per cavity round trip, have positive chirp all over the cavity, and have minimum pulse width at the beginning of the normal-dispersion segment. This segment is usually formed by the gain fibre where the input pulse is amplified self-similarly. Parabolic-shaped pulses makes similaritons resistant to wave breaking and can support larger levels of nonlinear phase shifts ($> \pi$) in comparison with soliton and dispersion-managed pulses [68, 69].

Outstanding pulse energies have been achieved with similariton fibre lasers, either for Yb^{3+}-based or Er^{3+}-based fibre lasers. For the former, works have demonstrated 100-fs pulses with pulse energy of 14 nJ and average output power of 300 mW [70], while for the latter, 64-fs pulsewidths with pule energy of 6.2 nJ and average powers of 675 mW have been demonstrated [71]. Such pulse energies are approximately five times higher than those obtained for dispersion-managed lasers.

3.2.4 All-normal fibre lasers

Recent works have shown that laser cavities with large normal dispersion support highly-chirped pulses (see Fig. 3.4 (d))with high energies and peak powers without pulse-breaking. The pulses in these cavities are formed by the interaction of nonlinear chirping and filtering which eventually produces strong self-amplitude modulation that can dominate the pulse-shaping. Pulses obtained with these configurations can also have pulse energies of $\sim$ 10 nJ.

3.3 Conclusions

In this Chapter, I presented a summary of the mechanism to generate passive ML lasers. In particular, the nonlinear polarization evolution technique and the semiconductor saturable absorber, are the techniques used for the development of the pulsed lasers described in Chapter 4 and 5. In this chapter I also discussed the different pulse-shaping mechanism in fibre cavities to obtain higher pulse energies straight from the oscillator. Two configurations are developed for this thesis: a soliton source, and a dispersion-managed source. Both configurations will be described in detail in the next Chapters.

Chapter 4

Mode-locked laser based on frequency-shifted feedback technique

In this Chapter I give an introduction to the operating principles of frequency-shifted feedback (FSF) lasers in the mode-locking (ML) regime. In addition, I give a brief summary of former theoretical and experimental work carried out with FSF lasers. I present the experimental results of two all-fibre Er^{3+}-doped laser configurations using an acousto-optic modulator (AOM) as a frequency shifter inside the cavity. The first configuration presents a simple ring cavity (gain medium, polarization controller, optical filter, output coupler, and frequency shifter) which facilitates the study of different operating regimes of the laser for different pump powers. The second configuration includes a fiberized polarizer which stimulates the nonlinear polarization evolution in the cavity. This hybrid FSF laser configuration enhances the stability in the ML regime allowing pulse analysis as function of different parameters of the laser cavity (frequency shift, coupling ratio, filter bandwidth). Experimental results obtained in this chapter, in addition to the numerical simulations of Chapter 5, provide a better understanding of the dynamics of FSF lasers in the ML regime, which have not been addressed in previous work. The study of the characteristics of the signal allows enumerating the advantages and disadvantages of this technique for ML pulses and its possible application for dynamic pulse sources.

4.1 Operating principles of frequency-shifted feedback lasers

The signal of a conventional laser is determined by four main elements: gain medium, feedback system, frequency-selection mechanism, and output coupling. The interaction of these elements generate a well-defined signal formed by the constructive interference and constant amplification of specific frequencies which match a resonant condition in the laser cavity (resonant frequencies). Over many round-trips, the signal reaches a steady-state regime and the gain of the amplifier equals the losses in the cavity leading to a round-trip gain close to unity. For a laser cavity comprising a frequency filter, this unity gain region is localized near the filter central frequency ν_c. See for example, Fig. 4.1 (a). However, in a laser with a frequency-shifted feedback (FSF) mechanism, the spectral components of the electric field travelling inside the cavity are shifted by "f_{AOM}" each time they pass through an intracavity frequency shifter. In this way, the energy localized close to ν_c is displaced to the higher-loss regions of the filter, generating an excess loss at ν_c. In order to overcome this excess loss, the net round-trip gain will acquire a value larger than unity around ν_c. Moreover, if the spectral components that are constantly shifted in the cavity are not somehow replaced as they leave the filter bandwidth, they will die out. In this sense, the laser acts as a broadband optical amplifier rather than a laser because the frequency-shifting effect does not allow the laser modes to be fixed at one specific wavelength. Therefore, at low pump powers, the spectral shape of the FSF laser shows a broader bandwidth and an asymmetry in comparison to the spectral shape of a conventional laser (see Fig.4.1(b)).

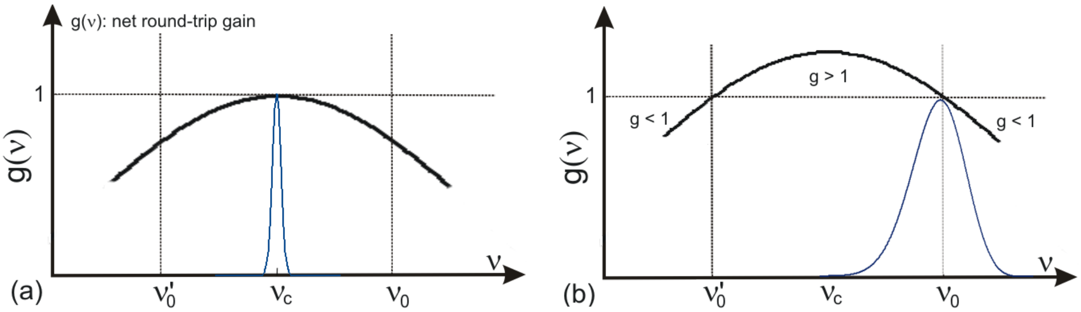

FIGURE 4.1: Schematic of the steady-state spectrum (blue solid line) of a laser (a) without and (b) with a frequency shifter inside the laser cavity. The black solid line represents the net round-trip gain $g(\nu_c)$ of the laser cavity.

Further studies in FSF lasers showed that under certain parameter conditions, these lasers could operate in different regimes such as broadband cw [72, 73] or pulsed mode [8, 53, 74, 75]. Regarding the latter, this regime appears with the introduction of a Kerr nonlinearity (e.g., SPM) in the resonator [8]. SPM acts as a phase seed mechanism that can establish a phase distribution along the spectrum of the bandpass filter, enhancing pulse formation. Once a pulse is formed, it can remain trapped in the cavity by the interaction of the continuous frequency shifting mechanism and the frequency dependent gain/loss properties of the cavity (optical filter). The explanation given beforehand is summarized in Fig.4.2. In this schematic, it is assumed that a feedback loop is stablished in the cavity and a pulse has been formed from stochastic noise (see Fig.4.2(1)). In this case, the continuos shift of the spectral components carried out by the frequency shifter pushes the pulse spectrum to the higher loss wings of the filter 4.2(2). However, the spectral components are then reshaped to its original state by the frequency dependent gain and loss of the laser cavity Fig.4.2(3). The new spectral components that will act as a phase seed mechanism are generated by means of SPM when the pulse travels through the nonlinear medium. These new spectral components are uniquely related to the phase spectrum of the generated pulse and feedback energy from the center of the pulse spectrum into its wings Fig.4.2(4). This process of spectral broadening of the generated pulse continues until a steady-state is reached.

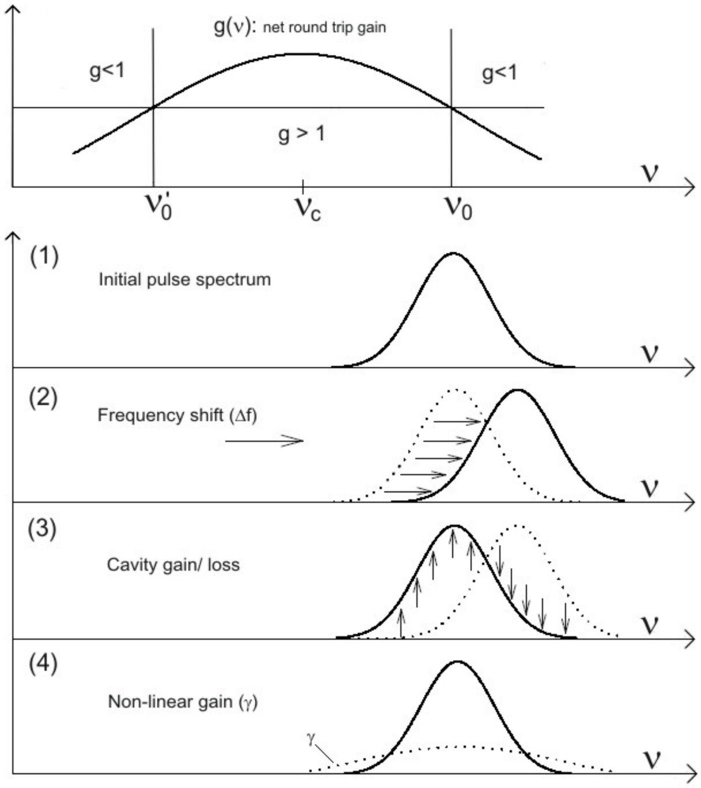

Figure 4.2: Evolution of the optical spectrum of a pulse in a FSF laser cavity with a net roundtrip gain $g(\nu)$: (1) Initial spectrum of the seeded pulse, (2) spectrum after the frequency shifting process, (3), reshaped spectrum by frequency dependent gain or loss process, and (4) generation of new spectral components by the cavity nonlinear gain. Processes (1) to (4) are iterated until a steady state is reached when the pulse spectral width becomes comparable to the filter bandwidth [8].

FSF lasers have been widely studied since their first mention in the literature, by Streifer et al. [76]. Their distinctive performance which allow them to operate in either broadband cw or pulsed regimes has made them attractive as light sources for applications such as broadband cw lasers [72, 73] to laser cooling [77], distance metrology [78, 79], multi-wavelength lasers [80–84], and pulse sources [8, 53, 75, 85–93]. Regarding the generation of ultrashort pulses with FSF lasers, the first report published dates from 1988 [73]. Since then, different work has been carried out in order to achieve shorter and higher-energy pulses from this type of lasers. The next section provides a brief review of the experimental work carried out up to date to generate ultrashort pulses with the FSF techniques. Theoretical investigations of FSF lasers will be further discussed in Chapter 5 where analytical and numerical simulation results are presented and compared with previous work.

4.2 Literature review of frequency-shifted feedback lasers

Pulse formation in FSF lasers was first reported by Kowalski et al. in 1988 [73]. In this work pulse widths between 29 ps and 9.6 ps with random pulse repetition rates were generated in a ring dye laser. Years later, Hale et.al [94] and Cutler [95] published theoretical models to calculate the shape of the output laser intensity in time and frequency domains. Both models showed that a FSF cavity could generate periodic pulses with a repetition rate equal to the inverse cavity round-trip time. Yet, these models did not consider noise or nonlinear effects. The role of nonlinear effects in pulse formation was studied by Sabert et. al [8]. The work suggested that Kerr-type nonlinearity of the optical fibre was responsible for pulse formation in the laser cavity. In this work the authors also demonstrated numerically and experimentally that shorter pulses and broader linewidths could be achieved by increasing the frequency shift in the cavity. These experiments were carried out in Er^{3+} and Nd^{3+} fibre lasers. A different analysis of pulse formation in FSF lasers was given by Fontana et al. [53]. In this work the authors presented an analogy of the sliding filter technique, used in long distance transmission systems, with the performance of a FSF fibre ring laser [96]. The authors demonstrated self-starting soliton generation with pulse widths between 20 and 16 ps with an Er^{3+} doped fibre FSF ring laser. The role of group velocity dispersion GVD in FSF laser was studied by Romagnoli et al. [86]. The authors concluded that pulse formation was possible in either anomalous or normal dispersion regimes. Therefore, FSF laser have also been demonstrated with Yb^{3+} fibres. For instance, Porta et al. demonstrated a tunable ML FSF laser operating in the region between 1010 nm and 1064 nm [89]. The laser generated 5 ps pulses and it operated in simultaneous Q-switched and ML regimes enabling the generation of 1.2 kW peak powers.

The first all-fibre FSF laser was published in [75]. This novel design was based on a fiberized acousto-optic frequency shifter which also worked as a band-pass filter. Okhotnikov et al. demonstrated in [80] that pulse formation in FSF lasers was also possible without using a tight spectral filtering mechanism (band-pass filter), which could eventually limit pulse shortening. Subpicosecond pulses in FSF laser have been achieved by inserting polarizing elements, i.e. a polarization beam splitter, inside the cavity [90, 91]. Ultrashort pulses were generated in this way by exploiting the nonlinear polarization evolution inside the ring cavity. For instance, in [91], an Yb^{3+}-doped FSF fibre laser generated stable 4-ps chirped pulses that were compressed outside the cavity to 68 fs pulses with energies of $\sim$ 100 pJ. Subpicosecond pulses were also achieved with hybrid cavity configurations like the one presented in [87]. In this work, slightly chirped $<$ 2-ps pulses were obtained with a laser cavity that included a nonlinear amplifying loop mirror (NALM). Pulses were compressed to the subpicosecond regime by compensating the linear chirp on the pulses by means of a piece of SMF-28 fiber.

Tunable FSF lasers have also been realised through different means [75, 85, 93]. For instance, in [75] wavelength tuning was achieved by controlling the acoustic driving frequency of a home made acousto-optic fiber frequency shifter. In more recent work, Nikodem et al. showed that adjustments of the AOM RF power could also lead to wavelength tuning [93].

Work has also been carried out to increase the peak power of the pulses in FSF fibre lasers. For instance, Broderick et al. increased the output energy of an Er^{3+}-doped FSF fibre laser by using a large mode area (LMA) fibre [88]. Pulse energies of $\sim$ 1.6 nJ and peak powers of 1.7 kW were demonstrated with this design. Heidt et al. demonstrated pulse energies up to 120 nJ and peak powers exceeding 40 kW with a Yb^{3+}-doped fiber laser with a linear cavity design [92]. Furthermore, the energies of the pulses were significantly increased by inducing a Q-switched ML. The energies achieved with this technique reached 1 μJ with average output powers as high as 870 mW.

Pulses generated with FSF lasers present an asymmetry in the optical spectrum, which is a consequence of the quadratic frequency chirp imposed by the frequency shifter [97] and the filter dispersion [96] in the cavity. Although this is a well-known characteristic of FSF lasers, there is little work that has linked experimental results [8, 86, 98] with analytical models describing the ML regime in FSF lasers [96, 97]. Furthermore, most of the experimental work carried out with ML Er^{3+}-doped FSF lasers have been focused on achieving shorter pulses through different cavity configurations without paying much attention to the pulse spectral shape and its relation with the pulse behavior in the time domain. For example, in work like [86, 90, 93] the experimental results show a strong asymmetry in the pulse spectrum; however, it is not clear how the different parameters in the laser cavity (filter bandwidth, frequency shift, gain)determine or modify the shape of the pulse in the frequency and time domains.

In the next section, I present experimental studies analysing the behaviour of the pulse shape and pulse spectra for different parameters of a ML Er^{3+}-doped FSF fiber laser in a ring cavity configuration. The experimental results are compared with the numerical simulations presented in Chapter 5. These novel experimental results allow a better understanding of the dynamics of FSF lasers and its advantages and limitations as a technique to generate ML sources.

4.3 Experimental Results

This section presents experimental results obtained from a tunable all-fibre ring cavity FSF laser. Modifications to the main cavity were carried out in order to increase the stability of the ML pulses. Self-starting ML and stable pulses were achieved by including a polarization beam splitter (PBS) to enhance non-linear polarization evolution (NLPE) inside the cavity. The stability achieved in this configuration allowed me to study the behavior of the ML signal as a function of different parameters of the laser cavity.

4.3.1 All-fibre ring cavity frequency-shifted feedback laser

Figure 4.3 shows the first scheme built to generate a tunable pico-second source based on FSF. The laser was formed of a 2.5 m long polarization maintaining Er^{3+}-doped fibre (IX-FIBRE, peak absorption @ 1530 nm 18 dB/m, core diameter 3 μm, and cut-off wavelength λ_{cf} = 980 nm) pumped by two pig-tailed laser diodes through a WDM coupler (1480/1550 nm). The laser diodes provided a maximum of 270 mW of pump power at 1480 nm (Fitel FOL 1402P). A second WDM coupler (1480 nm/1550 nm) was spliced after the gain fiber to eliminate the unabsorbed power inside the cavity. Unidirectional operation in the cavity was achieved by splicing an optical isolator after the second WDM. A polarization controller (PC: 1) formed of a quarter-waveplate $\lambda/4$, half-waveplate $\lambda/2$, and quarter-waveplate $\lambda/4$, helped to stabilize the ML operation of the laser. The tunability of the laser was achieved with a 30 nm tunable filter (SANTEC OTF-30M) with an optical bandwidth of $\Delta\lambda_{BPF}$ = 1.3 nm. The frequency shifting mechanism was generated with two fiberized AOMs (NEOS 26035-2-1.55-LTD) with a frequency shift of f_{AOM} = 35 MHz each. Therefore, the total frequency shift in the cavity was f_{AOM} = 70 MHz [1]. The output of the laser cavity consisted of a 50:50 output coupler spliced before the AOM. The laser output power was detected with a power meter (HP 81531B), while pulse measurements in the time domain were carried out with a 20 GHz fast photodetector (HP-83440C) and a digital communication analyser (DCA) (HP 83480A) with a 20 GHz electrical bandwidth. The DCA bandwidth gave the possibility to measure pulses as short as 22 ps. Finally, the signal spectrum was recorded with an optical spectrum analyser (OSA) (Ando AQ6315).

---

[1] First experiments were carried out with only one AOM. The additional AOM was proposed in order to reduce the pulse width (See Chapter 5). However, the pulse width measurements carried out after the implementation of the second AOM, did not show any clear reduction in the pulse width. Yet, the second AOM helped to mode-lock the laser more easily.

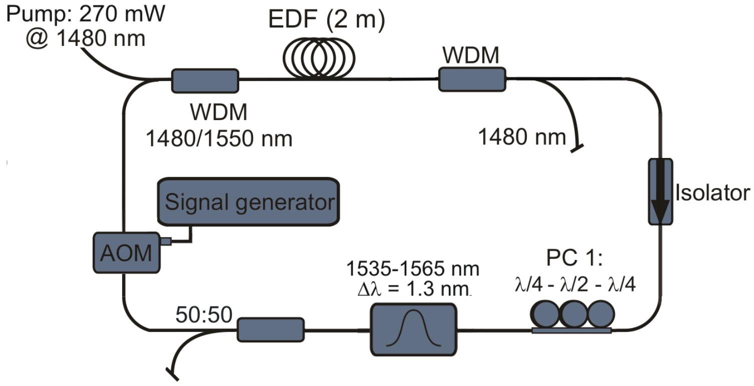

FIGURE 4.3: Experimental setup of the all-fibre FSF, Er^{3+}-doped fibre laser.

The cavity length was $\sim$ 20.8 m which corresponds to a cavity round trip time τ_{rt} = 100.5 ns. The average group velocity dispersion parameter of the cavity at 1550 nm was calculated as $\beta_2 = -16\ ps^2/\text{km}$ (anomalous dispersion). The GVD parameter β_2 of the PM-Er^{+3} doped fibre was calculated from its refractive index profile (FRIP) with the help of commercial software (FiberCad). The value calculated was $\beta_2 = 17.8\ ps^2/\text{km}$ at 1550 nm, for the fast axis. The rest of the cavity was formed of SMF-28 with a dispersion value of $\beta_2 = -20\ ps^2/\text{km}$ at 1550 nm.

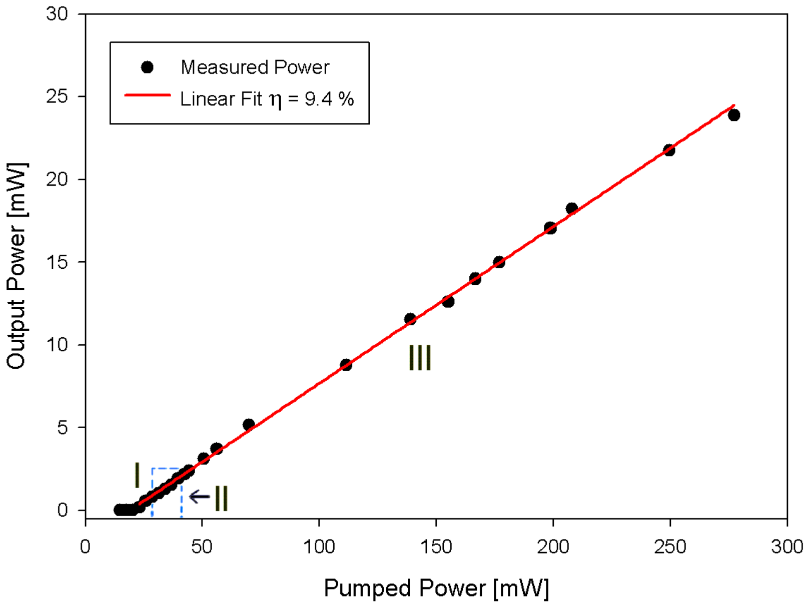

FIGURE 4.4: Output power versus pumped power of an all-fiber, ring cavity, FSF laser with a 1.3 nm optical bandwidth filter.

The output power performance of the laser operating at λ_0= 1555 nm is shown in Fig. 4.4. The laser threshold was measured at 20 mW of pump power. Different operating regimes were found as a function of pump power. Fig. 4.4 shows three different operating regimes, identified by significant changes in the output signal. Region I, is delimited from the laser threshold (20 mW) up to a pump power of $\sim$ 27 mW. In this region, the laser presented a cw operation with a maximum output power of 0.2 mW. For pump powers $\geq$ 27 mW, the laser stopped operating in cw mode and showed pulsation. Noisy pulses were generated in this regime, and its repetition rate increased linearly ($\sim$ 12.74 kHz to 18.02 kHz) with pump power. Fig. 4.5 shows the pulses generated in this regime. The pulse traces were taken with a fast photo-detector, and a digital oscilloscope with 2 GHz bandwidth (Tektronix DPO7254). In this regime, pulse formation was polarization insensitive.

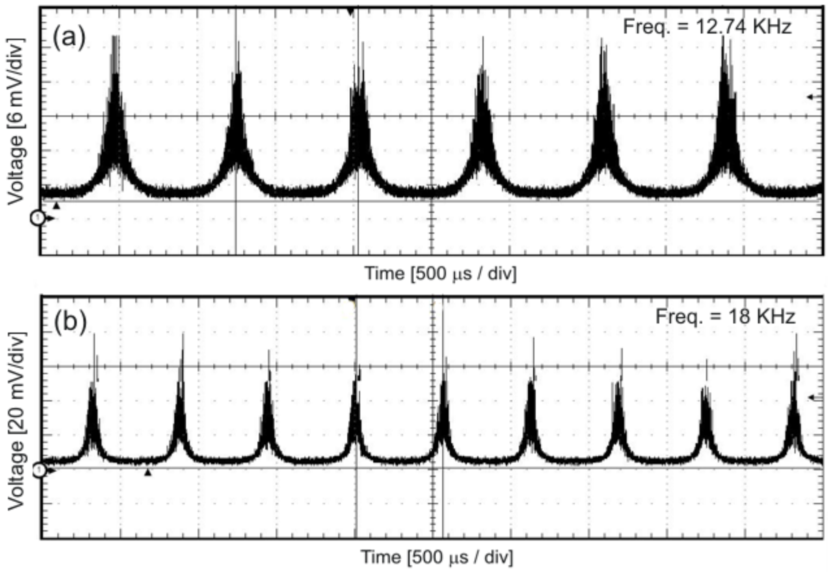

Figure 4.5: Train of pulses obtained at the output of the FSF laser for a pump power (a) $P_p = 28$ mW and (b) $P_p = 39$ mW.

The signal behaviour in the frequency domain was monitored with an RF spectrum analyser (Model HP 8562A). In addition to the signal peaks observed in the kHz region, a low-intensity beating was found at the cavity round-trip frequency $f_{rt} = 9.95$ MHz. The kHz pulsation can be explained in terms of the relaxation oscillation response of a laser to a sudden change of its operation conditions [98]. However, contrary to what happens in conventional lasers where relaxation oscillations eventually damp down to a steady state (cw emission), in FSF lasers the continuous shifting of spectral components leads to the emission of a train of independent pulses whose repetition rate depends on the pump power P_p.

For $P_p \sim 40$ mW, the system showed self-starting pulsing behaviour. The laser output emitted random sharp < 60-ps pulses with random amplitudes (see Fig. 4.6 (a)), and the quasi-symmetry of the optical spectrum observed in Regime II breaks (see the dashed blue trace in Fig. 4.6(c)). In this operating regime, the spectral maximum is shifted to longer wavelengths and the shorter wavelength side shows a *hump*. By adjusting the PCs in the cavity, it was possible to stabilize the train of pulses to either the cavity fundamental frequency f_{rt}= 9.95 MHz or to higher harmonics of f_{rt}. In both cases, the optical spectrum of the laser presented specific characteristics. For ML at f_{rt}, the optical spectrum presented a noisy quasi-symmetric shape; see for example the black solid trace in Fig. 4.6 (c). However, for higher repetition rates the spectrum presented a small *hump* on the shorter wavelength side similar to the dashed blue trace shown in Fig. 4.6(c).

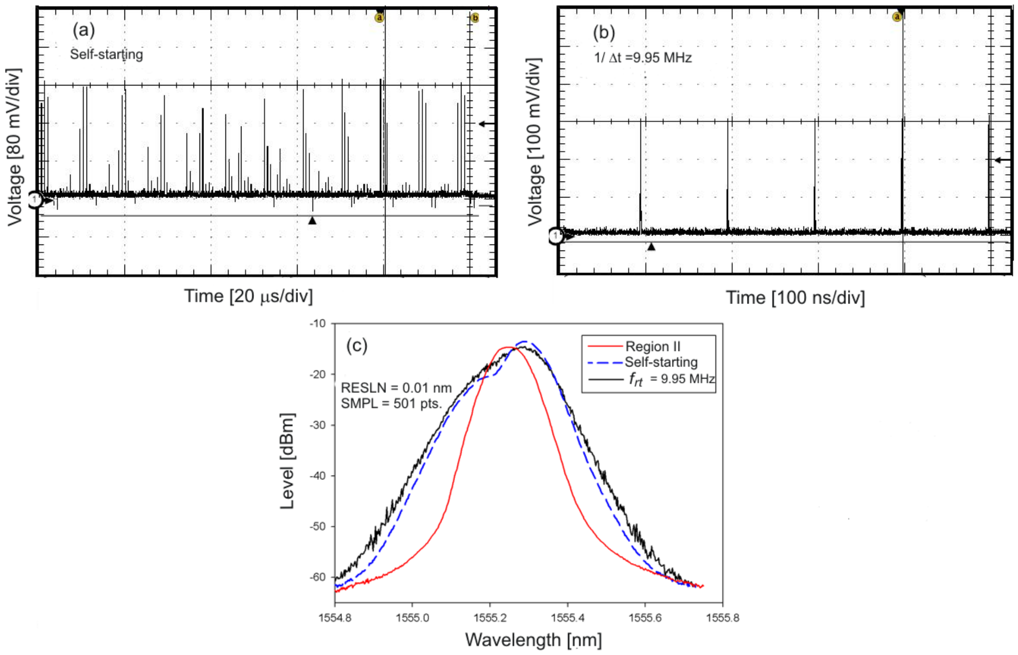

FIGURE 4.6: Laser intensity and optical spectrum of a FSF laser operating in the ML regime (Region III). (a) depicts the laser intensity just after the laser shifts into ML regime, while (b) shows the laser intensity after adjusting the PCs to mode-lock the signal to f_{rt}. (c) shows the spectrum of the optical field for three different modes of operation. Before ML regime (red solid line), ML regime (blue dashed line), ML fixed to f_{rt} (black solid line).

This particular configuration had a stronger tendency to operate in harmonic ML rather than fundamental ML. In addition, the laser operating in fundamental ML showed clustering of pulses with tens-of-ps separation between them; no single pulse could be made to circulate in the cavity. Therefore, pulse width measurements were carried out only for harmonic ML. Measurements yielded values between 57 ps and 53 ps for different repetition rates and pump powers Pp (see table 4.1). A main issue encountered in this configuration was the pulse repetition rate dependence on polarization and pump power Pp. Furthermore, the RF spectrum of the signal showed strong longitudinal mode competition for pulses at fundamental and harmonic ML. Therefore, it was proposed to include in the cavity a stronger saturable absorber mechanism in order to give more stability to the ML signal. A second configuration was built which included a fiberized polarizer to enhance a saturable absorption mechanism through non-linear polarization evolution.

TABLE 4.1: Pulsewidth measurements for different output powers. P_p: pump power, P_{out}: output power, f_{ML}: ML frequency, $\Delta\lambda$: laser bandwidth @ 3 dB, τ_{FWHM}: pulse width, TBP: time-bandwidth product, P_0: peak power.

P_p **[mW]**	P_{out} **[mW]**	f_{ML} **[MHz]**	$\Delta\lambda$ **[nm]**	τ_{FWHM} **[ps]**	**TBP**	$\mathbf{P_0}$ **[mW]**
70	2.16	59.7	0.094	53	0.62	680
100	7.76	249	0.098	56	0.68	550
200	15.14	497	0.096	57	0.67	530

4.3.2 Hybrid all-fibre ring cavity frequency-shifted feedback laser

The setup of the FSF laser is shown in Fig. 4.7. The laser consists of 2-m of a commercial FiberCore Er^{3+}-doped fiber (peak absorption @ 1530 nm $\sim$ 37 dB/m) pumped by two laser diodes delivering a total power of $\sim$ 270 mW @ 1480 nm through a WDM coupler (1480/1550 nm). A second WDM coupler was spliced to the other end of the active fiber in order to remove the unabsorbed pump power from the cavity. Two sets of polarization controllers - PC 1, and PC 2-, were spliced between a fiberized polarization beam splitter PBS to introduce the necessary phase bias to lock the longitudinal modes of the ring cavity and to adjust the output coupling in the cavity. PC 1 was formed of three wave plates (a quarter-wave plate, a half-wave plate, and a quarter-wave plate), while PC 2 was formed of only two wave plates (a quarter-wave plate, and a half-wave plate). A 95:5 % coupler was spliced after PC 2 to monitor the intracavity signal. For this configuration, the frequency-shifting mechanism inside the cavity was carried out through four different fibre-coupled AOMs from Gooch & Housego, driven by an RF signal generator. The downshift frequencies of three of the AOMs were f_{AOM} = -80 MHz, -110 MHz, and -200 MHz. The fourth AOM had an upshift frequency of f_{AOM} = +110 MHz. All AOMs showed similar characteristics except for the -200 MHz AOM, which had higher insertion loss compared to the rest of the AOMs [2]. Two types of band-pass filter (BPF) were used in the cavity. The first one was the same fiberized optical tunable filter described in Section 4.3.1, while the second one was a fiber Bragg grating (FBG) with 0.45 nm bandwidth. Finally, the unidirectionality of the ring cavity was ensured by splicing a fiberized isolator. The cavity configuration shown in 4.7 (a), had a total length of $\sim$ 14.5 m with an average GVD parameter of β_2 = -15 ps^2/km.

---

[2] The advantage of using the Gooch & Housego AOMs rather than the NEOS AOMs was the possibility to tune the frequency driving signal of the former ones. Therefore, it allowed to study the behaviour of the laser in resonant ($f_{AOM} = 1/\tau_{rt}$) and non-resonant regimes ($f_{AOM} \neq 1/\tau_{rt}$)

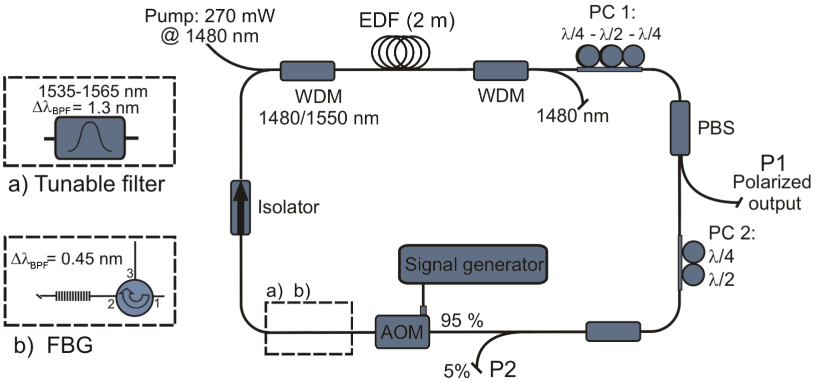

FIGURE 4.7: Schematic of the Er^{3+}-doped fiber ring laser with a frequency shifter spliced to the cavity for (a) a tunable filter with an optical bandwidth of $\Delta\lambda_{BPF} = 1.3$ nm, and (b) a FBG with an optical bandwidth of $\Delta\lambda_{BPF} = 0.45$ nm. EDF: Er^{3+}-doped fiber, PC: polarization controller, PBS: polarization beam splitter, AOM: acousto-optic modulator.

4.3.2.1 Characterization of the laser cavity

The cavity in Fig. 4.7 was first tested without an AOM. In this configuration, it was not possible to mode-lock the laser at any pump power level. Therefore, the saturable absorption effect generated by the nonlinear polarization evolution, and the PBS in the cavity was not strong enough to generate ML behavior. The output signal for this configuration was formed of noisy random pulses in time and amplitude. ML of the cavity was only achieved by adding any of the AOMs described in Section 4.3.2. Self-starting fundamental ML behaviour was generated easier when the laser operated in a non-resonant regime rather than in the resonant regime. In addition, the former regime provided longer stability to the ML signal. Therefore, in all the experiments carried out, the laser operated in a non-resonant regime. Self-starting ML behavior was always achieved for high pump power levels $P_p \geq 150$ mW. However, at these pump power levels, the laser output presented clustering of pulses with, tens of ps separation between them, circulating at the fundamental repetition rate $f_{rt} = 13.7$ MHz of the cavity. See for example the inset of Fig. 4.9 (a). By decreasing the amount of pump power in the cavity, the group of pulses was reduced to a single pulse circulating in the cavity (see Fig. 4.9 (a)). Pulses formed in the cavity keep its shape and width while reducing the pump power. It is only by adjusting the polarization controllers in the cavity that the shape and width of the pulses are modified. Furthermore, once the ML regime stops for $P_p \leq 30$ mW, the laser cannot be ML again until the pump power increases above $P_p \geq 150$ mW. This behavior is a common feature observed in soliton ML lasers [85, 99], and it is related to the pump power hysteresis presented in these systems [100].

The optical spectrum shape shown in Fig. 4.8 (a) and (b) was characteristic of the ML regime of the laser cavity. The spectra shown in these figures were obtained for a 110 MHz downshifted and upshifted AOM, respectively. The *hump* observed on either the longer (downshifted frequencies) or shorter (upshifted frequencies) wavelength side of the

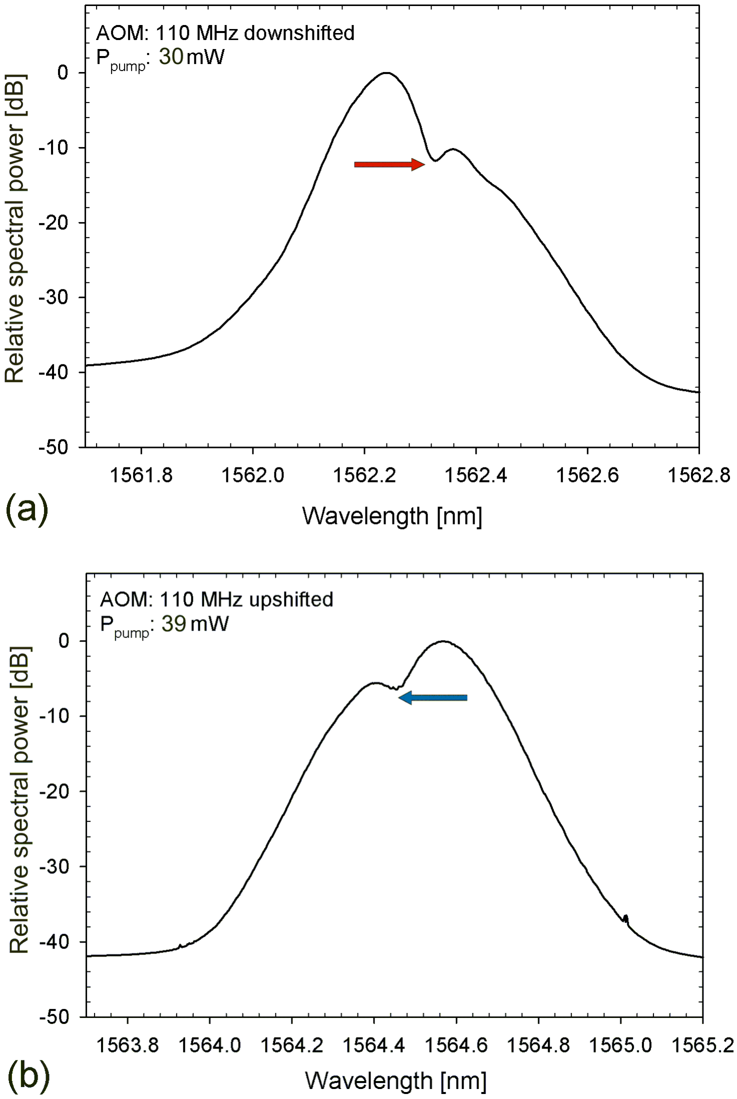

FIGURE 4.8: (a) Optical spectrum of a FSF laser in ML regime with a 110 MHz downshifted AOM, and (b) a 100 MHz upshifted AOM. The arrows in the plots represent the direction where the spectral frequencies of the laser are being shifted at every cavity round-trip.

spectrum is related to the transfer of the spectral energy carried out by the frequency shifting process of the AOM, to the higher loss region of the spectrum. A more detailed explanation of the formation of the *hump* in the spectrum will be described with the numerical simulations in Chapter 5.

Figure 4.9 (a) and (b) show the time trace and RF spectrum of the output signal for the cavity configuration shown in Fig. 4.7 (a), respectively. The laser, in this case, operated with a 110 MHz downshift frequency AOM (f_{AOM} = -100 MHz). The time trace of the output pulses was measured with the optical channel of a digital communication analyzer DCA (20 GHz bandwidth), the RF spectrum with a 5 GHz photodetector, and a RF spectrum analyzer (22 GHz bandwidth). The pulse trace, for this configuration, showed a longer trailing edge compared to the leading edge of the pulses. The inset of Fig. 4.9 (a) shows the compact group of pulses (traveling at the round-trip frequency), that are formed in the cavity for pump powers $P_p \geq 30$ mW. The inset correspond to a pump power of $P_p \sim 150$ mW, while the single pulse per round-trip is obtained at $P_p \sim 30$ mW. The pulse width measured at FWHM was $\tau_{FWHM} = 37$ ps. It is worth mentioning that the autocorrelation measurement of the signal did not show any sub-pulse structure and matched the pulse width measurement of the DCA. The optical spectrum of the ML signal is shown in Fig.4.8 (a). The pulse spectral bandwidth measured at FWHM was $\Delta\lambda = 0.12$ nm, and yields a time-bandwidth product (TBP) of 0.57. Fig.4.9 (b) shows the RF spectrum at the cavity's fundamental frequency with a resolution bandwidth of 1 kHz.

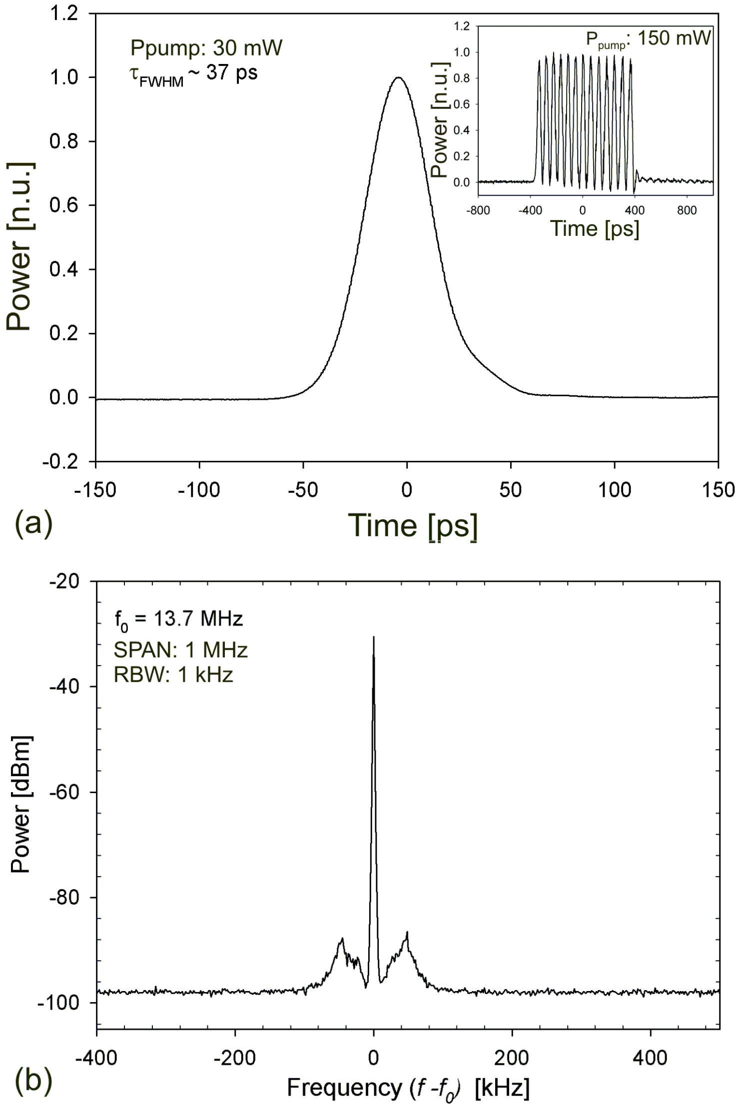

FIGURE 4.9: (a) Time trace, and (b) rf spectrum of the output signal of an all-fiberized FSF laser using an AOM with 110 MHz downshift frequency. The inset in (a) shows the stable train of pulses gathered in the form of square-shape pulses circulating in the cavity at the fundamental repetition rate for Ppump $\geq$ 33 mW.

4.3.2.2 Pulse and spectral shape as a function of the output power coupling ratio

The stability of the laser, in the ML regime, allowed me to study in more detail the dependence of the pulse shape and its optical spectrum for different parameters of the laser cavity. At this point, it is worth mentioning that all measurements shown in this section and onwards were carried out with a single pulse circulating in the cavity ($P_p \sim 30$ mW).

The pulse shape behavior as a function of the output coupling ratio in the cavity was first monitored. The coupling ratio was adjusted by finely tuning the quarter-waveplate of PC 1 located before the fiberized polarization beam splitter (see Fig. 4.7). In addition to the monitoring of the pulse shapes, the spectral maximum of the pulses and the ratio between the intracavity and output power of the system were also traced. Fig. 4.10 (a) and (b), show the shape of three optical spectra and their corresponding time traces. The optical spectrum was measured with an optical spectrum analyzer OSA with a resolution of 0.01 nm, while the time trace signal was measured with the optical channel of the DCA described in the former section. The experimental results showed that pulse shapes become more asymmetric as the split between the spectral maximum and the *hump* of the spectrum is more prominent. See for example, the differences between the red and the blue solid traces in Fig. 4.10 (a), and (b). Yet, if we plot the pulse intensity in logarithmic scale (see inset of Fig. 4.10 (b)), we can see the presence of a long tail on the trailing edge of every pulse. The difference between the shapes of the optical spectra shown in Fig. 4.10 (a) is attributed to the polarization dependent losses in the cavity which change as the coupling ratio is adjusted. Although the pulse asymmetry seen in the experimental results agrees with previous analytical models [86, 97], I consider that in our specific case, the pulse asymmetry is not necessarily related with the stronger filtering condition that the longer wavelength side of the spectrum suffers due to the frequency shifting mechanism [97], but to the hump formation on the pulse spectra. The latter does not mean that these results disagree with previous models, but as it will be explained in Chapter 5, the spectral asymmetry observed in these figures is a consequence of the broad bandwidth of the intracavity filter and the SPM generated inside the cavity.

Figure 4.11 (a) and (b) show the dependence of the pulse width and spectral maximum as a function of the output power for two different polarization states of the laser cavity. It was observed that for specific positions of the PC spools, the laser showed better ML stability. Therefore, the selection of the two polarization states was determined by the ML stability of the laser as the output power coupling ratio of the laser cavity was adjusted. Adjustment of the output power coupling ratio was carried out in the same way as in the previous experiment (slight tuning of PC 1). Results showed that for both polarization states, minimum pulse widths were achieved for coupling ratios close to

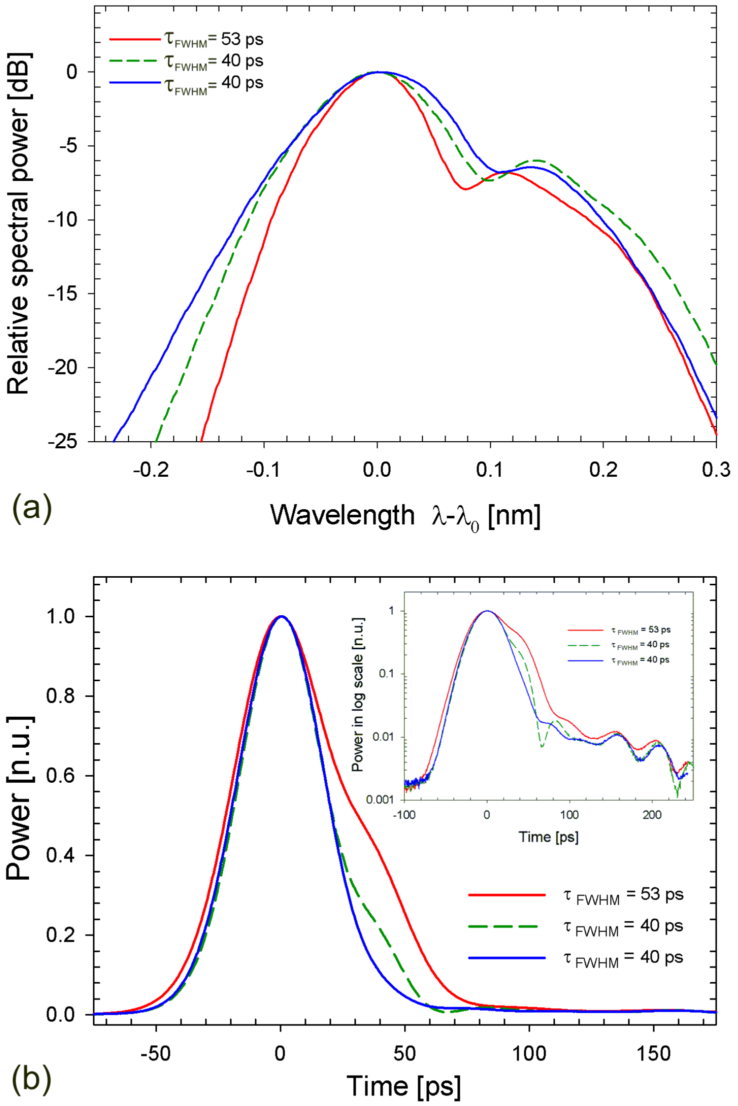

FIGURE 4.10: (a) Optical spectrum and (b) pulse intensity for different polarization states in the cavity. The spectra shown in (a) are plotted relative to the spectral maximum λ_0 of the pulse in order to compare the spectral shape. The inset in (b) shows the pulse intensity of the same pulses on logarithmic scale.

1. In addition, for both polarization states the pulse width τ_{FWHM} and ratio between the intracavity and output power P_{in}/P_{out}, were inversely proportional to the output power. However, the pulling direction of the spectral maximum was different in each polarization state. For Fig. 4.11 (a), a shift towards longer wavelength was observed at higher output powers, while in Fig. 4.11 (b) the spectral shift was in the opposite direction. This behaviour, I believe, is due to the relative position of the lasing signal inside the filter bandwidth $\Delta\lambda_{BPF}$. The reader has to bear in mind that the bandwidth of the laser signal (≤ 0.15 nm) is much narrower than the filter bandwidth $\Delta\lambda_{BPF} = 1.3$ nm. Therefore, different polarization states can place the lasing peak of the laser in a broad range of places within the filter bandwidth which do not correspond to the exact central part of the filter. The TBP of the pulses in Fig. 4.11 (a) and (b) did not change

significantly for different pulse widths and had values of ~ 0.60 and ~ 0.57, respectively.

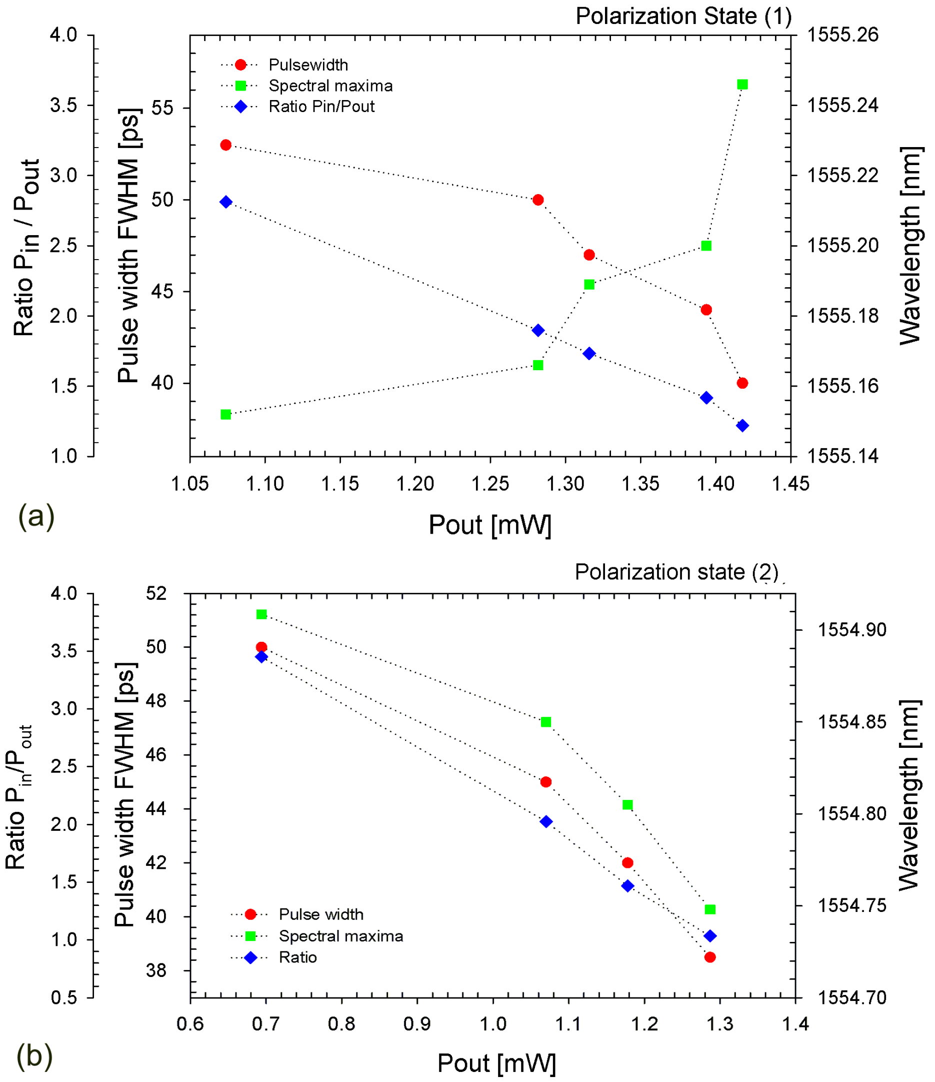

Figure 4.11: Pulse width FWHM, spectral maximum position and coupling ratio P_{in}/P_{out} as a function of the output power P_{out} for two different polarization states in the cavity. (a) Polarization state (1) and (b) polarization state (2). P_{in}: Intracavity power.

4.3.2.3 Pulse width and optical bandwidth as a function of the driving frequency

In order to study the dependence of the pulse width as a function of the frequency shift, two more fiberized AOMs with different driving frequencies (f_{AOM} = + 80 MHz and + 200 MHz) were spliced into the cavity shown in Fig. 4.7 (a). The different laser cavities showed identical behavior as the cavity described in Section 4.3.2.1. In all the cases, self-starting fundamental ML was achieved at high pump powers, and therefore reduction of pump power was necessary in order to reduce the number of pulses in the cavity. Fig. 4.12 (a) shows the pulse width and spectral bandwidth of the output signal as a function of the AOM driving frequency. The graphic shows a decrease in the pulse width and a broadening of the optical bandwidth for higher frequency shifts. Pulse widths of τ_{FWHM} $\sim$ 58 ps with TBP $\sim$ 0.56, and τ_{FWHM} $\sim$ 35 ps with TBP $\sim$ 0.63 for the f_{AOM} = -80 MHz and f_{AOM} = -200 MHz AOMs were obtained, respectively. Fig. 4.12 (b) shows the shape of the optical spectrum measured for the three AOMs. The figure shows that the *hump* on the longer wavelength side of the spectra is always present regardless of the AOM spliced in the cavity. In addition, the distance between the spectral maximum and the *hump* grows as the frequency shift mechanism in the cavity increases. Fig. 4.12 (a) also shows the results for a cavity without an intracavity BPF. These results will be further explained in the next section. Pulse width measurements for these configurations presented a higher TBP $\sim$ 0.69 compared to the results obtained with the fiberized BPF.

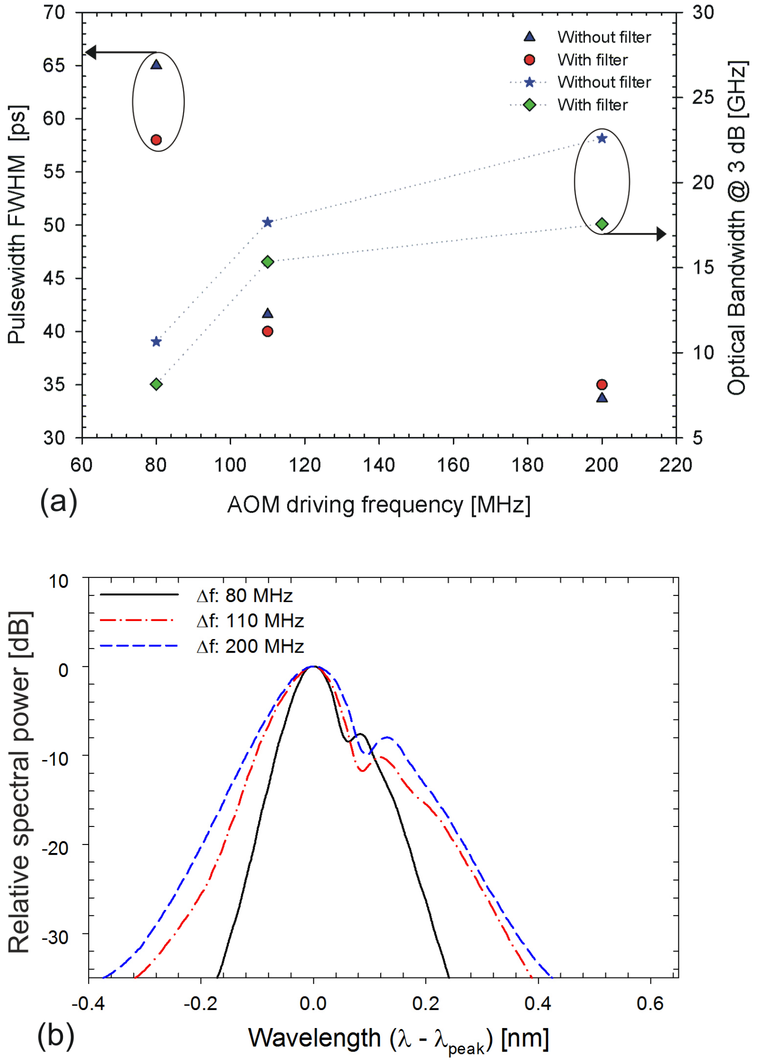

FIGURE 4.12: (a) Pulse width FWHM and optical bandwidth as a function of the AOM driving frequency of a FSF ring laser cavity with and without optical filter. (b) Pulse spectra for three AOMs with different downshifting frequency mechanism ($f_{AOM} = -80$ MHz, $f_{AOM} = -110$ MHz, and $f_{AOM} = -200$ MHz).

4.3.2.4 Multi-wavelength regime

The cavity shown in Fig. 4.7 (a) was also tested without a BPF. For all three AOMs, the laser presented multi-wavelength behavior which was attributed to the partly inhomogeneous line broadening of the erbium-doped medium [81]. ML behavior was achieved at all times for the fundamental repetition rate of the cavity. Fig. 4.13 (a) shows the optical spectrum obtained with a 200 MHz downshifted frequency AOM spliced in the cavity. The spectrum corresponds to the ML signal generated by the laser. Although the optical spectrum shown in Fig. 4.13 (a) presents different lasing peaks the only peak that is ML is the highest peak with an asymmetric shape. This is clearly seen in Fig. 4.13 (b), where the central peak of the multi-wavelength spectrum is shown. For this graph, the AOM used had an 80 MHz downshifting mechanism and the pulses generated in the cavity yield pulse widths of FWHM $\sim$ 65 ps. The pulse width and optical bandwidth measurements for these configurations are summarized in Fig. 4.13 (a).

4.3.2.5 Tunable laser

Tunability of the laser signal, over a range of 30 nm, was possible with help of the filter spliced in the cavity (see Fig. 4.7). Pulse width measurements were carried out for every 5 nm. For this configuration, the AOM used had a driving frequency of $f_{AOM} = -110$ MHz. Fig. 4.14 shows the pulse width measurements carried out over the entire tuning range of the laser (1535 - 1565 nm). The scatter data represents the average pulse width, while the "error bars" show the minimum and maximum pulse width obtained at a specific wavelength by adjusting the polarization state of the cavity. The inset of the figure shows a broader view of the tunable laser. It is worth mentioning that the pulse width behaviour shown in Fig. 4.14 follows the small-signal gain spectral shape obtained for a $\sim$ 60% of population excitation of the Er-ions.

4.3.2.6 Frequency-shifted feedback laser with narrow band-pass filter

The dependence of the pulse width and pulse spectra for narrower BPFs was also investigated. Therefore, the fiberized BPF was replaced by a FBG with a spectral bandwidth of $\Delta\lambda_{BPF} = 0.45$ nm and reflectivity R = 99%. In order to use the FBG reflection spectrum, the laser ring cavity was modified into a sigma cavity configuration with help of a three port circulator (see Fig. 4.7 (b)). The behavior of the laser signal was studied for three different AOMs with downshift mechanisms of f_{AOM} = -80 MHz, -110 MHz and -200 MHz, and its signal was monitored with help of an OSA, and DCA. ML behavior in all three cases appeared for pump powers $P_p \geq 200$ mW. Once the laser was ML, it was possible to decrease the pump power to $P_p \sim 140$ mW. However, below this value, ML was no longer supported in the cavity. The narrower filter bandwidth of the FBG allowed for a better monitoring of the relative position of the spectral maximum within

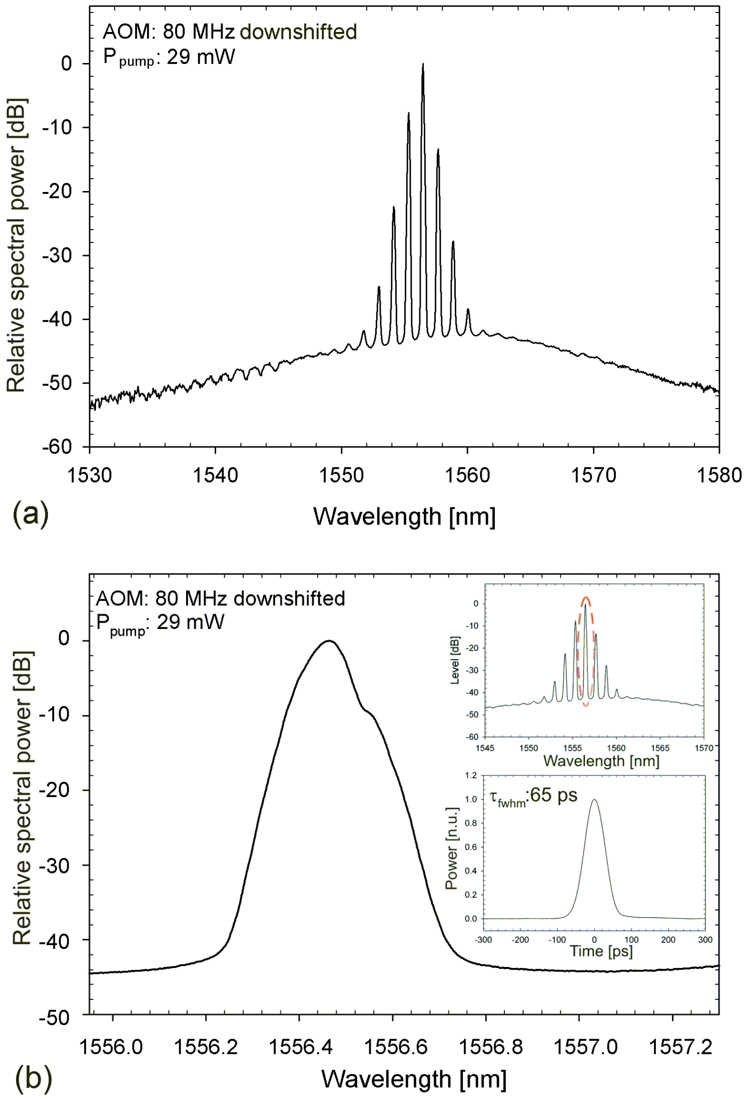

FIGURE 4.13: Optical spectra of a FSF ML fiber laser without an intracavity filter for (a) 200 MHz downshift AOM and (b) 80 MHz downshift AOM. Upper inset in (b) shows a broader span of the central lasing peak of the signal. Lower inset in (b) shows the optical pulse generated by the laser.

the filter bandwidth, and therefore provided a better understanding of the effects of the spectral shifting mechanism in the cavity. Fig. 4.15 (a) shows the FBG reflection spectrum (black solid line) together with the pulse spectra of the laser cavity operating in ML regime for the three different AOMs described previously. The spectra observed for the downshifts f_{AOM} = -80 MHz and f_{AOM} = -110 MHz differ from the results shown in the former sections. Here, although the spectral maximum is localized on the shorter wavelength side (see inset of Fig. 4.15 (a)), there is no clear evidence of a *hump* formation on the longer wavelength side of the spectrum. Instead, a single peak in the lasing spectrum was observed with a slightly higher intensity level on the shorter wavelength side. The time traces observed on the DCA were also different from the previous results. Compare for example, the blue dashed trace and the red solid trace on Fig. 4.15 (b)

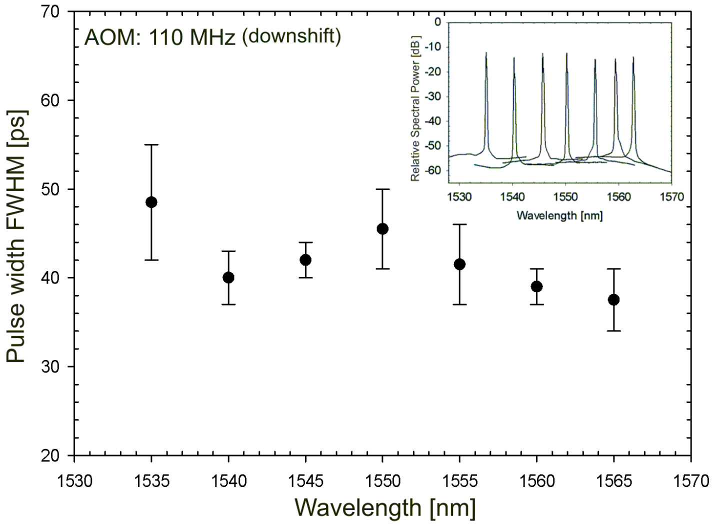

Figure 4.14: Pulse width measurements along the entire tuning range of the FSF laser. The inset shows the optical spectra of the laser plotted over the same tuning range.

with the traces on Fig. 4.10 (b). The pulse spectral bandwidths measured at FWHM were $\Delta\lambda = 0.076$ nm and $\Delta\lambda = 0.102$ nm for frequency shifts of f_{AOM} = -80 MHz and f_{AOM} = -110 MHz, respectively. Therefore, pulse widths wider than $\tau_{FWHM} > 46$ ps and $\tau_{FWHM} > 34$ ps were expected in the time trace. However, pulses $\tau_{FWHM} > 430$ ps were emitted in these configurations (see for example, Fig. 4.15 (b)). An autocorrelator was not available at the moment these experiments were carried out; hence, it was not possible to analyze the substructure of the ML pulses observed on the DCA. However, based on the measurements of the pulse bandwidths and the fact that the laser is operating at high pump powers, it is assumed that the broad pulse measured with the DCA is formed by a group of clustered pulses with almost no separation between them.

Although this operation regime is different from the one observed with broader filter bandwidths,it is possible to link both regimes by looking at the performance of the laser operating with the f_{AOM} = -200 MHz AOM. In this configuration, the pulse spectrum formed a main peak with a spectral bandwidth of $\Delta\lambda = 0.04$ nm and a broad shoulder on the longer wavelength side 10 dB below the level of the spectral maximum. The time trace observed on the DCA showed a similar behavior as the results observed for broader filter bandwidths (see Fig. 4.9 (a)). However, in this configuration the distance between pulses is much shorter, causing an overlap between the pulses -see for example, the green dash-dotted line in Fig. 4.15 (b). The individual pulse widths measured at FWHM were $\tau_{FWHM} \sim 93$ ps, yielding a TBP of ~ 0.46.

As mentioned in Section 4.3.2.1, the f_{AOM} = -200 MHz AOM presented higher insertion loss than the rest of the AOMs. Hence, it is possible to consider that the AOM excess

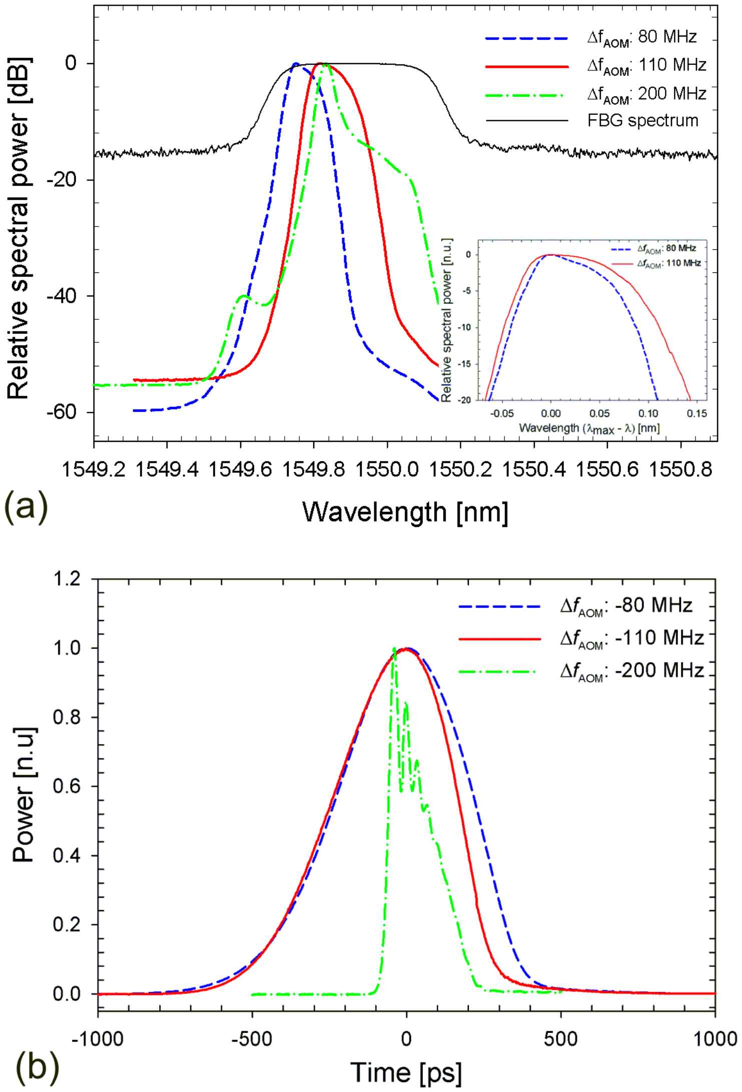

FIGURE 4.15: (a) Optical spectrum and (b) time trace of ML pulses formed in a FSF laser using AOMs with different frequency shifts. Blue dashed trace: f_{AOM} = -80 MHz, red solid line: f_{AOM} = -110 MHz, and green dash-dotted line: f_{AOM} = -200 MHz. The black solid line in (a) shows the reflection spectrum of the band-pass filter of the cavity, while the inset shows a close up of the pulse spectra of the lasers using the -80 MHz and -110 MHz AOMs

loss, together with the increment in the frequency shift mechanism, imposed a restriction in the amplification of the spectral components located on the longer wavelength side of the spectrum. Therefore, the shoulder formed on this side of the pulse spectrum remained at a lower level with respect to the spectral maximum. This effect is not seen for the two other AOMs, where it is clear that the longer wavelength side is amplified almost to the same level as the spectral maximum. This performance can be better observed in the inset of Fig. 4.15(a). Hence, the formation of the broader pulses observed for the configurations with the f_{AOM} = -80 MHz and f_{AOM}= -110 MHz AOMs are a clear consequence of the amplification of the spectral components situated at the longer wavelength side of the spectrum, where the spectral components are constantly transferred by the AOM.

4.3.3 Optical filtering of the laser spectrum

In order to study in more detail the structure of the pulses formed in Section 4.3.2.1, the pulse spectrum was spectrally filtered by splicing a fixed high reflective FBG with $\Delta\lambda_{BPF} = 0.08$ nm bandwidth at the output of the FSF laser. An optical circulator helped to obtain the reflection of the filtered spectrum from the laser output. The tunable band-pass filter spliced in the cavity allowed to tune the laser signal through the FBG spectrum. A tuning of $\sim$ 0.3nm was enough to cover the entire pulse spectrum and to monitor the behaviour of the pulse in the time domain. The filtered signal had not enough power to be monitored in the DCA, therefore the filtered spectrum had to be amplified with an EDFA. Fig. 4.16 (a) shows the pulse spectrum for different lasing wavelengths (colour dashed lines) before being filtered by the FBG (blue solid line). The figure helps to visualise the position of the pulse spectrum within the bandwidth of the FBG. The corresponding time trace for each filtered section of the pulse spectrum is shown in Fig. 4.16 (b). Pulses are arbitrarily shifted in time in this figure to have a clearer view of each pulse. Filtered pulses presented at all time a small satellite pulse at the trailing edge. I believe, this pulse is a result of the 3rd-order spectral phase and its manifestation is more prominent in these traces due to the EDFA action. The pulse width of the filtered pulses is $\tau_{FWHM} \sim 90$ ps, and has a TBP of ~ 0.45; a value quite close to a transform limited Gaussian pulse. One interesting feature of the spectral filtering is the one observed for the spectral maximum $\lambda_0 = 1548.1975$ nm (green dashed line in Fig. 4.16 (a) and (b)). For this wavelength, the optical filter is centred at the split between the main peak and the *hump* of the pulse spectrum. Time traces for this spectral position show two pulses with different intensities and pulse width slightly separated from each other. The time trace obtained for this portion of the spectrum shows its complex spectral phase caused by the interaction of the frequency shifting mechanism, the pulling effect of the filter bandwidth and the SPM inside the cavity.

4.4 Discussion

The design and implementation of a stable picosecond source with a FSF technique allowed studying its dynamics in the ML regime and to monitor the behaviour of the pulse asymmetry in the optical and temporal domain as functions of different cavity parameters. Based on the numerical simulations presented in Chapter 5; the asymmetric shape of the spectra shown in Fig. 4.8 (a) and (b), are a consequence of the equilibrium reached by the frequency shifting mechanism applied to the optical field in every round-trip and the shift of the spectral maximum acquired by the frequency-dependent

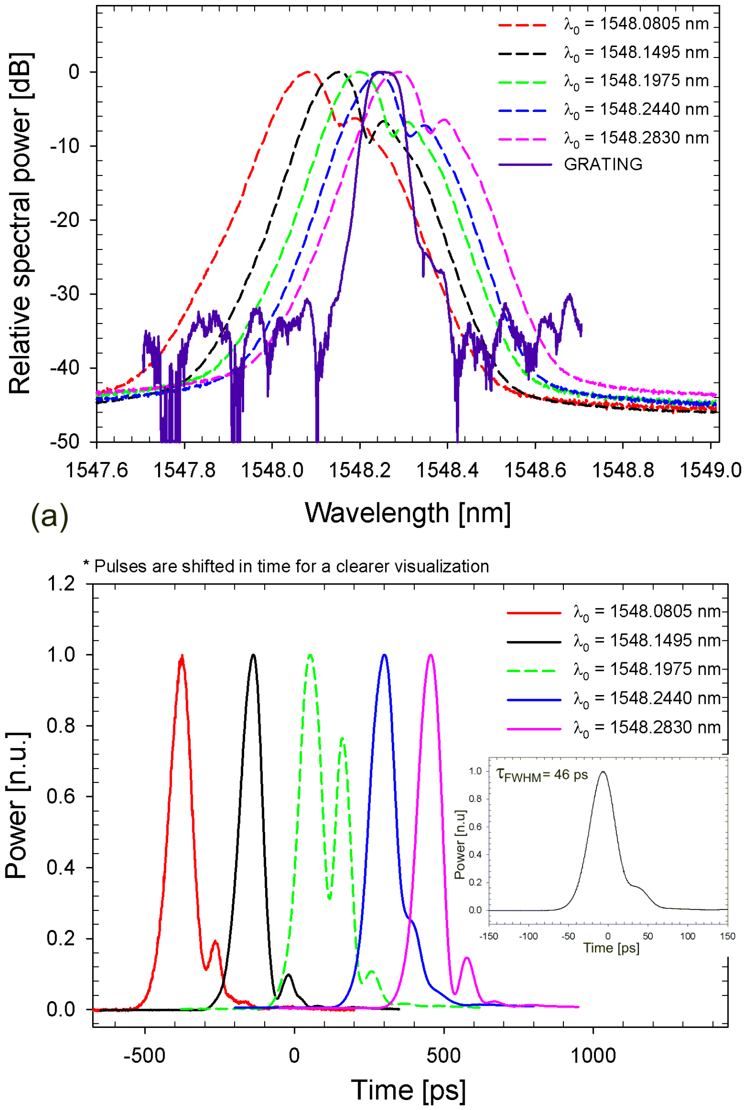

Figure 4.16: (a) Optical spectra and (b) pulse intensities for different wavelengths of the laser signal. The pulse spectra shown here are measured before the FBG, while the pulse intensities are measured after the FBG.

gain/losses of the cavity. The *hump* observed in these figures is more likely to appear when the frequency-dependent gain in the cavity is not enough to amplify the far end of the spectrum where the frequency components are being shifted at every round-trip (in this case, the longer wavelength side of the spectrum). Under these conditions, the asymmetry of the pulses resembles those shown in Fig. 4.9 (a) and Fig. 4.10 (b). For this case, the asymmetry of the pulse depends more on the shape of the *hump* situated on the longer wavelength side of the spectrum, than on the stronger filtering effect performed over the longer wavelength side of the spectrum.

Regarding the shape of the *hump* on the pulse spectrum and its relation with the pulse asymmetry, it is clear that a pulse will become more asymmetric as the split between the *hump* and the spectral maximum increases. Adjustments in the polarization state of the cavity (polarization-dependent losses) modify the shape of the *hump*, and therefore control the asymmetry and width of the pulse. Shorter pulses present broader bandwidths in the central part of the pulse spectrum and on the *hump*. This same effect is observed in the numerical simulations presented in Chapter 5 and it is attributed principally to SPM. Numerical simulations show that shifts of the spectral maximum to the shorter wavelength side is mainly caused by the broadening of the *hump*. This means that the hump pushes the section of the spectrum, where the spectral maximum is localized, towards the opposite direction of the frequency shifting process. Still, we have to bear in mind that frequency and polarization-dependent losses in the cavity play a major role in shifting the spectral maximum. This might explain the different behaviour of the spectral maximum shift in Fig. 4.11 (a) and (b).

Different behaviour of the optical spectrum and pulse shape was observed for narrower filter bandwidths. For these configurations the cavity frequency-dependent gain was able to amplify the far end of the spectrum, avoiding the formation of a *hump*. Therefore, broad pulses observed in Fig. 4.15 (b) are a consequence of the excess gain generated inside the cavity and of the strong filter dispersion applied over the pulse spectrum. In order to understand why we observe pulses with pulse-width in the range of hundreds-of-ps, (see Fig. 4.15 (b)) we have to consider two things. Firstly, fundamental ML was only possible at $P_p \geq 200$ mW, which is 50 mW above the pump power required to mode-lock the laser configurations with broader BPFs. At this high pump power, cavities with broadband filters always showed groups of clustered pulses separated by a short distance between them. Therefore, it is likely that the broader pulses are indeed formed by compact groups of pulses with pulse distances reduced due to the strong filter dispersion applied over the pulse spectrum. In addition, the pump power $P_p = 150$ mW at which fundamental ML stops, is still too high to observe a single pulse circulating in the cavity. Therefore, the broad pulse observed cannot be considered as a single entity. Regarding the shape of the pulses generated in these configurations, in Chapter 5 a simple numerical simulation proposes an answer to the shape behaviour of the broader pulse as a function of the distance between the compact groups of pulses of which the broader pulse is formed. The results obtained with the 200 MHz downshifted frequency AOM give further evidence of the effects of the spectrum amplification and filter bandwidth over the pulse shape. In this configuration, the frequency-dependent losses of the AOM and cavity do not allow the amplification of the far end of the spectrum. In this situation, the pulses follow the same behaviour as in the cavities with broad BPF. However, in this case, the distance between the clustered pulses is shorter, but still wide enough to avoid a complete pulse overlap. Therefore, it is possible to think that as the longer wavelength side of the spectrum is amplified and the pulse spectral maximum pushed in the opposite direction of the frequency shifting mechanism, the clustered pulses in the group are pulled closer to each other forming what appears in the DCA as a single pulse.

4.5 Conclusions

In this Chapter, a stable tunable Er^{3+}-doped FSF laser delivering picosecond pulses was proposed and built. The stability of the source allowed a much insightful analysis of the shape of the pulse spectra and pulse intensity as functions of different parameters of the laser cavity (filter bandwidth, frequency shift, and coupling ratio), compared to previous experimental works [8, 53, 86]. Results show that not only broader filter bandwidths and higher frequency shifts lead to shorter pulses (in agreement with [8, 53]), but also shorter pulses can be achieved by keeping the coupling ratio of the cavity close to unity. In addition to this, the results presented in this Chapter show a more graphical and therefore intuitive analysis of the optical pulse shape and its relation with the pulse intensity that has not been addressed in the literature before. For example, results show that for broad intracavity filter bandwidths the shape of the spectrum tends to split and form a *hump* on the longer (shorter) wavelength side due to the downshift (upshift) frequency mechanism of the AOM. In this regime, the *hump* is mainly responsible of the strong asymmetry on the trailing (leading) edge of the pulse in the time domain. The fact that the spectrum seems to split in two is due to the frequency dependent losses of the cavity which do not allow this section of the spectrum to be amplified while the laser is mode-locked. In contrast, for narrow filter bandwidths results showed that the pulse spectrum does not split and the side of the spectrum where the spectral components are constantly shifted can be amplified to a level close to the spectral maximum. Identification of these characteristics in the optical spectrum (which have not been addressed in the literature before) is important because of its inherent relation with the pulse intensity. Therefore, while in the first regime (broadband filters), a clustered train of coherent optical pulses with a clear separation between them was achieved, in the second regime (narrowband filters) the separation between pulses was almost canceled forming a single broad pulse of hundreds of picoseconds. This shows for the first time (in an experiment) how the filter-induced dispersion and filter-induced losses in a FSF lasers play a fundamental role in determining the minimum separation between clustered adjacent pulses.

The results obtained in this Chapter provide novel insights in the behaviour of FSF lasers and are useful to explain former published results regarding these lasers. Furthermore, these results show the possibility to generate multi-functional stable sources by choosing the appropriate parameters in the cavity. For example, ML multi-wavelength sources by means of a Fabry-P$\acute{e}$rot filter, or use the benefits of the AOM to amplitude modulate the cavity and generate Q-switched ML laser.

Chapter 5

Numerical simulations of a frequency-shifted feedback laser

In this Chapter I present numerical simulation studies on pulse formation in an Er^{3+}-doped frequency-shifted feedback (FSF) fibre ring laser. In particular, I focus on the development and behaviour of the pulse spectrum and its relation to the pulse shape in the time domain for different parameters of the laser cavity. The numerical results shown here are compared with the experimental data of Chapter 4 allowing a better understanding of the formation and asymmetry of the optical pulses generated in FSF lasers. In the first part of this Chapter, I give a brief summary of previous theoretical work and numerical models for FSF lasers. I also describe the numerical model used for the simulations and the values given to the different parameter of the simulation. The numerical results are discussed in terms of the asymmetry of the optical spectrum and pulse shape as functions of the frequency shift and filter bandwidth of the cavity. The results are also compared to previous analytical models and it is shown that the numerical model is able to describe properly the behaviour of FSF lasers using broad filter bandwidths.

5.1 Review of theoretical work for frequency-shifted feedback lasers

Theoretical investigations of FSF lasers have used different models to describe the output characteristics of such lasers in their different operating regimes [8, 74, 98, 101–103]. For example, at low pump power, where FSF lasers present broadband cw output, the rate-equation models of Bonnet et al. [98], and Stellpflug et al.[74], offer a good description of the dynamics. However, as the rate equation model lacked phase information, it could not describe the mode-locked regime of these lasers. The work of Nakamura et al.

(*Moving comb model*) [103], and Yatsenko et al. (*discrete-frequency model*) [102] considered phase information of the electric field, and were able to show steady-state pulse formations for specific parameter conditions; still both models did not consider phase shifts generated by nonlinear elements in the laser cavity. A first approach to analyse the behaviour of FSF lasers in the mode-locked regime was carried out by Kodama et al., [101]. In this work the authors compared the behaviour of mode-locked FSF lasers with that of solitons in sliding-frequency guiding filters for long haul telecommunication systems [96]. In these papers, pulses were analysed using soliton perturbation theory yielding analytical solutions for stable pulse formation. Because the analysis was based on soliton theory, it was relevant for the anomalous dispersion regime. However further work [8, 86, 97] showed that FSF lasers could operate in both dispersion regimes (normal and anomalous). The Kerr nonlinearity (SPM) as a key element to the pulse behaviour in the laser cavity was first studied in detail in [8]. In this work the authors also presented numerical and experimental results regarding the behaviour of the output signal of a Nd^{3+} fibre laser for different parameters of the laser cavity. Pulses generated in FSF lasers present an asymmetry observed in the optical spectrum, which is a consequence of the quadratic frequency chirp imposed by the frequency shifter [97] and the filter dispersion [96] in the cavity. Although this is a well-known characteristic of FSF lasers, there is little work that has linked experimental results [8, 86, 98] with analytical models describing the asymmetries observed in the pulse spectrum. In addition, pulse behaviour observed in the experimental results did not match analytical solutions or asymmetries observed in previous work. Therefore, it was necessary to implement numerical simulations with the experimental parameters presented in Chapter 4, and corroborate our results with previous analytical work. In the next section I briefly disccus the model of Kodama et al. [101] based on soliton perturbation theory and explain why this model cannot be applied to predict the evolution of the soliton amplitude and frequency. The results presented in this Chapter are also compared with those of de Sterke et al. [97], where pulse formation was studied without any reference to cavity dispersion.

5.2 Theoretical analysis of FSF lasers using soliton perturbation theory

A mode-locked all-fiber ring laser with large net anomalous dispersion in its cavity is more likely to generate soliton type pulses. Optical solitons are formed due to the interplay between the dispersive and nonlinear properties of the laser cavity, and their interaction is well described by the non-linear Schrödinger equation (NLSE). In a FSF laser, the effects of frequency shifting, and gain bandwidth can be considered as perturbations to the soliton solution of the NLSE, allowing to obtain an analytical solution for pulse behavior in FSF lasers.

Pulse propagation in a fibre laser ring cavity with a continous frequency-shifting mechanism, and a bandpass filter, can be described in dimensionless units by the averaged NLSE [104]:

$$\frac{\partial u}{\partial Z} - \frac{i}{2}\frac{\partial^2 u}{\partial T^2} - i\,|u|^2\, u - i\alpha\, T\, u \;=\; \delta\, u + \beta\,\frac{\partial^2\, u}{\partial T^2} + \gamma\,|u|^2\, u. \tag{5.1}$$

where $u(Z,T)$ is the average amplitude of a guiding-center soliton normalized to the soliton amplitude [104, 105], Z is a distance scale normalized to the dispersion length $L_D = \tau_0^2/\,|\beta_2|$, $T = (t - z/v_g)\,/\tau_0$ is the retarded time frame moving with the pulse at the group velocity v_g normalized to a time unit τ_0, α is the frequency shifting rate, δ is the cavity gain, β is the filter-induced losses, and γ is related to the physical value of the cavity nonlinear gain. The dimensionless parameters α, β and γ in equation 5.1, are defined as:

$$\begin{aligned}
\alpha \;&=\; \frac{(2\,\pi\,10^{-6})\,f_{AOM}\,\tau_0^3}{L_c\,\beta_2},\\
\beta \;&=\; \frac{2}{\beta_2\,\Delta\nu_{BPF}^2\,L_c},\\
\gamma \;&=\; \frac{\gamma_1\,P_0\,\tau_0^2}{\beta_2}.
\end{aligned} \tag{5.2}$$

where, f_{AOM} is the net AOM frequency shift(MHz), τ_0 is related to the soliton FWHM pulse width by $\tau_0 = \tau_{FWHM}/1.763$ (ps), L_c is the length of the ring cavity (km), β_2 is the fibre GVD parameter (ps^2/km), $\Delta\nu_{BPF}$ is the angular filter bandwidth ($2\,\pi$ THz), γ_1 is the nonlinear gain coefficient(W^{-1}km^{-1}), and P_0 is the soliton peak power (W).

The left-hand side of Eq. 5.1 represents the NLSE with a linear potential given by α, and its solution without considering any perturbation ($\delta\; = \beta\; = \gamma\; =\; 0$) yields the following soliton equation [101]:

$$u(Z,T) = \eta\; sech\,\{\eta[t - \xi(Z)]\}\; exp[i\kappa(Z)T \;+\; i\psi(Z)], \tag{5.3}$$

where $\xi = \alpha Z^2/2$ represents the soliton position, $\kappa = \partial\xi/\partial Z$ is the soliton frequency and ψ is related with the amplitude and frequency of the soliton by $\partial\psi/\partial Z = (\eta^2 - \kappa^2)/2$. However, in the presence of small perturbations caused by a bandwidth-limited gain and nonlinear medium, perturbation theory can be used to analyse the evolution of the amplitude η and frequency κ of the soliton. The evolution equations for η and κ in the Z coordinate are given by [106]:

$$\begin{aligned} \frac{d\eta}{dZ} &= 2\delta\,\eta \;-\; 2\beta\,\eta\left(\frac{\eta^2}{3} + \kappa^2\right) + \frac{4}{3}\,\gamma\,\eta^3, \\ \frac{d\kappa}{dZ} &= \alpha \;-\; \frac{4}{3}\,\beta\,\eta^2\,\kappa. \end{aligned} \tag{5.4}$$

Analysis of FSF laser with perturbation theory is limited to small values (< 1) of α, β and γ. The values of these parameters, as shown in Eq. 5.2, are determined mainly by cavity parameters. Therefore, one should be aware that if the experimental parameters of the system under investigation yield large values of α, β, or γ, perturbation theory may no longer be useful to predict the evolution of the soliton in such system. Equation 5.2 shows that smaller values of β can be achieved by increasing the filter bandwidth. For example, increasing $\Delta\lambda_{BPF} >$ 4nm while keeping the other parameters constant, yields values of $\beta < 1$; values which are acceptable for calculations with perturbation theory. Nevertheless, calculation of the parameter α, using the experimental data for pulse width τ_{FWHM} = 35 ps and AOM frequency shift f_{AOM} = -200 MHz, yields a value of $\alpha \sim 41$. Therefore, for the system under investigation shown in Chapter 4 perturbation theory is not an appropiate tool for analysing the pulse evolution of such system.

In order to have a better understanding of the dynamics of the laser behaviour, and to predict more accurately the experimental results obtained in Section 4.3.2; a numerical model was implemented matching the experimental conditions of the laser cavity. The numerical model is performed using a co-simulation between Matlab and commercial software VPI Transmission Maker. The latter is used to generate the optical signal and to simulate the optical fibre amplifier in the cavity.

5.3 Numerical model

The numerical model is based on independently simulating every element of a FSF laser cavity like the one shown in Fig. 4.7. Although the numerical model does not allow to obtain an analytical solution of the steady-state of the laser system, it allows to track the behavior of the electric field as it passes through every elements in the cavity. Under specific operation conditions, the numerical model can generate stable (steady-state) optical pulses circulating at the fundamental repetition rate of the ring cavity. The parameters of the numerical model correspond to a great extent to the experimental setup described in Chapter 4. However, at this point, the numerical model takes into account only a single polarization component traveling in the ring cavity. Hence, the saturable absorption effect generated by the NLPE is not considered in this first model. The numerical model starts from an initial arbitrary complex optical field (e.g. transformed limited $sech^2$ pulse or white noise process). After a cavity round-trip, the resulting signal is then used as input for the next cavity-round trip calculation until the signal reaches a steady-state. VPI Transmission Maker software uses the analytic signal approximation to represent optical processes. This yield a complex optical field that is given by:

$$E(t) = \sqrt{P(t)} \cdot exp(-j2\pi\Delta\nu t) \tag{5.5}$$

where $\Delta\nu$ is the offset between the emission frequency and an optical reference frequency ν_{ref} (defined by the user), and $P(t)$ is the optical power of the waveform. VPI Transmission Maker software normalizes the optical fields such that their modulus-square represents optical power $P(t) = |E(t)|^2$.

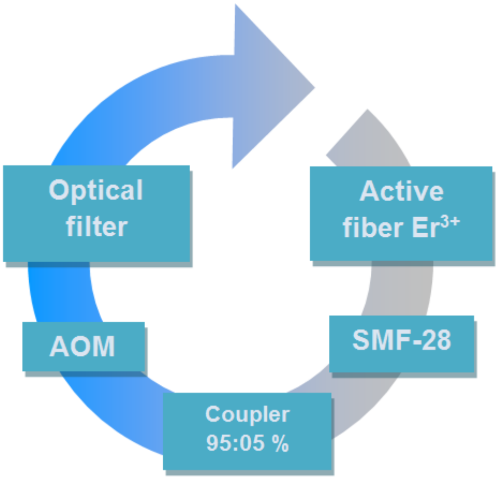

FIGURE 5.1: Schematic of the FSF laser elements used for the numerical simulations.

The description of each of the elements in the cavity is as follow: the active fiber is formed of a piece of 2-m long (L_{EDF}) Er^{3+}-doped fibre which is described by a stationary model based on a unidirectional propagation equation for signals and a two-level rate equation for ion populations. The emission and absorption spectra are specified in terms of the Giles parameters [107] of the Er^{3+} fiber used in the experiment shown in Chapter 4. The model for the Er^{3+}-doped fibre can simulate the effect of Kerr nonlinearity on the signal propagating throughout the gain fibre. The model takes into account the effect of self-phase modulation (SPM) according to the following equation:

$$\frac{\partial E(z,t)}{\partial z} = i\gamma \left|E(z,t)\right|^2 E(z,t) \tag{5.6}$$

where $E(z,t)$ denotes the slowly-varying complex-envelope of the optical field and γ is the nonlinear coefficient of the fibre at the carrier frequency. γ is calculated as

$$\gamma = \frac{2\pi n_{nl}\nu}{cA_{eff}} \tag{5.7}$$

where n_{nl} is the nonlinear refractive index of the active fibre and A_{eff} is the effective core area of the fibre. In addition, the model for the Er^{3+}-doped fibre also accounts for spontaneous emission. For this specific amplifier model it was assumed that the overlap integral between the optical mode and inversion ions were independent of the signal power. In such case, the excitation level is given by [108]:

$$\frac{n_2}{N_t} = \frac{\sum_k \frac{P_k^*(z)\alpha_k}{h\nu_k\zeta}}{1+\sum_k \frac{P_k^*(z)(\alpha_k+g_k)}{h\nu_k\zeta}} \tag{5.8}$$

where n_2/N_t is the excited Er^{3+} inversion level ratio, P_k^* is the total power $P_k^* = P_k^s + P_k^p + P_k^{+ase} + P_k^{-ase}$, including the co-propagating signals, pump and amplified spontaneous emission (ASE), and the counter propagating ASE at frequency ν_k, g_k and α_k are the fiber wavelength dependence gain and absorption of the Er^{3+} fiber (Giles parameters), h is the Planck's constant and ζ is the saturation factor of the fiber defined as $\zeta = \pi b_{eff}^2\ N_t/\tau$, where b_{eff} is the effective radius of the dopant distribution, τ is the lifetime of the metastable level, and N_t is the total Er^{3+} ion concentration. The spatial evolution of the optical field along the active fiber is described by the following propagation equations [108]:

$$u_k^{\pm}\frac{\partial P_k^{p,s}}{\partial z} = [g_k+\alpha_k]\,\frac{n_2}{N_t}P_k^{p,s} - (\alpha_k P_k^{p,s}) \tag{5.9}$$

$$u_k^{\pm}\frac{\partial P_k^{ase\pm}}{\partial z} = [g_k+\alpha_k]\,\frac{n_2}{N_t}P_k^{ase\pm} - (\alpha_k P_k^{ase\pm}) + \frac{g_k n_2 P_{ASE,k}^0}{N_t} \tag{5.10}$$

where P_k^s is the co-propagating power of the optical pump/signal at frequency ν_k, $P_k^{ase\pm}$ is the co-counter propagating power of the amplified spontaneous emission (ASE) centered around the frequency ν_k, with bandwidth $\Delta\nu_k$, $P_{ASE,k}^0 = 2h\nu_k\Delta\nu_k$ is the noise power propagating in a given direction, spontaneously emitted at any given point along the fibre. The total ASE power at a point z along the fibre, given by Eq. 5.10, is the sum of the ASE power from previous fibre sections and the added local noise power $P_{ASE,k}^0$. The ASE power centered at frequency ν_k is propagated as one signal with an input power of 0 at $z = 0$ for co-propagating ASE and another signal with an input power of 0 at $z = L_{EDF}$ for the backward-propagating ASE (L_{EDF} is the length of the active fibre). Finally, $u_k^{\pm}$ is the constant equal to 1 for forward-propagating waves, and -1 for backward-propagating waves. The ordinary differential equations (ODEs) shown in Eq. 5.9 and Eq. 5.10 are solved by the commercial software. Although the user manual for this software does not specify the method used to solve the ODEs, such systems can be solved numerically with a typical fourth-order Runge-Kutta method [109].

A segment of SMF-28 fiber follows the gain fiber. Pulse propagation within this segment is modeled with the nonlinear Schrödinger equation (NLSE) for linearly polarized optical waves, using the split-step Fourier method described in Chapter 2 of [41]. The NLSE for the model takes the form [41]:

$$\frac{\partial E(z,t)}{\partial z} = -\frac{\alpha_{loss}}{2}E(z,t) - \frac{i}{2}\beta_2\frac{\partial^2 E(z,t)}{\partial t^2} + \frac{1}{6}\beta_3\frac{\partial^3 E(z,t)}{\partial t^3} + i\gamma\left|E(z,t)\right|^2 E(z,t) \quad (5.11)$$

where $E(z,t)$ denotes the slowly-varying complex-envelope of the optical field, β_2 is the group-velocity dispersion (GVD) coefficient, β_3 is the GVD slope, α_{loss} is the fiber loss, and γ is the nonlinear parameter of the fiber at the carrier frequency ν_{ref}. The pulse amplitude is reduced by a 5% after the fiber section in order to account for the optical coupler (95:05) spliced in the experimental setup. The frequency shift induced by the AOM (f_{AOM}) is modeled by shifting each of the frequency components of the optical signal by "n" times the space between two adjacent frequency components $\nu_{step} = \nu_k - \nu_{k-1} = 19.53125$ MHz. Finally, the optical filter is modeled by a bandpass Gaussian filter centered at ν_c and with bandwidth $\Delta\nu_{BPF}$ measured at FWHM. The Gaussian filter is modeled in the frequency domain as an analog filter with the transfer function $H(2\pi\nu_k) = e^{-ln\sqrt{2}|2\nu_k|^2}$ and a zero phase response.

The following parameters were considered for the simulations in order to match the experimental conditions in Chapter 4: $L_{EDF} = 2$ m, Er^{3+} fiber Giles parameters (α_k and g_k) are taken from the specifications of a commercial Fibercore I-25 fiber with peak absorption of $\alpha_{1530} = 37.2$ dB/m at 1530 nm, NA of 0.24, cut-off wavelength $\lambda_{off} = 946$ nm, and mode field diameter (MFD) of 5.6 μm. The calculated saturation factor was $\zeta = 2.6\text{x}10^{16}$ $(\text{ms})^{-1}$ assuming a value of $N_t = 3.776\text{x}10^{25}$ ions/m^3, and $\tau_{LT} = 10$ ms. Calculation of N_t considered an Er^{3+} dopant radius equal to the fiber core radius. The pump signal wavelength was $\lambda_p = 1480$ nm and its power P_p was optimized to give a small-signal gain of G $\sim$ 22 dB. This parameter was later on modified in order to obtain a single pulse circulating inside the cavity. The parameters for the fiber are: $L_{smf} = (c/1.45)\nu_{step} - L_{EDF}$, $\alpha_{loss} = 0.2$ dB/m, $\beta_2 =$ -15 ps^2/km, $\beta_3 = 0.1647$ ps^3/km and $\gamma_1 = 1.1$ W^{-1}km^{-1}. Finally, for the optical filter the values given are $\nu_{ref} = 193.1$ THz (1552.5 nm) and $\Delta\nu_{BPF}$= 20-120 GHz.

Numerical results presented in this Chapter are shown in wavelength units rather than frequency in order to facilitate the comparison between the experimental results obtained in Chapter 4.

5.4 Numerical simulation results

5.4.1 Steady-state solutions for different initial conditions

To test whether different initial conditions lead to similar steady-state solutions, two different initial conditions (IC) - 1) Time-bandwidth limited $sech^2$ pulse, and 2) Gaussian-distributed white noise source- were used for a given set of cavity parameters. The model converged to the same "steady-state" (stationary) solution for both initial conditions for a specific range of cavity parameters. Fig. 5.2 shows the spectral bandwidth of the optical signal plotted as a function of the pulse width after each cavity round-trip, for a frequency shift f_{AOM} = -10ν_{step} ~ -200 MHz and a filter bandwidth $\Delta\nu_{BPF}$ = 80 GHz. The letter C on the graphic indicates the convergence zone for the two initial conditions. Traces shown in Fig. 5.2 provides an image of the chirping behavior of the pulse as it evolves into a steady-state solution. For example, the solid blue line shows the evolution of a time-bandwidth limited $sech^2$ pulse with initial duration of τ_{FWHM} = 25 ps, while the red dashed line shows the evolution of a Gaussian-distribute noise source as initial condition.

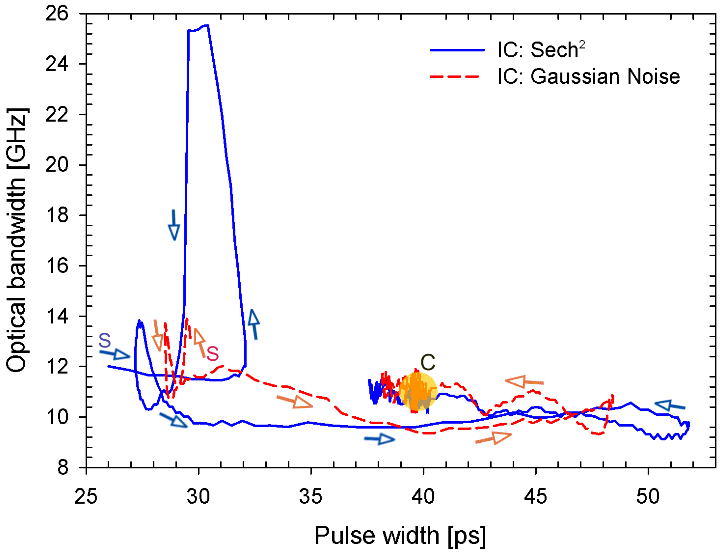

FIGURE 5.2: Numerical results of the spectral bandwidth as a function of the pulse width. Data is measured at each round-trip at the output of the 95:05 coupler (see Fig. 5.1). Two initial conditions are plotted: 1) Time-bandwidth limited $sech^2$ pulse (solid blue trace), and 2) Gaussian-distributed noise source (red dashed trace).

5.4.2 Pulse behavior for different cavity parameters

Numerical simulations were carried out to monitor the behavior of the pulse width and optical spectrum as a function of three different parameters of the laser cavity (frequency shift f_{AOM}, optical filter bandwidth $\Delta\nu_{BPF}$, and output coupling ratio P_{in}/P_{out}, where

P_{in} is the intracavity power and P_{out} the laser output power). Fig. 5.3(a) shows the results for the pulse width FWHM and optical bandwidth at 3 dB as functions of the filter bandwidth $\Delta\nu_{BPF}$ for different values of AOM frequency shifts f_{AOM}. These results are compared with the experimental data obtained in Chapter 4 (see the star symbols on the same figure). Numerical results obtained with the numerical model agree with the behaviour shown with perturbation theory and with former work [8, 101]. Furthermore, pulse shortening was also obtained for output coupling ratios close to 1. For example, for an optical filter bandwidth $\Delta\nu_{BPF}$ = 80 GHz, and frequency shift $f_{AOM} \sim$ -200 MHz, pulse widths of τ_{FWHM} = 40 ps and τ_{FWHM} = 37.5 ps were obtained for coupling ratios of P_{in}/P_{out} = 19, and P_{in}/P_{out} = 1, respectively (see Fig. 5.4). These results agree as well with the experimental results obtained in Chapter 4, see for example Fig. 4.11.

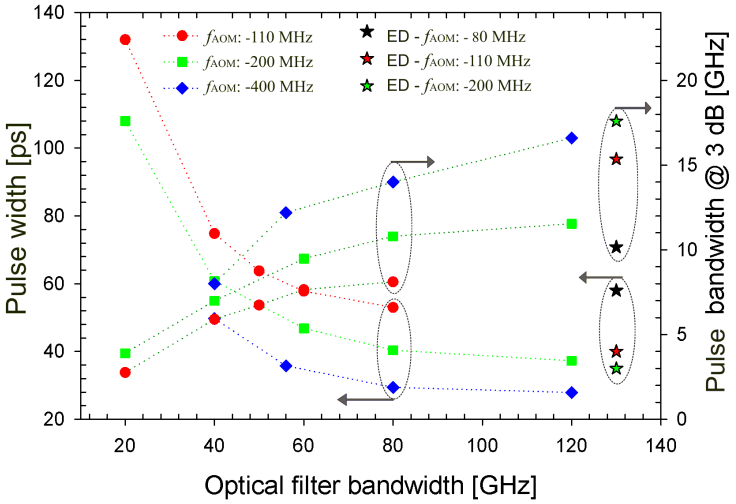

FIGURE 5.3: Numerical (circles) and experimental (stars) results of the pulse width τ_{FWHM} and pulse bandwidth $\Delta\lambda$ as functions of the optical filter bandwidth $\Delta\lambda_{BPF}$ for different frequency shifts f_{AOM}. ED stands for experimental data.

Pulse asymmetry and optical spectra were also monitored as functions of the frequency shift f_{AOM} and filter bandwidth $\Delta\nu_{BPF}$. Fig. 5.5 (a) and (b) show the "steady-state" solutions of the pulse spectrum and pulse trace in the time domain, for different filter bandwidths $\Delta\nu_{BPF}$ and a AOM frequency shift of f_{AOM} = -200 MHz, respectively. Numerical results showed an increment in the asymmetry of the optical spectrum and in the pulse shape for broader filter bandwidths. However, as it can be seen in Fig. 5.5, pulse asymmetry follows two trends for different filter bandwidth. The first one is observed for filter bandwidths below $\Delta\nu_{BPF} <$ 40 GHz. Here, the spectral maximum moves away from the filter central frequency ν_c and the pulse trace in the time domain shows a slightly steeper decay time on the trailing edge compared to the leading edge. See for example the solid black traces in Fig. 5.5 (a) and (b). For filter bandwidths above $\Delta\nu_{BPF} >$ 40 GHz, the tendency in the position of the pulse spectral maximum reverses. This change is largely generated by the development of a *hump* on the longer wavelength side of the spectrum, which pushes the spectral maximum to shorter wavelengths. In

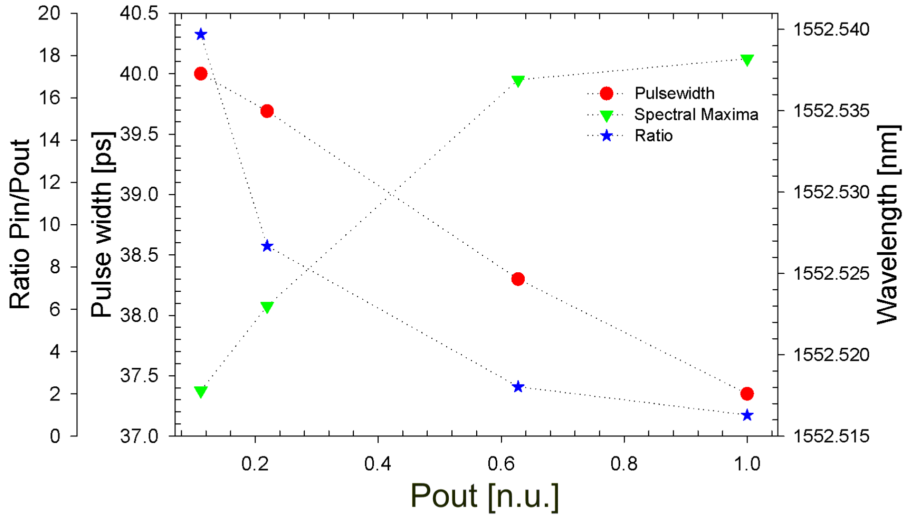

Figure 5.4: Pulse width (left axis), spectral maximum position (right axis), and power ratio between the intracavity power and the output power (offset left axis) as a function of the normalized output power.

the time domain, the *hump* formation is reflected on the longer decay time of the trailing edge of the pulse (see solid blue traces on Fig. 5.5 (a) and (b)). The numerical results for this operating regime agree well with the experimental data obtained in Chapter 4 for broad filter bandwidths.

The same performance regarding the position of the spectral maximum was observed in the numerical simulations of Sabert, et al., [8]. The authors explained this behavior in terms of the increasing contribution of SPM to the pulse spectrum. However in their work (and in any other work regarding ML-FSF lasers), there is no mention regarding the strong asymmetry observed on the pulse spectrum for broad filter bandwidths and its effect on the pulse shape. Therefore, in order to have a better understanding of the dynamics of the laser, the evolution of the optical spectrum and pulse intensity at each round-trip (RT) of the simulated laser cavity was tracked. For these calculations, a Gaussian-distributed white noise process as initial condition to simulate the spontaneous emission was used. Fig. 5.6 (a), and (c) show the intensity contour (in dB) of the pulse spectra at each round-trip for a filter bandwidth of $\Delta\nu_{BPF}$ = 20 GHz, and $\Delta\nu_{BPF}$ = 80 GHz, respectively, while Fig. 5.6 (b), and (d), show the evolution of the pulse intensity in normalized units for filter bandwidths, $\Delta\nu_{BPF}$ = 20 GHz, and $\Delta\nu_{BPF}$ = 80 GHz, respectively. Fig. 5.6 (a), and (c) show a rather systematic evolution of the optical spectrum that can be divided in two sections. The first one encompasses the shifting of most of the spectral density towards the longer wavelength side of the filter. This can be observed within the first round-trips RT $\leq$ 100 and RT $\leq$ 200 for Fig. 5.6 (a) and (c), respectively; while in the time domain, there is no evidence of pulse formation yet. A second section can be defined at the point where the spectral components reach a maximum deviation from the filter central wavelength and the optical spectrum becomes broad enough to pull the spectral maximum closer to the filter central wavelength. To

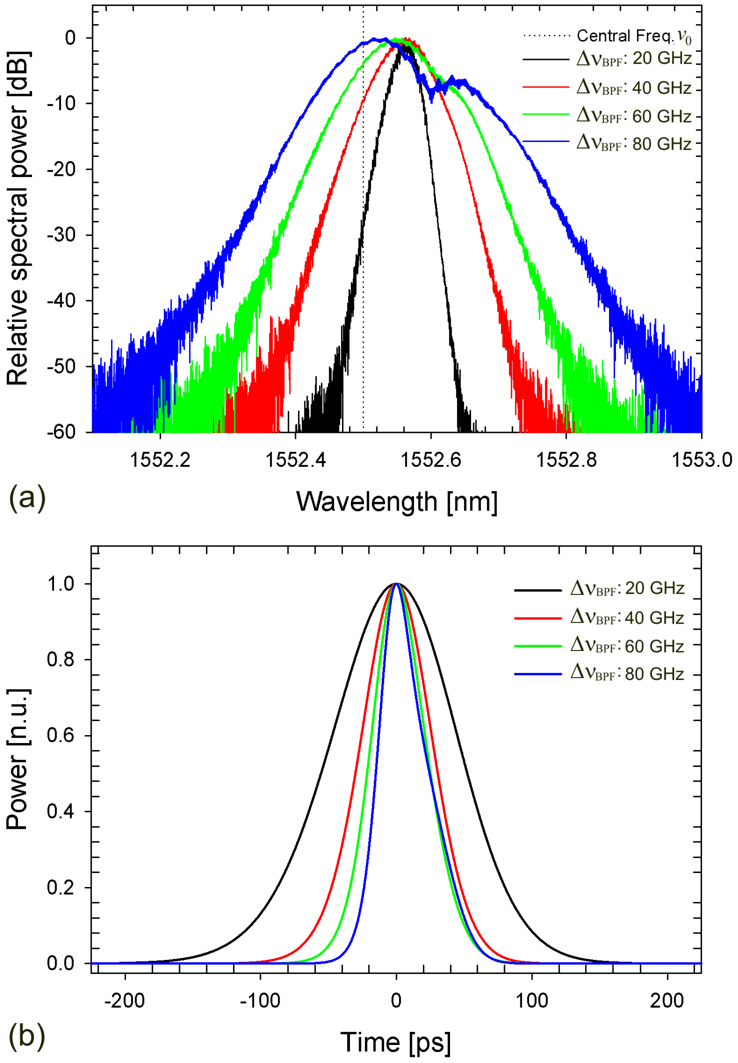

Figure 5.5: Steady state solutions of the (a) optical spectrum and (b) pulse shape, calculated for a frequency shift f_{AOM} = -200 MHz and different optical filter bandwidths $\Delta\nu_{BPF}$.

illustrate this, the filter central wavelength (λ_c = 1552.5 nm) is stressed with a dim black solid line on Fig. 5.6 (a), and (c). In this section the pulse formation starts to take place. In the case of the filter with $\Delta\nu_{BPF}$ = 80 GHz, a shorter pulse is formed with a higher peak power, allowing SPM to grow. This is reflected on the broad optical spectrum in Fig. 5.6 (c) between RT $\sim$ 250 and RT $\sim$ 350. As the peak power of the pulse increases at each round trip, a limit on its pulse energy is imposed by the cavity configuration. The pulse energy limit generates a split of the optical spectrum pushing most of the pulse spectral density towards shorter wavelengths, while a shoulder on the longer wavelength side of the spectrum starts developing (RT $\sim$ 400 for Fig. 5.6 (c)). In the time domain, the pulse starts to decrease its peak power, shedding part of its trailing edge energy to the surroundings (Fig. 5.6 (d)). Note, that this condition is not observed in the simulation with $\Delta\nu_{BPF}$ = 20 GHz, where the peak power of the pulse

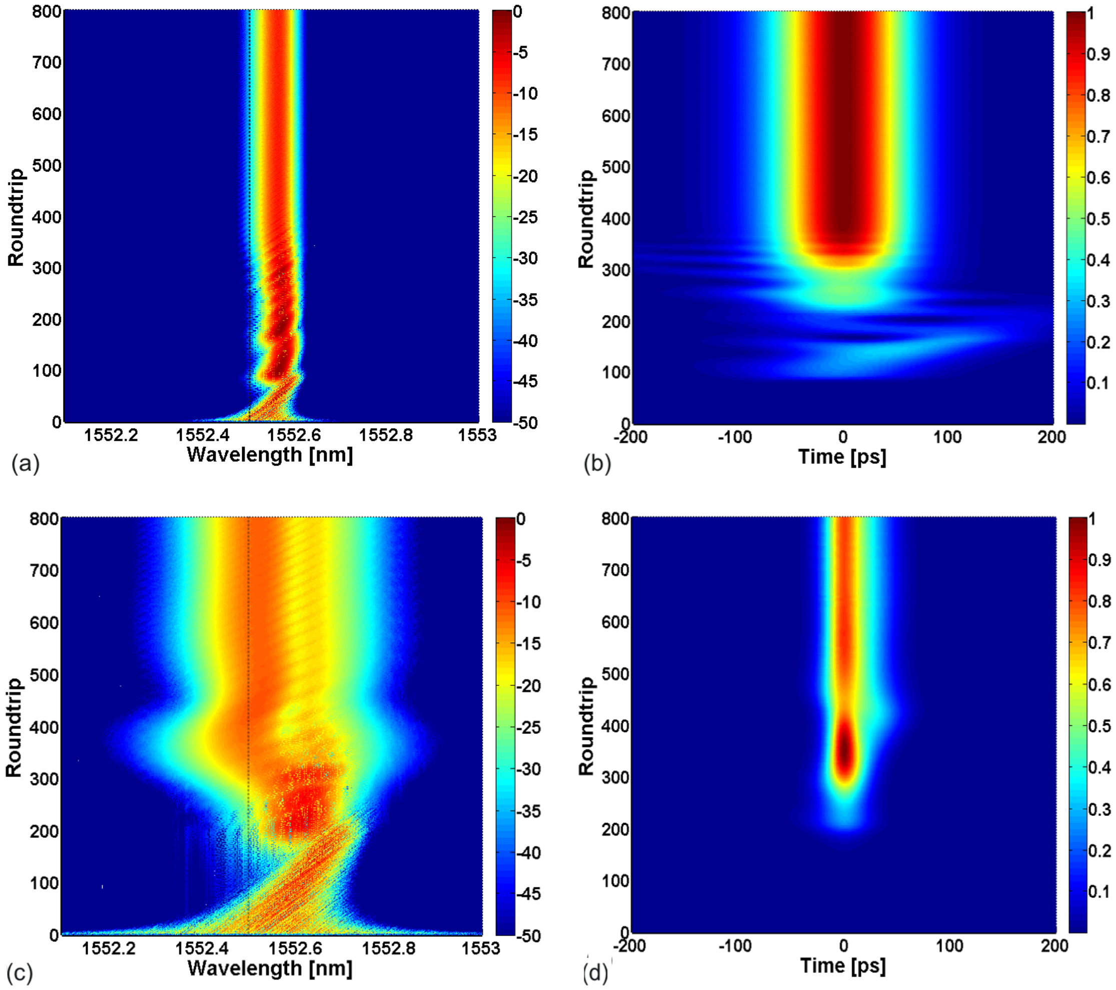

Figure 5.6: Evolution of the optical spectrum (left figures) and pulse (right figures) width for two different filter bandwidth $\Delta\nu_{BPF}$ = 20 GHz (upper figures) and $\Delta\nu_{BPF}$ = 80 GHz (bottom figures). The scale for the optical spectrum intensity is normalized in dBs to maximum at each roundtrip, while the intensity of the pulse in the time domain is normalized in a linear scale.

grows uniformly, until it reaches a steady state. Therefore, the pulling effect towards the central wavelength of the filter bandwidth is cause, in addition to the broadening of the spectrum, by the formation of the *hump* on the longer wavelength side of the pulse spectrum. In the time domain, the pulse shows a longer decay time on its trailing edge. This asymmetry is different from the one formed in the simulation for $\Delta\nu_{BPF} = 20$ GHz, where the steady-state pulse presents a slightly steeper trailing edge. The positions of the spectral maximum once the simulations reached a steady state were $\nu_{max} \sim 7.8$ GHz and $\nu_{max} \sim 4.2$ GHz, for Fig. 5.6 (a) and Fig. 5.6 (c), respectively.

Results of pulse asymmetry as a function of the AOM frequency shift parameter are shown in Fig. 5.7. Results show that pulse asymmetry is not only dependent on the optical bandwidth, but rather on the ratio between the optical filter bandwidth and the AOM frequency shift. Fig. 5.7 (a) shows the "steady-state" spectra for three different

AOM frequency shifts ($f_{AOM} = -110, -200, and - 400$ MHz) while keeping the optical filter bandwidth constant. A significant asymmetry is observed for $f_{AOM} = -110$ MHz, and it decreases as the AOM frequency shift increases. Results also show that in this case, the pulse spectral maximum locates further away from the filter central frequency ν_{ref} for larger frequency shift. The former results can be explained in terms of the pulse energy E_p obtained for each simulation. For the case of $f_{AOM} = -110$ MHz, the pulse energy is higher than in the other two cases $f_{AOM} = -200, and - 400$ MHz. This is due to the fact that the spectral maximum is located closer to ν_{ref}, and therefore the spectral components see more gain. This situation creates a pulse evolution similar to the one observed in Fig. 5.6 (c). However, as the pulse spectral maximum shifts away from the central part of the filter, the filter gain reduces and therefore the pulse gain. A decrease of pulse energy prevents the optical spectrum from breaking and forming a hump on the longer wavelength side. Therefore, reduction of pulse asymmetry will depend on the ratio between the optical filter bandwidth and the AOM frequency shift and the optical filter gain.

In [97], the asymmetry of the pulses is described in terms of pulse chirping as a consequence of the interaction between the nonlinearity of the medium, the frequency shift of the AOM, and the filter bandwidth. For example, if a constant downshifting frequency mechanism is applied to the optical spectrum, it is expected that the longer wavelength side of the spectrum is strongly filtered compared to the shorter wavelength side; in addition, SPM will contribute to increase or decrease the frequency shifting process of the signal. Therefore, according to [97], a pulse will show a steeper leading/trailing edge if the spectral components located in it are filtered more strongly than the opposite edge of the pulse. The numerical results obtained show that this description is correct as long as the SPM generated in the cavity is not predominant. Fig. 5.8(a) and (b) show the asymmetric intensities (solid lines) and phases (dashed lines) for two steady-state pulses simulated with a filter bandwidth of $\Delta\nu_{BPF} = 20$ GHz and $\Delta\nu_{BPF} = 80$ GHz, respectively. Fig. 5.8 (a) shows a steeper trailing edge and almost a linear phase across the pulse width, while in Fig. 5.8 (b) the steeper edge is formed on the leading edge of the pulse and the optical phase becomes non-linear. This increment in the non-linearity of the phase will be reflected in a stronger asymmetry of the pulse.

5.5 Conclusions

In this Chapter, I presented numerical simulation studies on the behavior of the optical spectrum and pulse shape as functions of different parameters of the laser cavity (frequency shift and optical bandwidth). The numerical model simulated an Er-doped FSF fiber laser in a ring cavity configuration including the following elements: gain medium, nonlinear element, bandpass filter and a frequency shifter. Results showed that for specific parameters of the laser cavity, stable pulses circulating at the fundamental rep-

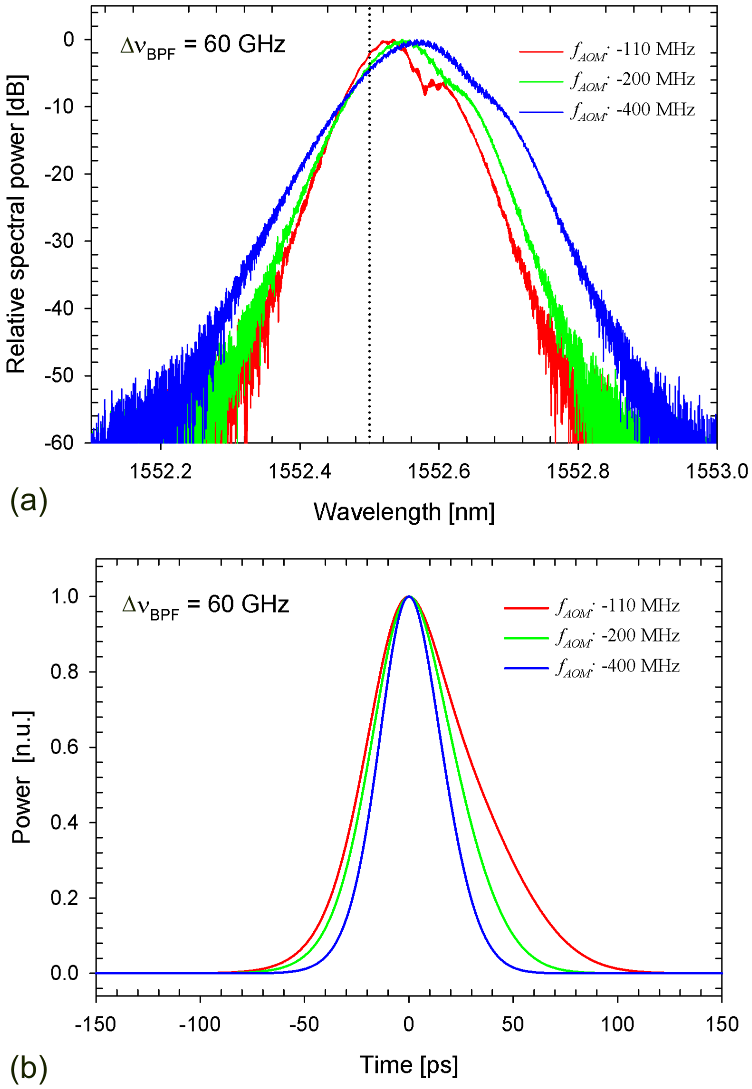

FIGURE 5.7: Steady state solutions of the (a) optical spectrum and (b) pulse shape, calculated for a optical filter bandwidth $\Delta\nu_{BPF} = 60$ GHz and different AOM frequency shifts: $f_{AOM} = -110$MHz (solid red line), $f_{AOM} = -200$MHz (solid gren line), and $f_{AOM} = -400$ MHz (solid blue line).

etition rate of the cavity could be formed. Numerical results shown in this Chapter are in agreement with previous work [8, 97, 101], where it was shown that shorter pulse widths are achieved either by increasing the bandwidth of the optical filter or increasing the frequency shift in the laser cavity. The novelty of the results shown in this Chapter compared to previous work is that the numerical model can properly simulate the output spectral shape of a FSF laser for a broad range of optical filter bandwidths and frequency shifts. Previous work had only focused on analyzing analytically [101] and numerically [8, 97] the pulse evolution in FSF lasers with narrow optical bandwidths and small frequency shifts where soliton perturbation theory can be used. That being said the results shown here offer a better graphical study of the pulse spectral evolution in a FSF laser, particularly for the relation between the filter bandwidth and frequency

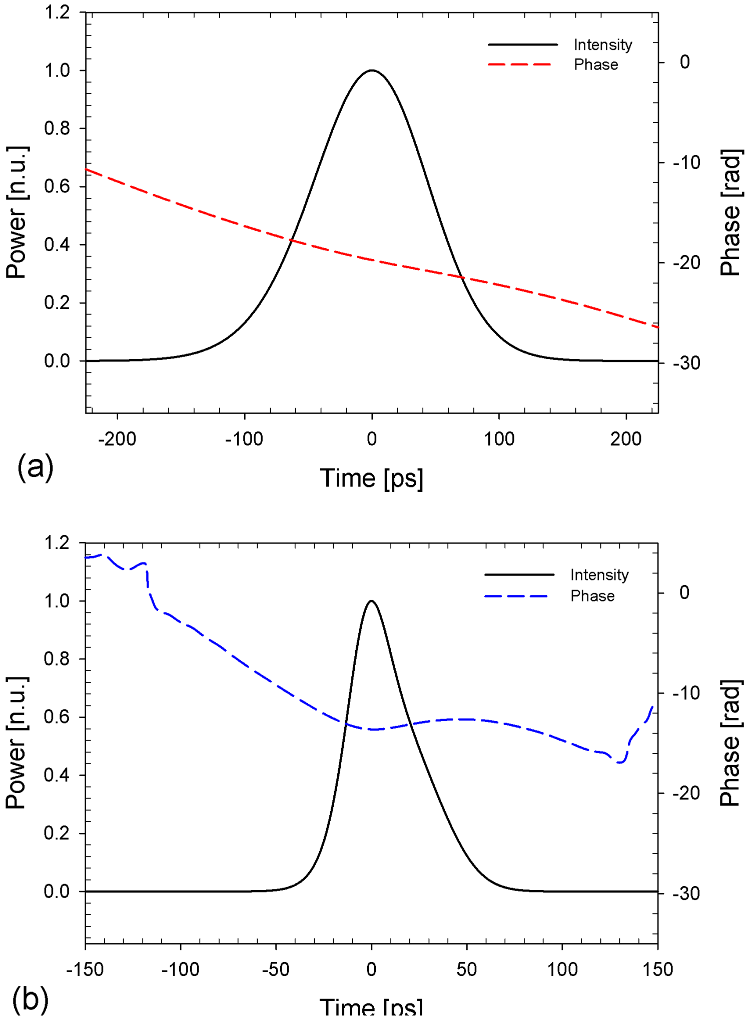

Figure 5.8: Intensity (solid line) and phase (dashed line) of steady state solutions for two filter bandwidths: (a) $\Delta\nu_{BPF} = 20$ GHz and (b) $\Delta\nu_{BPF} = 80$ GHz.

shift parameters. It is shown for the first time that as the ratio between the filter bandwidth and the frequency shift increases, the asymmetry of the pulse spectra also increases. The strong asymmetry is attributed to the increment in SPM leading to a split of the main pulse spectrum. This split is seen as a *hump* on the wavelength side of the spectrum where the pulse spectral components are being constantly shifted by the frequency shifter mechanism in the cavity. In the time domain, pulse asymmetry is strongly related to the *hump* formation on the pulse spectrum. For this particular case, these novel results show a clearer picture of the evolution of the optical spectrum from cw noise towards pulse formation in a FSF laser, allowing me to identify the reasons for the shifting of the spectral maximum of the pulse towards the opposite direction of the frequency shift mechanism. The numerical results shown in this Chapter, in addition to the experimental results shown in Chapter 4, can help to understand better a few of the complex interactions effects happening in these lasers that were not clarified in the literature so far.

Chapter 6

Mode-locked lasers based on a semiconductor saturable absorber mirror

In this Chapter I present the characterization of three mode-locked fibre lasers based on a semiconductor saturable absorber mirror (SESAM), operating at 1.5 μm. The simple, compact and stable design of the cavity allowed me, by simply changing the intracavity filter, to generate either femtosecond or wavelength-tunable picosecond pulses. Results obtained with these lasers are compared with the ones shown in Chapter 3 for a mode-locked FSF laser. The laser cavities presented in this chapter show a better performance in terms of self-start operation and reduction of amplitude and timing jitter noise compared to the FSF laser. Furthermore, the laser cavity proposed here show reliable self-starting continuous-wave (cw) mode-locking operation with no Q-switching instabilities [1]. The stability of the source allowed me to use it as a seed source for the master optical power amplifier (MOPA) system described in Chapter 7.

6.1 Introduction

Since their first mention in the literature in 1992 [110], SESAMs have become essential intracavity components for passive mode-locked (ML) lasers. One of the reasons for their commercial grow relies on the fact that their optical properties can be engineered over a broad range, thus allowing their use in wider cavity laser designs [57]. In particular, for fibre lasers, SESAMs offer several advantages such as, repeatability of self-starting ML,

---

[1] In a cw mode-locking laser, the resonator modes are excited with constant power. Therefore, pulses emitted in this operating regime have constant pulse energy. This is not the case for Q-switched mode-locking lasers where the intra-cavity pulse energy experiences strong fluctuations, related to a dynamic instability [44, 58]

enhancement in the stability for cw mode locking [58], and implementation in relative simple and compact cavity designs [50, 59–62].

Nowadays advances in semiconductor grow technology and bandgap engineering have extended the common GaAs-based technology used at 800 nm to wavelengths in the near infrared region [59, 111–113]. In particular, for wavelengths around 1.5 μm InP-based [59, 114], and GaAs-based diluted nitride [115, 116] SESAMs are commonly used; the latter ones presenting lower nonsaturable losses due to the lower lattice mismatch between the absorber (GaInNAs) and GaAs substrates.

Previous work in the 1.5 μm wavelength region has demonstrated compact and self-starting picosecond and femtosecond sources using various saturable absorbers, and cavity configurations. For example, in [59] self-starting transform-limited 320 fs pulses with 40 pJ energy were obtained in a linear cavity with an InGaAsP saturable absorber, while in [50], self-starting picosecond pulses with 2.3-nJ/pulse energy were generated by introducing a saturable absorber, and a linear loss element in the cavity to avoid multiple-pulse formation at high pump powers. As pointed out in Chapter 2, stretched-pulse ML fibre lasers are attractive configurations for superior pulse-energy extraction compared to soliton ML lasers. In these cavities, where pulse shaping by soliton formation in not presented, it is always desirable to carry out pulse shaping through a fast saturable absorber. Nevertheless, a fast saturable absorber presents problems for self-starting from a continuous-wave. In this case, slow saturable absorbers show better self-starting behaviour, with the inconvenience that pulses can develop a trailing wing due to their slow recovery response [117]. In [62] a stretched-pulse ML fibre laser was proposed combining a slow and a fast SESAM in the cavity. While the former provided a self-starting ML mechanism, the latter preserved the pulse shaping. Picosecond pulses with 250-pJ/pulse energy without multiple-pulse breakup at high pump powers were generated with this configuration. SESAMs have also been used for pulse shaping in fibre lasers with fundamental repetition rates above 2 GHz [118]. In this work, the high gain per unit length was provided by a 4.8-cm piece of commercial co-doped $\mathrm{Er}^{3+}/\mathrm{Yb}^{3+}$ fibre pumped with a semiconductor laser at 975 nm. Short pulses and reliable self-starting cw ML was achieved by means of a commercial saturable absorber mirror with a resonant design and relatively high modulation depth.

In this chapter, a sigma cavity laser including a polarization beam splitter, to enhance NLPE, and a commercial SESAM is proposed and characterized. The laser cavity was later on modified in order to study the pulse duration limits and to achieve a robust self-start operation and low noise laser. The similarity in the design of this laser with the FSF laser, described in Section 4.3.2, allowed me to compare the overall performance (e.g. self-starting operation, stability, amplitude and timing jitter) of both lasers.

6.2 SESAM characteristics

In Section 6.1 it was mentioned that SESAM parameters can be selected depending on a particular laser configuration. Therefore, choosing the correct SESAM design is foremost to achieve a good laser performance and to avoid Q-switching instabilities (the latter being a common issue for long upper-state lifetime lasers) [58]. Usually, when soliton-pulse shaping is not present in the laser cavity (i.e. stretched-pulse laser cavities), a SESAM with high modulation depth ΔR is desirable to enhance the mechanism of pulse narrowing and to provide enough perturbation for self-starting ML behaviour. Yet, a high modulation depth leads to an increment of the non-saturable losses A_{ns} which eventually can lead to Q-switching instabilities [117]. Therefore, a SESAM with low modulation depth is also desirable to suppress Q-switching behaviour and enhance cw ML stability.

In addition to the correct selection of SESAM parameters for a good laser performance, different groups have carried out investigations to determine a stability criterion against Q-switching behaviour in passively ML lasers [117, 119]. According to Hönninger et al. [119], if the absorber recovery time is much shorter than the cavity round-trip time, then the minimum intracavity pulse energy to achieve stable cw ML is given by [119]:

$$E_{P,c} = \left[F_{sat,L}\, A_{eff,L}\, F_{sat,A}\, A_{eff,A}\, \Delta R\right]^{1/2} \tag{6.1}$$

Where $F_{sat,L} = h\nu / \left[2\left(\sigma_{em} + \sigma_{abs}\right)\right]$ is the gain saturation fluence, $h\nu$ is the lasing photon energy, σ_{em} and σ_{abs} are the emission and absorption cross-section of the lasing wavelength, $F_{sat,A}$ is the SESAM saturation fluence, $A_{eff,L}$ and $A_{eff,A}$ are the effective laser mode areas of the gain medium and on the SESAM, respectively.

From Eq. 6.1 it can be seen that the effective laser mode area on the SESAM is proportional to the critical intracavity pulse energy, therefore, a way to improve the stability of cw ML can be done by adjusting the effective laser mode area on the SESAM. Taking into account the above information, it was decided to buy a SESAM from BATOP Optoelectronics [120] with a resonant design, average modulation depth $\Delta R = 14\%$ and a relaxation time constant $\tau_{sam} = 2$ ps. A summary of the characteristics of the SESAM is shown in Table 6.1, and the graphics for the spectral reflectance, dispersion, and saturation fluence are shown in Appendix B. The SESAM was centre mounted on a gold plated cylinder and fixed to a translation stage. This mounted scheme allowed me

TABLE 6.1: Semiconductor saturable absorber mirror specifications

SAM-1550-23-24.5g-2ps

Laser wavelength	λ = 1550 nm
High reflection band	λ = 1550 - 1600 nm
Absorbance	A_o = 23 %
Modulation depth	ΔR = 14 %
Non-saturable loss	A_{ns} = 9 %
Saturation fluence	F_{sat} = 25 μJ/cm^2
Relaxation time constant	$\tau_{sam} \sim$ 2 ps
Damage thershold	500 MW/cm^2

to adjust the laser effective mode area on the SESAM (e.g. to adjust the pulse energy incident on the semiconductor).

6.3 Experimental Results

The proposed configuration for the ML laser with a SESAM is similar to the one proposed in Chapter 4 for the FSF laser. However, in this case, a sigma configuration had to be implemented in order to use the reflected signal from the saturable absorber. It was found that the output of the laser had a tendency to lase in Q-switching ML regime or in a noisy harmonic ML regime when the SESAM was placed close to the gain fibre (i.e. before the polarization beam splitter). These operating regimes were observed for different pump powers and combinations of lenses used to adjust the effective laser mode area on the SESAM. The cavity in Fig. 6.1 (a) showed the most stable configuration for a self-starting cw ML signal. The position of the SESAM for the configurations involving optical filters (i.e. the position of the SESAM before or after the optical filter) did not make a difference in the laser performance. Therefore, in order to have a better comparison with the FSF laser configuration described in Chapter 4, it was decided to place the SESAM before the optical filters, as shown in Fig. 6.1 (b) and (c). In this configuration, the self-starting behaviour was carried out by the SESAM while the NLPE acted as an additional pulse shaper.

The setup for the femtosecond ML laser is shown in Fig. 6.1 (a). The laser cavity consists of the same optical devices described in Section 4.3.2. However, for this configuration, a 3 port circulator was spliced into the cavity after the 95:5% coupler. The fibre end of port 2 of the circulator was angle cleaved and the light coming out of this port was launched onto the SESAM (described in Section 6.2), through a pair of aspheric lenses. The pair of aspheric lenses helped to adjust the incident pulse fluence by varying the illuminated area on the SESAM. I found that the laser presented a better performance by focusing the light beam more tightly onto the saturable absorber. This action was achieved by combining a lens of effective focal length EFL = 18.40 mm (Thorlabs C280 TME-C) closer to the fibre and a lens of EFL = 15.29 mm (Thorlabs C260 TME-C) closer to the SESAM. Finally, to close the cavity, the port 3 of the circulator was spliced to the signal port of the 1480/1550 WDM. The total cavity length was ∼ 11 m, and had an average GVD parameter β_2 = -0.2 ps^2.

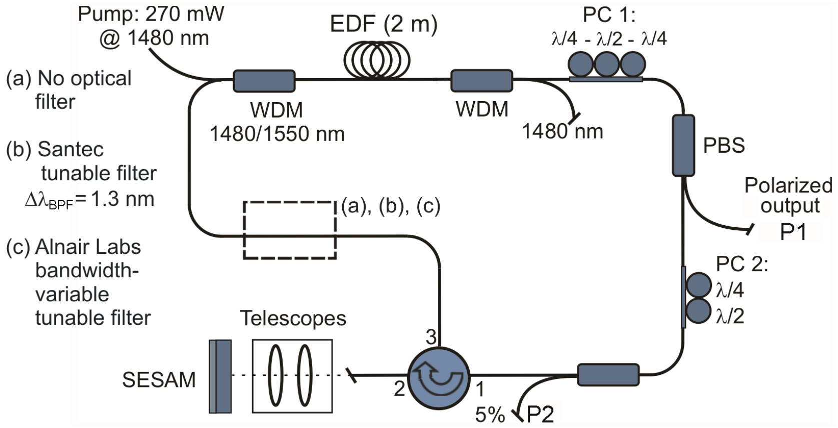

Figure 6.1: Schematic of the mode-locked fibre sigma laser with a semiconductor saturable absorber. The configuration was tested without an (a) optical filter, with a (b) tunable filter with $\Delta\lambda_{BPF}$ = 1.3 nm and (c) bandwidth-variable tunable filter. EDF, Er-doped fiber; PC, polarization controller; PBS, polarization beam splitter; P1, port 1; P2, port 2.

6.3.1 Femtosecond laser performance

The laser was characterized in the time domain with a background-free (noncollinear) second harmonic generation autocorrelator, and in the frequency domain by an optical and RF spectrum analyzer. The laser presented stable self-starting fundamental ML behaviour for pump powers as low as P_{pump} ∼ 37 mW. ML operation remained stable in the cavity up to P_{pump} ∼ 48 mW. Above this power level, the laser output presented noisy multiple-pulse behaviour, which is characteristic of soliton systems with excessive gain [121]. For P_{pump} ∼ 43 mW, the output signal monitored at P1 generated femtosecond pulses with 105-pJ pulse energy and average output power P_{out} = 1.9 mW. Fig. 6.2 (a) and (b) show the measured output pulse autocorrelation and pulse spectrum from P1 and P2, respectively. The measured pulse width at FWHM from P1 was ∼ 310 fs (assuming a $sech^2$ profile), while the 3 dB spectral bandwidth was ∼ 9.72 nm centred at 1556 nm. The corresponding time-bandwidth product (TBP) was calculated to be ∼ 0.372. The peak power P_{peak} calculated with the 310 fs pulse was ∼ 298 W. Formation of Kelly sidebands on the optical spectrum are related to the soliton-like nature of the pulses generated in the laser cavity [122]. Fig. 6.2 (c) shows the RF spectrum at the cavity fundamental frequency (18.3 MHz) with a span of 1 MHz and a resolution bandwidth of 100 kHz. The low broad band noise observed on the RF spectrum highlights the low amplitude fluctuations ($\Delta E/E \sim 0.091\%$) of the laser cavity. Appendix A explains the method for characterizing the laser noise.

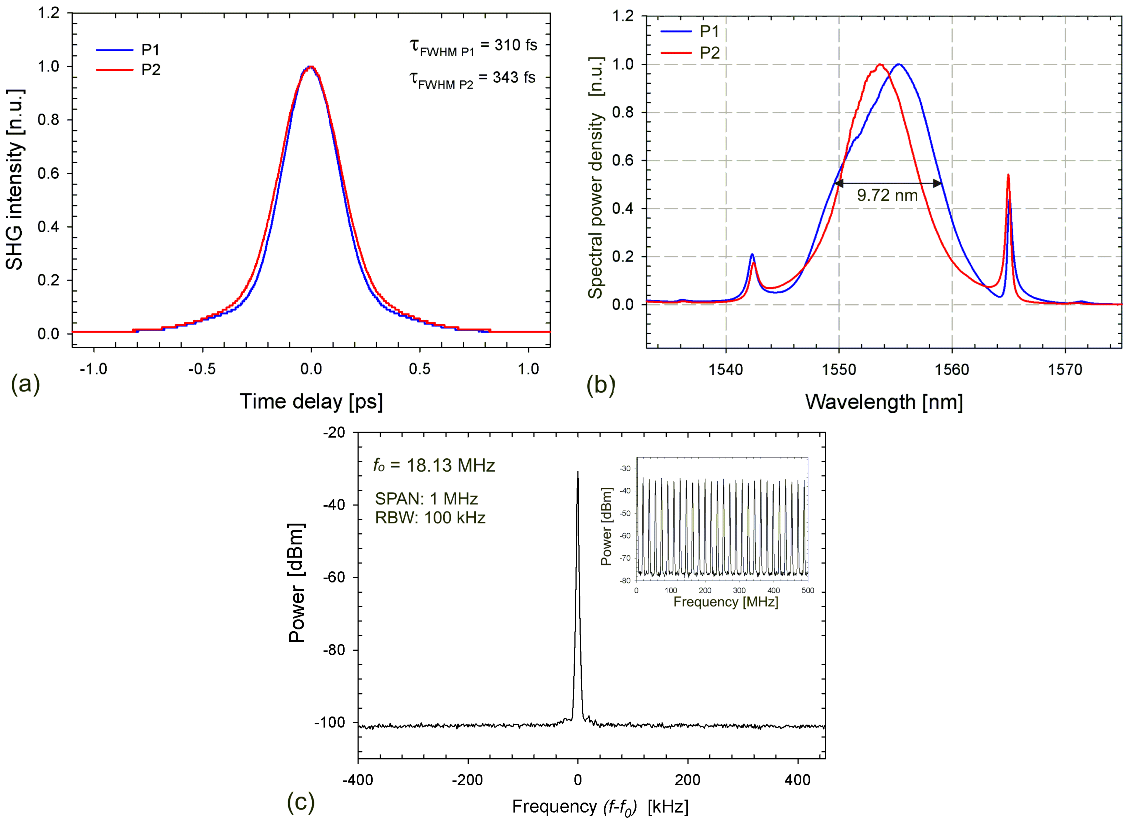

FIGURE 6.2: (a) Autocorrelation measurement of port P1, (b) optical spectra of port P1 and port P2, and (c) RF spectrum of the output signal in port P1, for a cavity with net GVD parameter β_2 = - 0.19 ps^2.

In soliton ML lasers pulse duration can be controlled by adjusting the dispersion in the cavity. This condition is given by the soliton area theorem which relates the product of the pulse width and its energy to the average GVD dispersion and nonlinearity of the cavity (see Section 3.2.1) [121]. Considering this, the laser cavity was further characterized as a function of the cavity dispersion β_2 by reducing the length of the single mode fibre (SMF-28) in the cavity. Fig. 6.3 (a) shows the pulse width (circles) and TBPs (triangles) as a function of the cavity dispersion. Pulse widths of $\sim$ 244 fs (assuming a $sech^2$ pulse shape) with TBP $\sim$ 0.526 were obtained for a β_2 = -0.0799 ps^2. Further reduction of the cavity dispersion was limited by the amount of fibre used in the two manual polarization controllers and the length of fibre ($\sim$ 10 cm) required to splice the different cavity components. Fig. 6.3 (b) shows the measured pulse spectrum at port P1 (blue trace) and port P2 (red trace) for a cavity dispersion β_2 = -0.0799 ps^2. Experimental results show a shortening in the pulse width and an increment in the TBP of the pulses as β_2 is reduced in the cavity. Reduction of the anomalous dispersion in the cavity is reflected in the dynamics of the pulse circulating in the cavity, where the spectral shapes between port P1 and port P2 become less similar. See for comparison Fig. 6.2 (b) and Fig. 6.3 (b). Spectral side bands (Kelly bands) amplitudes were weakened substantially for $\beta_2 \leq$ -0.1.

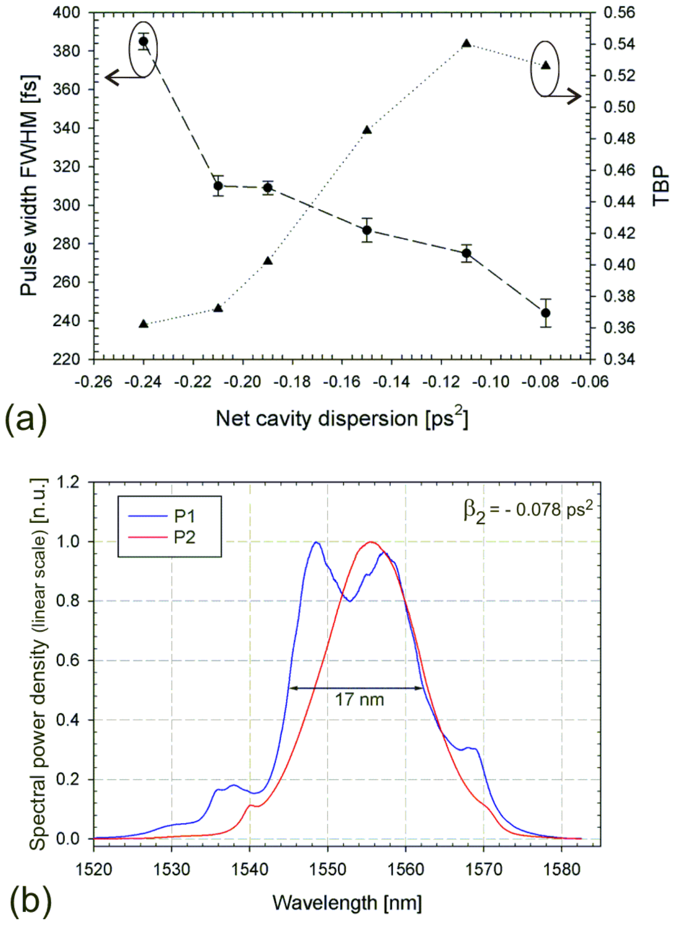

FIGURE 6.3: (a) Pulse width measured at FWHM and TBPs as a function of the average cavity dispersion $\beta 2$. (b) pulse spectrum from port P1 (blue trace) and P2 (red trace) for a β_2 = -0.078.

6.3.2 Wavelength-tunable picosecond fibre laser

Tunability of the laser source was achieved by insertion of a bandpass filter with 1.3 nm bandwidth measured at FWHM. The tuning range of the fibre laser was limited by the fiberized filter to ∼ 30 nm. Self-starting fundamental ML behaviour was achieved for pump powers as low as $P_{pump} \sim$ 23 mW. The robust stability of the laser allowed it to remain ML through the whole tuning range of the filter. Addition of the filter in the cavity broadened the pulse width to ∼ 11 ps. Pulse width adjustment was also possible by slightly tuning the position of the polarization controllers PC1 and PC2 in the cavity. For this experiment, pulse width measurements were carried out with a commercial frequency resolved optical gating (FROG) system from Southern Photonics (model: HR150 Optical Pulse Analyser). The temporal and optical resolution of the system is 26.66 fs, and $\leq$ 0.05 nm, respectively. Fig. 6.4 (a) shows the recovered spectrogram of the laser signal at 1552 nm for a specific polarization state (PS1) in the cavity. The polarization states PS1 and PS2, shown in Fig. 6.4, define the shortest and broadest stable pulses achieved, respectively. Further adjustment of the polarization controllers beyond these points led to an unstable signal. Fig. 6.4 (b) shows the retrieved intensity (solid line) and phase (dashed line) as a function of time, for the polarization states PS1 and PS2, while Fig. 6.4 (c) shows the retrieved pulse spectra for the same polarization states. For PS1 the calculated pulse width and optical bandwidth was $\sim$ 9.46 ps and $\sim$ 0.47 nm, respectively; while for PS2 the same parameters were $\sim$ 11.55 ps, and $\sim$ 0.35 nm. Retrieval of the pulse phase showed that both pulses are linearly up-chirped (i.e. the leading edge of the pulse is red-shifted while the trailing edge is blue-shifted), with calculated TBPs of 0.56 and 0.50, for PS1 and PS2, respectively.

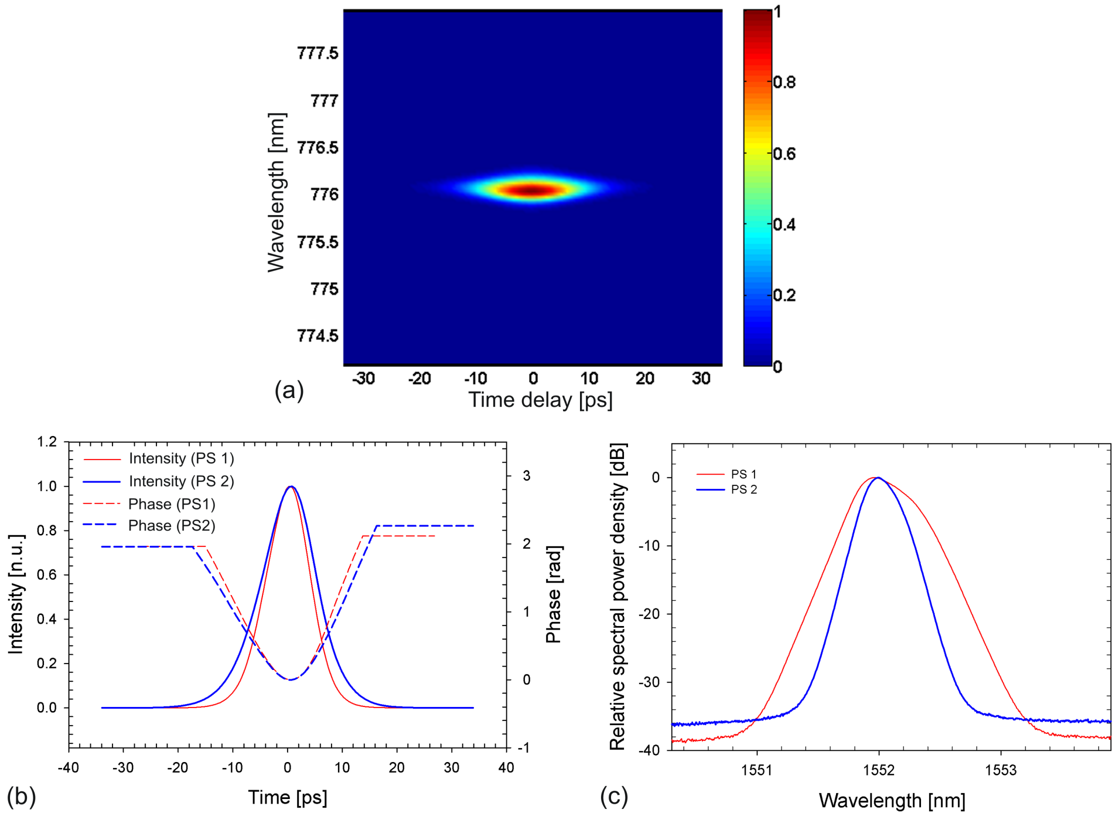

FIGURE 6.4: (a) Measured FROG trace of the polarization state PS1. Retrieved intensity (solid) and phase (dashed) as a function of time for two polarization states in the cavity: PS1 (red) and PS2 (blue). (c) Retrieved spectrum for PS1 (red) and PS2 (blue).

Figure 6.5 (a) shows the pulse width measurements over the entire tuning range of the laser (1535 - 1565 nm). The scatter data on Fig. 6.5 (a) represents the average pulse width, while the "error bars" show the minimum and maximum pulse width obtained by adjusting the polarization state in the cavity. The laser emitted pulse trains with an average pulse width of $\sim$ 11 ps over most of the tuning range, with a slight increment in the pulse duration for wavelengths shorter than 1538 nm.

As mentioned above, self-starting fundamental ML behaviour was achieved for pump power thresholds as low as 23 mW for wavelengths longer than 1553 nm. However, for shorter wavelengths this threshold increased to ∼ 30 mW. Fig. 6.5 (b) shows the measured average output power and calculated peak power over the entire tuning range of the laser. Inclusion of the optical filter reduced the average output power to ∼ 1 mW for wavelengths shorter than 1553 nm. For longer wavelengths ($\lambda_0 \geq 1553$ nm), the pump power in the cavity was decreased in order to sustain a stable cw ML signal. Reduction of pump power and adjustments of the position of the polarization controllers decreased the average output power to ∼ 0.4 mW. The calculated peak power changed from 5.5 W at 1530 nm to 8.6 W at 1550 nm. For longer wavelengths, it decreased to ∼ 2.5 W.

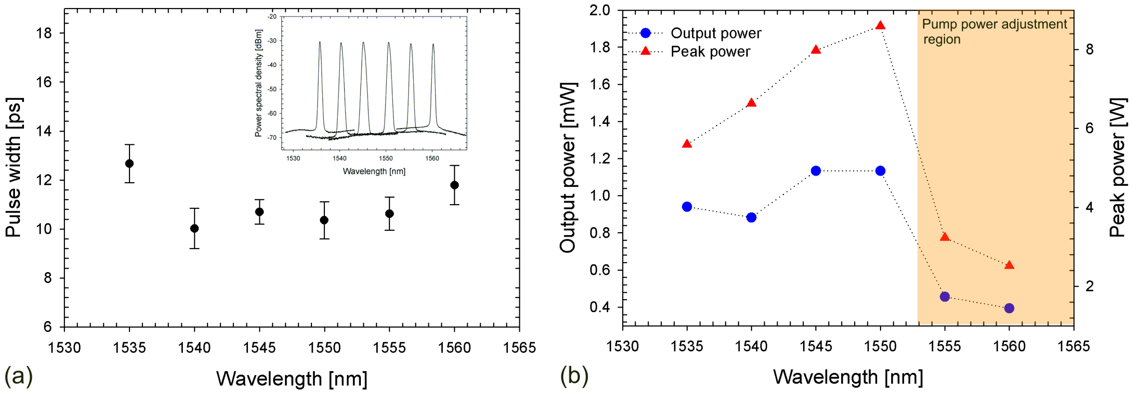

Figure 6.5: (a) Pulse width measurements along the entire tuning range of the optical filter. Inset shows the optical spectra of the laser plotted over the same tuning range. (b) Output power (circles) and peak power (triangles) as a function of wavelength. The coloured zone represents the wavelength region where the pump power is adjusted in order to keep ML in the laser.

The laser was further characterized by measuring the amplitude noise and timing jitter with the Von der Linde method [9] described in Appendix A. Fig. 6.6 (a) and (b) show the broadband and narrowband RF spectrum of the ML laser centred at the cavity round-trip frequency (13.28 MHz), respectively. The calculated amplitude fluctuations of the laser was small ($\Delta E/E \sim 0.47$ %). Therefore, it was possible to ignore it for estimating the time jitter [9]. The calculated contribution of time jitter of the pulses was ∼ 6.09 ps, measured at the 10^{th} harmonic narrow band spectrum of the RF signal (see inset of Fig. 6.6 (a)).

6.3.3 Wavelength- and bandwidth-tunable picosecond fibre laser

To test whether the laser cavity had the same performance for a different type of filter, I replaced the 1.3 nm bandwidth filter for a wavelength- and bandwidth-tunable filter

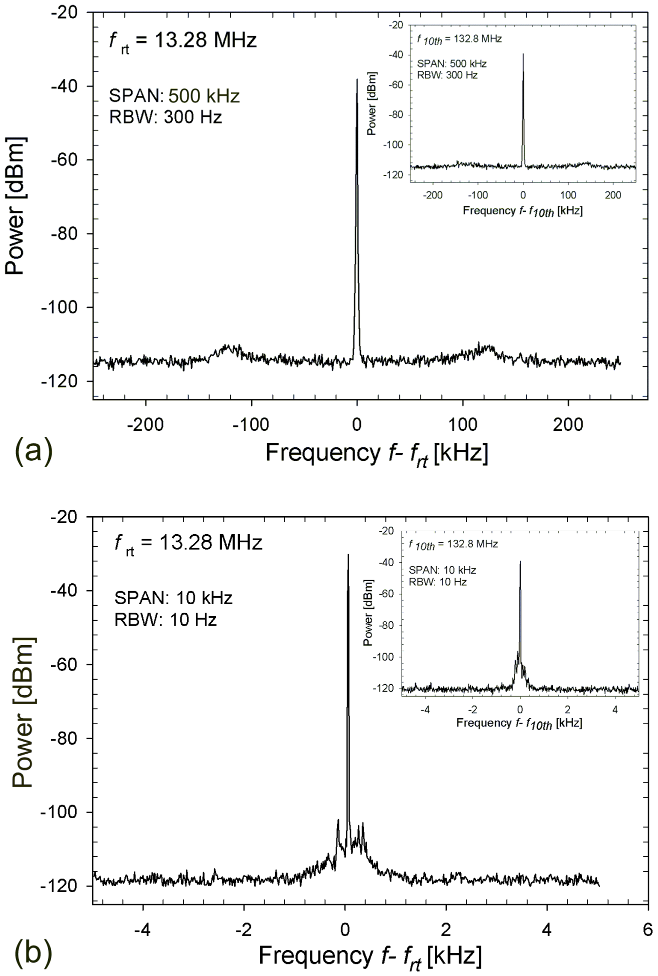

FIGURE 6.6: (a) RF spectrum of the picosecond fibre laser centered at the cavity round trip frequency. (b) High-resolution version of (a), showing the low amplitude noise of the laser. Insets show the same information described in (a) and (b), but for for the tenth harmonic, respectively. The information in the tenth harmonic is used to calculate the timing jitter.

from Alnair Labs (see Fig. 6.1(c)). The laser has a tuning range of 80 nm (1530 nm - 1610 nm) and a tuning bandwidth at 3 dB from 0.1 nm to 13 nm with filter-edge roll-off (~ 200 dB/nm). The laser was firstly characterized by tuning the filter bandwidth (7 nm $\geq \Delta\lambda_{BPF} \leq$ 1.3 nm) while keeping the filter wavelength fixed at 1550 nm. Starting from the broadest bandwidth ($\Delta\lambda_{BPF}$ = 7 nm), the laser showed stable self-starting fundamental ML operation (f_{rt} = 12.87 MHz) at 30 mW of pump power and it remained locked as the bandwidth of the filter was narrowed. Fig. 6.7 (a) and (b) shows the recovered spectrogram (upper figures) and the retrieved pulse intensity and phase (lower figures) for a filter bandwidth ($\Delta\lambda_{BPF}$ = 7 nm) and ($\Delta\lambda_{BPF}$ = 1.3 nm), respectively. For $\Delta\lambda_{BPF}$ = 7 nm the calculated pulses duration was ~ 2.76 ps with a TBP ~ 0.64, while for $\Delta\lambda_{BPF}$ = 1.3 nm the calculated pulse duration was ~ 11.3 ps with a TBP ~ 0.62. The sinc shaped pulses observed on the retrival pulse intensity are believed to be formed by the band limited rectangular spectrum of the optical filter.

Finally, retrieval of the pulse phase showed that the pulses were also linearly-up chirped.

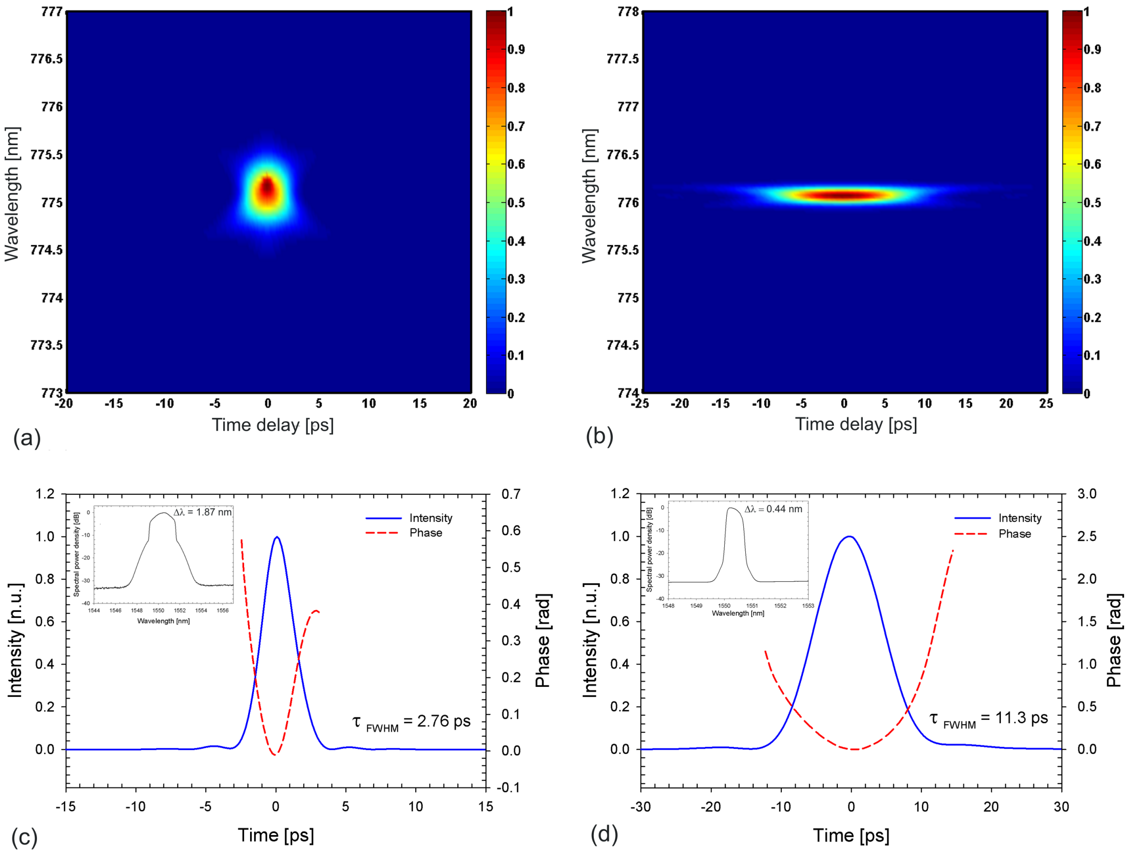

FIGURE 6.7: Measured FROG trace (UPPER figures) and retrieved intensity (solid) and phase (dashed) as a function of time (LOWER figures) for an optical filter bandwidth (a) and (c) $\Delta\lambda_{BPF}$ = 7 nm, and (b) and (d) $\Delta\lambda_{BPF}$ = 1.3 nm. INSETS: Optical spectrum of the measured pulse.

A summary of the average output power (triangles) and peak power (circles) measured at different lasing wavelengths and bandwidths are shown in Fig. 6.8 (a) and (b), respectively. In general, average output powers of ∼ 0.4 mW were measured for different filter bandwidths and through the entire tuning range of the fibre laser. The calculated peak powers for different filter bandwidths yielded values from 11.5 W for $\Delta\lambda_{BPF}$ = 7 nm to 2.3 W for $\Delta\lambda_{BPF}$ = 1.3 nm. It is worth mentioning that shorter pulses with durations of ∼ 1.3 ps were also achieved for the maximum filter bandwidth ($\Delta\lambda_{BPF}$ = 13 nm). However, for this filter bandwidth continuous wavelength tuning was not possible.

Table 6.2 shows a summary with the specifications of each source described in this Chapter. For comparison purposes, the table also shows the specifications of the FSF laser (@ 110 MHz) described in Chapter 4.

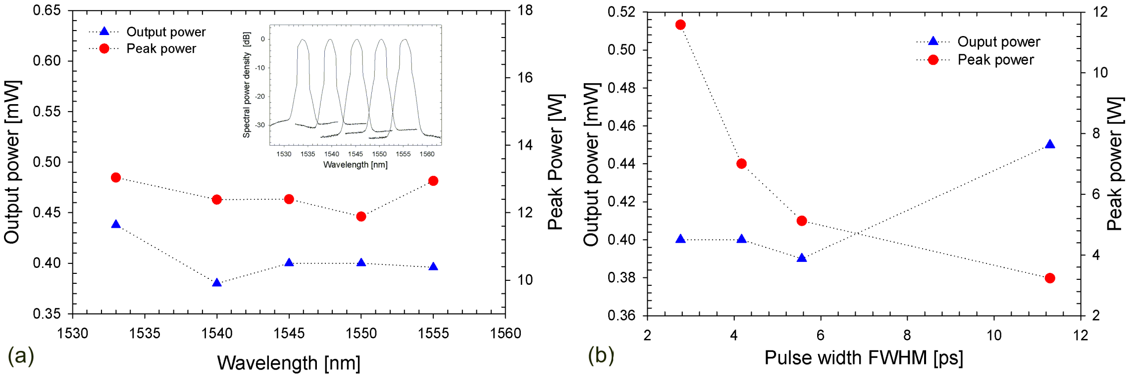

FIGURE 6.8: (a) Output power (triangles) and peak power (circles) measurements along the entire tuning range of the optical filter with filter bandwidth $\Delta\lambda_{BPF} = 7$ nm. Inset shows the optical spectra of the laser plotted over the same tuning range. (b) Output power (triangles) and peak power (circles) as a function of pulse width.

6.4 Conclusions

In conclusion, I presented three compact and stable ML Er^{3+}-doped fibre laser operating in the 1.5 μm region. Self-starting ML behaviour in all three cavities is achieved by enhancing NLPE and by incorporation of a commercial SESAM. The proposed sigma cavity configuration works in a fundamental ML regime with and without optical filter for pump powers as low as $\leq$ 23 mW. The laser can deliver (without an optical filter) femtosecond pulses ($\leq$ 380 ps) with a maximum average output power of $\sim$ 1.9 mW, at repetition rates of $\sim$ 13 MHz ($E_p \sim$ 105 pJ). Incorporation of an optical filter in the cavity, allows for picosecond pulse ($\leq$ 12 ps) generation with maximum average powers of $P_{pump} \sim$ 1 mW, at repetition rates of $\sim$ 13 MHz, corresponding to pulse energies $\leq$ 102 pJ. The robust ML stability of the laser cavity allows a continuous wavelength (1533 nm to 1558 nm) and bandwidth (7 nm to 1.3 nm) tuning, making the laser a versatile tool for different applications (seeding of Erbium amplifiers or highly non-linear fibres, second harmonic generation, medical applications, etc).

Comparison between the lasers presented in this Chapter and the FSF laser described in Chapter 4 shows a better performance in terms of noise (e.g. see table 6.2), and stability for the former ones. ML lasers with SESAM showed to be more resilient to environmental fluctuations (e.g. vibrations or changes in temperature), although both kind of laser could remain ML for hours. Another advantage observed with the lasers using SESAM is the lack of hysteresis presented in FSF lasers to achieve self-starting fundamental ML behaviour (i.e. there is no need to pump at high powers to start the ML mechanism in the cavity).

Table 6.2: Laser parameters for different configurations of cw ML fibre lasers. *Power scaling of FSFL forms new pulses with the same characteristics of the fundamental pulse. These new pulses travel in compact groups close to each other at the fundamental round-trip frequency.

Laser configuration	**Pulse width (ps)**	**Wavelength (nm)**	**PRR (MHz)**	P_{out} **(mW)**	**Pulse energy (pJ)**	**Amplitude noise** $\Delta E/E$	**Time jitter** $\Delta\tau/T_{rt}$	**Power Scaling**
SESAM **Femtosecond**	244 - 386 fs	1556 nm	13 MHz	1.9 mW	105 pJ	$\sim$ 0.091 %	——	NO
SESAM **Alnair filter**	2.7 - 11.3 ps	1535 - 1558 nm	12.87 MHz	0.4 mW	$\sim$ 40 pJ	——	——	NO
SESAM **Santec filter**	$\sim$ 10.5 ps	1535 - 1560 nm	13.28 MHz	0.4 - 1 mW	40 - 102 pJ	$\sim$ 0.47 %	$\sim$ 6.09 ps	NO
FSFL (110 MHz) **Santec filter**	$\sim$ 39 ps	1533 -1565 nm	13.7 MHz	$\sim$ 1 mW	72 pJ	$\sim$1.33 %	$\sim$ 20 ps	YES *

Chapter 7

Amplification of a picosecond bandwidth-tunable laser source

In this Chapter I describe the implementation and characterization of two master oscillator power amplifiers MOPAs used in the direct amplification of the 10 picosecond bandwidth-tunable laser source described in Section 6.3.2. Two large mode area (LMA) fibres were tested for the high power amplifier stage and their performance was compared in terms of efficiency and beam quality. The first tested fibre was an in-house fabricated double-cladding Er^{3+}/Yb^{3+} co-doped LMA fibre (LF122) with core diameter of 27 μm, while the second one was a commercial double-cladding Er^{3+}-doped LMA fibre (Er-HPA) with core diameter of 35 μm. The maximum extracted average and peak power for each fibre was 1.01 W and 5.7 kW for the LF122 fibre, and 1.5 W and 11 kW for the Er-HPA fibre at a wavelength of 1535 nm and 1558 nm, respectively. In this chapter I proposed in order to compensate for the low cladding absorption at 980 nm of the Er-HPA a hybrid configuration where a high power commercial Raman laser is used to core-pumped the amplifier in a co-propagating scheme and a 980 nm laser diode in cladding-pumped in counter-propagation. The results show that the Er^{3+} fibre managed to handle higher average powers while keeping a good pulse shape.

7.1 Introduction

Mode-locked (ML) fibre lasers are feasible compact light sources that can emit pulses in the femtosecond and picosecond regime. However due to high nonlinearities experienced in the oscillator, pulse peak powers and pulse energies are limited to $\sim$ 1 kW [42] and $\sim$ 1 nJ [2], respectively. Yet, some applications such as material processing, frequency conversion, supercontinuum generation, or spectroscopy require higher peak powers or pulse energies. Therefore, pulses from these oscillators must be amplified. Fibre amplifiers have demonstrated great potential in power scalability reaching average powers in the kW regime and peak powers in the GW regime for cw [10, 27, 28] and pulse mode operation [123–125], respectively. In addition, the geometry of the active waveguide offers on the one hand good heat-dissipation, high single pass gain, high beam quality, and compactness [2]. However, on the other hand it also brings unwanted nonlinear effects such as SPM, stimulated Raman scattering (SRS) and/or stimulated Brillouin scattering (SBS). In particular, for ultrashort pulse amplification, SPM imposes most of the limitations for pulse amplification. As explained in Chapter 2, SPM gives rise to an intensity-dependent phase shift that leads to spectral broadening of the pulses. Although small shifts in the pulse phase do not affect its shape, excessive spectral broadening degrades the pulse quality and limits its utility for different applications. Eq. 2.13, in Chapter 2, shows that the nonlinear phase shift ϕ_{NL} can be reduced either by decreasing the fibre length L or the pulse peak power P_0, or by increasing the fibre effective area A_{eff} . Hence, current research in high power amplifiers has focused in designing novel amplifier configurations [126, 127], and fibres with large effective mode areas [17, 128–131] in order to achieve higher pulse energies and peak powers.

The most common system for pulse amplification is the so called master oscillator power amplifier (MOPA). Generally, systems using MOPA configurations require a chain of stages, each one with specific characteristics to avoid pulse shape degradation while amplifying the pulse energy. In addition, depending on the pulse duration regime, and pulse central wavelength, additional external pulse amplification techniques are used to avoid the onset of pulse breaking. For example, in the femtosecond regime fibre-based chirped pulse amplification (CPA) can amplify pulses above hundreds of μJ [125], [124], while with the parabolic pulse amplification technique more moderate pulse energies, but still in the μJ regime, can be obtained [127, 132]. For picosecond pulses, it is more useful to do direct amplification of pulses with MOPAs using LMA fibres. This technique allows for pulse amplification with relatively high peak powers ($\sim$ kW), and small pulse energies ($\sim$ nJ), which can be useful in applications like nonlinear microscopy [133], supercontinuum generation [134], or frequency conversion [132].

For applications which require to work in the so called eye-safe wavelengths around 1.5 μm, Er^{3+}-doped and Er^{3+}/Yb^{3+} co-doped fibres offer a way for pulse amplification in this region. Nevertheless, one of the drawbacks of Er^{3+}-doped fibres, for high power amplification, is that the efficiency drops at high Er^{3+} concentrations due to pair-induced quenching [36, 37]. Therefore, for high power amplifiers it is common to use Er^{3+}/Yb^{3+} co-doped fibres, where the light absorbed by the Yb^{3+} ions is transferred to the Er^{3+} ions. On the one hand, this co-doping technique gives the advantage of broadening the absorption band of the fibre in the 910 to 980 nm region, which is of great importance for cladding-pump fibre amplifier configurations. However, on the other hand, control of the fibre refractive index profile (RIP) during the fabrication process is more challenging than in Er^{3+}. Such difficulties arise from the addition of phosphorus to the MCVD fibre fabrication process to enhance the energy transfer of Yb^{3+} to Er^{3+}. Phosphorus presents a highly volatile behaviour during the collapse phase of the MCVD process, reducing its presence in the fibre core. This reduction of phosphorus causes a change in the refractive index, which is commonly observed as a central dip in the fibre core. See, for example, Fig. 7.2 which shows the RIP of an in-house fabricated Er^{3+}/Yb^{3+} co-doped fibre (LF122) used in one of the experiments presented in this Chapter. A main consequence of this central dip in the refractive index is that it limits the formation of diffracted-limited beams with LMA fibres. Furthermore, Er^{3+}/Yb^{3+} co-doped fibres can decrease their efficiency at high pump power, due to spurious emissions in the Yb^{3+}-band and to excessive thermal load due to the quantum defect [15, 16]. Fabrication of Er^{3+} fibres does not present such difficulties. Therefore, step index profiles are possible to fabricate with these fibres, allowing diffraction-limited beams even with very large mode area (VLMA) fibres [17]. However, as mentioned above, due to the low pump absorption, it is necessary to increase the fibre length to compensate for the low cladding absorption. For pulse amplification such increment in the fibre length is detrimental because it reduce the onset of nonlinearities. On way to compensate for the low cladding absorption is to core-pump the active fibre. In this regard, the development of Raman lasers at 1480 nm with output powers up to 10 W delivered in single mode fibres [18], have facilitated to core-pump LMA Er^{3+} fibres, hence reducing the problem of large quantum defect and thermal loading observed in Er^{3+}/Yb^{3+} co-doped fibres [2], and allowing shorter lengths of fibre to reduce nonlinearities. Still, one of the main challenges for pulse amplification at 1.5 μm relies on the anomalous dispersion of LMA fibres. Therefore, direct pulse amplification at high gains does not follow an adiabatic amplification, causing a pulse break-up and limiting the attainable peak-power [135, 136]. In the 1.5 μm wavelength region, different groups have focused in overcoming these limitations by designing VLMA ($A_{eff} \geq 1000\mu m^2$) fibres with diffraction-limited operation with record peak power of $\sim$ 127 kW and pulse energies of $\sim$ 56 nJ.

In this chapter, I examine the direct amplification of picosecond pulses covering a wavelength range from 1535 nm to 1560 nm, with an in-house fabricated Er^{3+}/Yb^{3+} co-doped LMA fibre (LF122) and a commercial Yb^{3+} free Er^{3+}-doped LMA fibre (Er-HPA). The chapter also reports on the techniques used to reduce nonlinearities, suppression of higher order modes, and improving the amplifiers efficiencies. Although the configurations presented here have on the last amplification stage a free-space launching scheme for the 980 nm multi-mode diode laser, this type of amplifiers can be turned into compact alignment-free systems which can deliver high peak power and relatively low average power for realisation of efficient harmonic generation or supercontinuum generation.

7.2 Picosecond MOPA set-up

In order to have a better comparison of the pulse amplification at different wavelength, it was necessary to keep the oscillator signal, described in Section 6.3.2, as stable as possible. This means that the output signal seeded to the amplification stages should keep approximately the same properties in terms of output power and spectral bandwidth over the entire wavelength tuning-range. Changes in the output signal of the oscillator are due to the uneven gain profile of the active medium for a specific pump power. Hence, to keep a reasonably similar output signal, slight adjustments in the polarization state of the cavity and pump power were carried out on the oscillator while amplifying the pulses at different wavelengths.

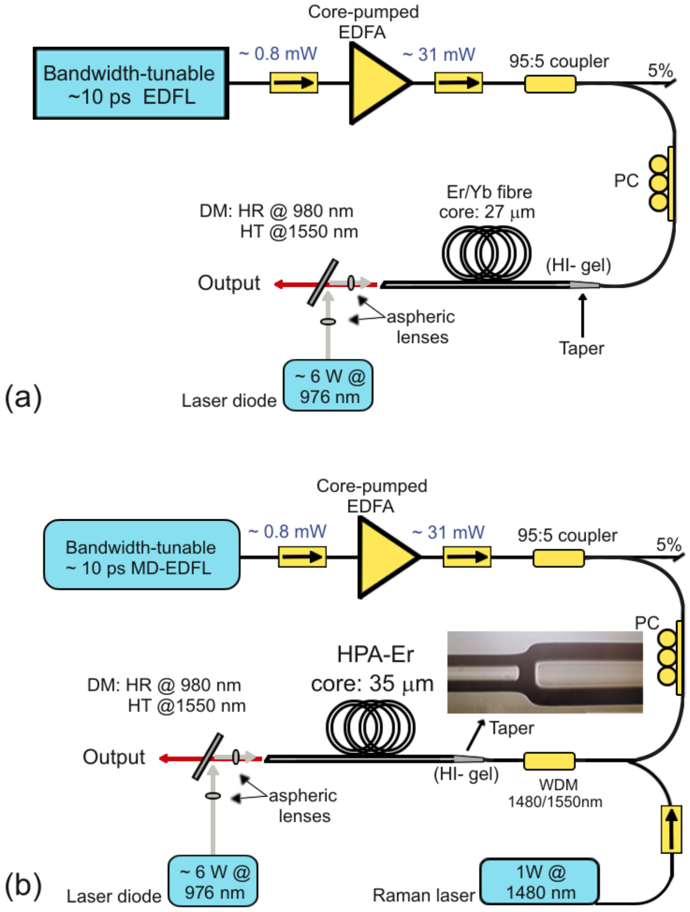

FIGURE 7.1: Schematic for the high power fibre MOPA with a (a) LMA Er^{3+}/Yb^{3+}-doped fibre and (b) LMA Er^{3+}-doped fibre. DM: dichroic mirror.

Pulse amplification of the tunable-picosecond source is carried out firstly with a pre-amplifier and then with a main power fibre amplifier. Fig. 7.1 (a) and (b) show the schematics of the Er^{3+}/Yb^{3+} co-doped fibre, and Er^{3+}-doped fibre MOPA configurations, respectively. The pre-amplifier comprises a core-pumped Er^{3+}-doped fibre with a length L_{EDF} = 1.3 m, and a mode field diameter MFD = 6 μm. In this stage the oscillator signal is amplified by $\sim$ 16 dB for most of the entire tuning range. First experiments with longer lengths of fibre showed substantial broadening of the pulse spectrum due to SPM. Therefore, cutback measurements were carried out in order to reduce the increment in the nonlinear phase of the pulse. The output signal of the pre-amplifier is then seeded to the main power amplifier through a fiberized isolator and a polarization controller. A 95:5% tap coupler spliced before the polarization controller, helped to monitor the average power and pulse shape. The average power at the output of the pre-amplifier was measured to be $\sim$ 31 mW and the pulse peak power was calculated to be $\sim$ 198 W, assuming a $sech^2$-shape pulse with pulse width of 12 ps. For these values, the calculated nonlinear length L_{NL} was $\sim$ 4 m. Therefore, the total fibre length of the passive devices spliced between the pre-amplifier and the main power amplifier is kept short ($<$ 1 m).

Two different LMA fibres were tested for the main power amplifier: an in-house fabricated double-cladding Er^{3+}/Yb^{3+} co-doped fibre, and a commercial double-cladding Er^{3+}-doped fibre. The signal seeded to both amplifiers is launched through a tapered fibre section to avoid exciting high order modes and allow single-mode operation. Both MOPAs were cladding-pumped in counter-propagation through coupling optics using a 976 nm diode laser from Apollo Instruments (model F10-976-1). In addition to the cladding-pumping scheme, the Er^{3+}-doped fibre amplifier is core-pumped in co-propagation through a 1480/1550 nm WDM coupler. The pump signal is generated by a commercial Raman laser from IPG Photonics emitting a maximum output power of 1 W at 1480nm. The hybrid configuration scheme allows to compensate for the low cladding absorption at 980 nm of the Er^{3+}-doped fibre amplifier. Therefore, shorter fibre lengths are possible, reducing the onset of nonlinearities in the fibre.

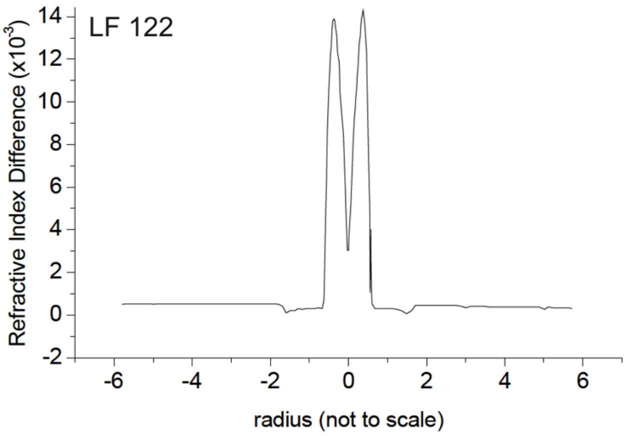

FIGURE 7.2: Refractive index profile of the in-house fabricated Er^{3+}/Yb^{3+} co-doped fibre with identification number F402- LF122. Image obtained from [3].

7.2.1 Power scaling with a large core Er/Yb co-doped fibre

The first pulse amplification tests were carried out with an in-home fabricated Er^{3+}/Yb^{3+} co-doped fibre, previously used in experiments for nanosecond pulse amplification by Dr. Codemard [3]. The advantage of using this fibre, apart from its LMA characteristics and high pump cladding absorption, was that one of its ends was already tapered and spliced to a standard single mode fibre (smf-28), facilitating its inclusion into the amplification system.

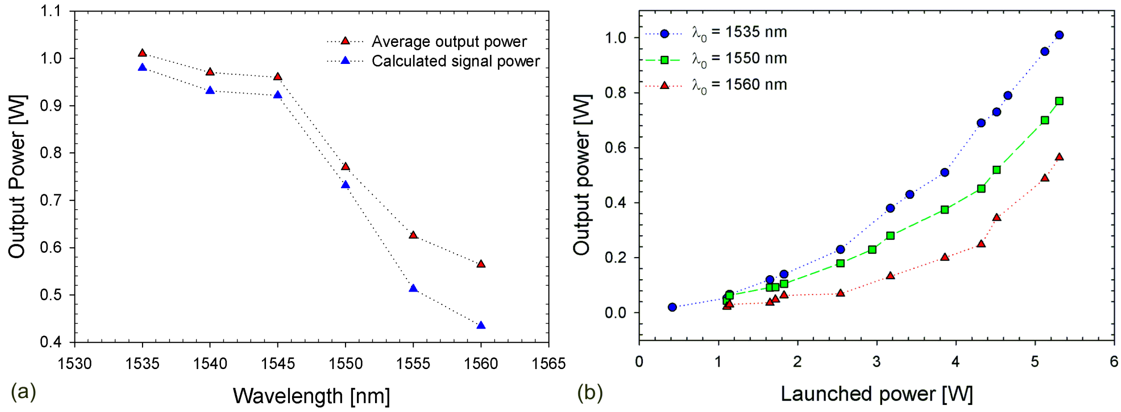

FIGURE 7.3: (a) Output power variation of the laser over the entire tuning range for different pump powers, and (b) Output power as a function of launched pump power for three different wavelengths.

7.2.1.1 Large core Er/Yb co-doped fibre characteristics

Figure 7.2 shows the fibre RIP of the Er^{3+}/Yb^{3+} co-doped fibre used in the MOPA system. The central dip observed in the refractive index facilitates the formation of ring-shaped modes (including the fundamental mode), hence imposing limitations to obtain diffraction-limited beams. The fibre has a core and inner-cladding diameter of 27 μm and 180 μm, respectively. The shape of the inner-cladding is D-shaped and has an NA of 0.2. It has a cladding absorption of $\sim$ 25.7 dB/m at 976 nm and core absorption of $\sim$ 5.7 dB/m at 1535 nm. The length of the fibre is 2.5 m and its core area is calculated to be $\sim$ 572 μm^2.

7.2.1.2 Amplification results

Output pulses are characterized with a thermal power meter, optical spectrum analyser, and non-collinear background free SHG autocorrelator. Fig. 7.3 (a) shows the output power of the MOPA as a function of wavelength. For the maximum launched pump power of 5.12 W, the maximum extracted power was 1.03 W at 1535 nm, and decreased to 564 mW at 1560 nm. The signal power (power without ASE) is calculated by integrating in linear scale the optical spectrum of the amplifier (see for example the solid

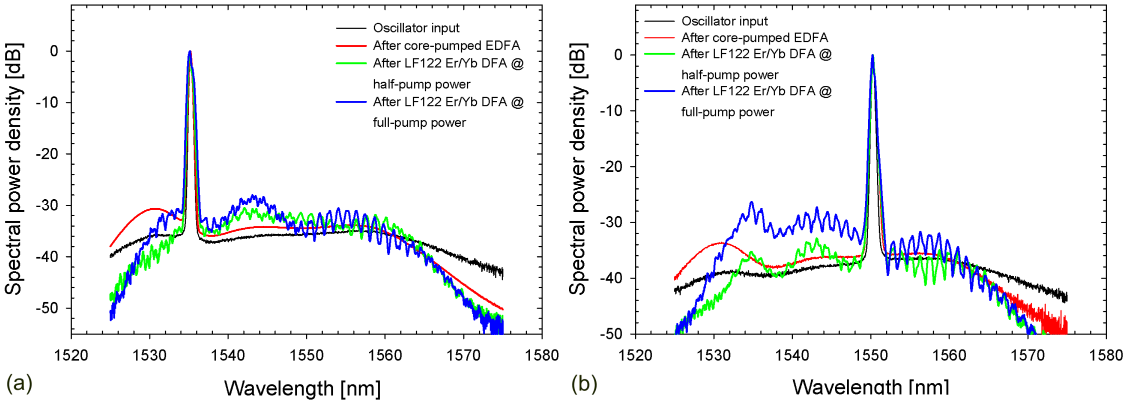

FIGURE 7.4: Normalized optical spectra at different stages of amplification for two different lasing wavelengths (a) 1535 nm and (b) 1550 nm. The spectra of the input signal and first amplification stage are measured with a resolution of 0.01 nm, while the spectrum of the second amplification stage have a resolution of 0.1 nm.

blue trace in Fig. 7.4 (a) or (b)) within a narrow wavelength band which only contains the lasing peak of the spectrum. This value is then divided by the total output power of the laser obtained by integrating in linear scale the whole optical spectrum. The resulting factor is then multiplied by the output power of the MOPA that was measured with the thermal power meter. This procedure is followed for each wavelength shown in Fig. 7.3 (a). Fig. 7.3 (b) shows the nonlinear behaviour of the output power as a function of the launched pump power. Above 4.5 W of launched pump power, slope efficiencies of $\sim$ 36 % and $\sim$ 26 % are achieved at 1535 nm and 1560 nm, respectively. The nonlinear behaviour of the laser output power observed in Fig. 7.3 (b) is a consequence of the pump lasing peak shifting towards the 976 nm absorption peak of the Er^{3+}/Yb^{3+} co-doped fibre.

Figure 7.4 (a) and (b) show the evolution of the optical spectrum through the two amplification stages for a lasing wavelength of 1535 nm and 1550 nm, respectively. The spectrum of the core-pumped amplification stage shows an excitation level of $\sim$ 65% for the EDFA. For this excitation level it is possible to achieve the same gain for different wavelengths within the entire tuning-range of the laser while keeping a signal to ASE extinction ratio $>$ 30 dB. For 2.5 m of fibre the main MOPA presents two dominant ASE peaks: one at 1535 nm and the other at 1542 nm. Higher gain saturation of the signal at shorter wavelengths reduces the ASE extinction ratio to $\sim$ 30 dB at 1535 nm, compared to the ratio of $\sim$ 27.5 dB at 1550 nm. An increment in the fibre length can generate more gain at longer wavelengths due to Er^{3+} re-absoprtion [16]. However, this will reduce the onset of nonlinearities and limit the pulse peak power.

Adjustments in the polarization controller of the ML laser modify the pulse width between 11.5 ps and 8.7 ps. Fig. 7.5 (a) and (b) shows the autocorrelation measurement before (red trace) and after (blue trace) amplification for the largest and shortest pulse

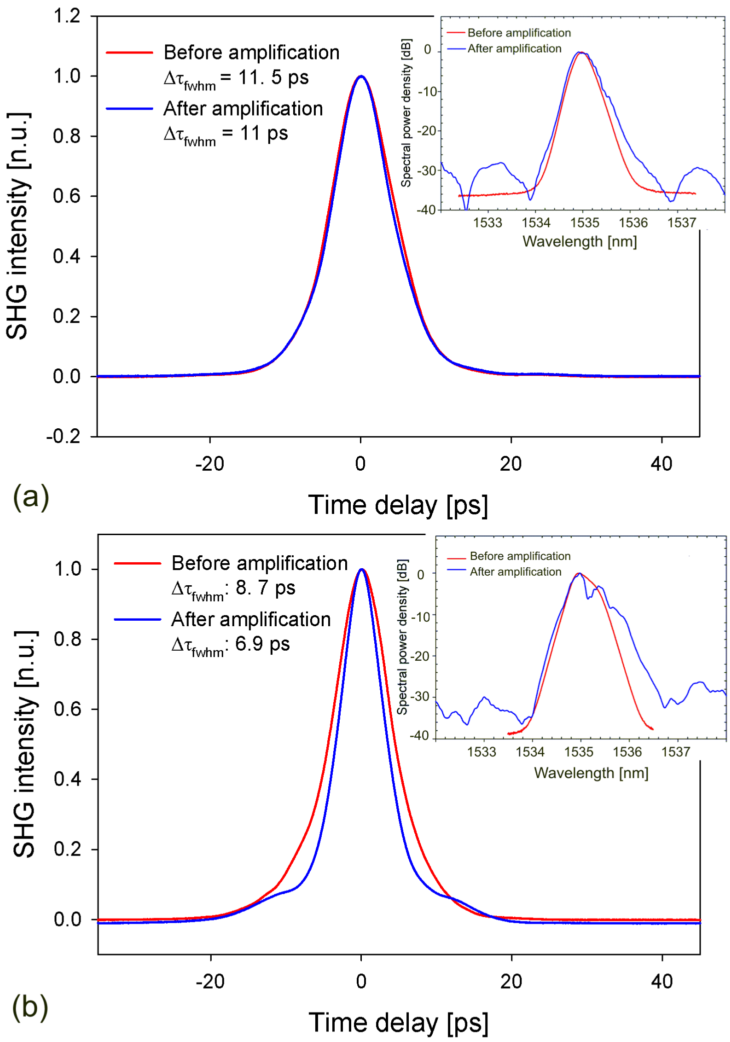

FIGURE 7.5: Autocorrelation measurement for a pulse width of (a) 11.5 ps and (b) 8.5 ps. Insets: spectra measured before (red trace) and after (blue trace) amplification.

generated in the oscillator, respectively. The inset shows the corresponding pulse spectra. For an input pulse width $\tau_{FWHM} \sim 11.5$ ps, the pulse shortens by approximately 4 % after amplification. However, if the input pulse is $\tau_{FWHM} \sim 8.7$ ps, the pulse suffers temporal compression after amplification. This behaviour is observed in the autocorrelation measurement where the pulse width decreases to ∼ 6.9 ps, and the pulse energy is spread to the pulse wings forming a pedestal at the bottom of the autocorrelation trace. The pedestal indicates the onset of pulse break-up [38]. For the largest pulse width and maximum output power, a pulse energy $E_p \sim 74$ nJ was calculated assuming a $sech^2$ pulse shape and a peak power of $P_p \sim 5.7$ kW.

The beam quality factor (M^2) of the laser is characterized with a scanning-slit beam-profiler (model: NS-PYRO 9/5) from Photon Inc, see Fig. 7.6. For a maximum output power $P_{out} = 1.03$ W at 1535 nm the laser has an $M_x^2 \sim 2.0$ and $M_y^2 \sim 1.8$. The difference in the M^2 factors, for the two orthogonal directions to the beam axis, shows that the

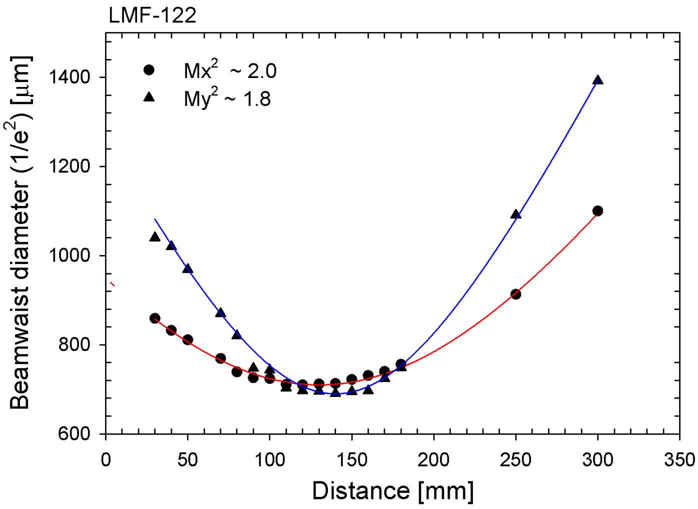

FIGURE 7.6: Beam quality measurement at the output of the LMA Er^{3+}/Yb^{3+} co-doped fibre for a maximum output power P_{out} = 1.03 W at 1535 nm.

laser beam is not circularly symmetric.

7.2.2 Power scaling with a large core Er-doped fibre

The availability of a commercial 1 W single mode Raman laser operating at 1480 nm [1], allowed me to replace the Er^{3+}/Yb^{3+} co-doped fibre with a LMA Yb^{3+}-free Er^{3+}-doped fibre in the main MOPA configuration. The advantage of this fibre relied on its larger core size, which helps minimizing the pulse spectral broadening while increasing the pulse peak power. In addition, the more uniform index profile of this fibre compared to that of the Er^{3+}/Yb^{3+} co-doped fibre can provide better beam quality. Nevertheless, as explained in Section 7.1, the low cladding absorption of LMA Er^{3+}-doped fibres cannot generate enough gain for short lengths of fibre. Thus, the Raman laser was useful for core-pumping the fibre, allowing enough gain for pulse amplification while keeping the fibre length relatively short.

7.2.2.1 Large core Er-doped fibre characteristics

The LMA Er^{3+}-doped fibre is a commercial fibre from CorActive (model: HPA Er-35-0). The fibre has a core and cladding diameter of 33 μm and 135 μm, respectively. The NA of the inner cladding is 0.37. It has a cladding absorption of 0.5-1.5 dB/m and 3-5 dB/m at 980 nm and 1530 nm, respectively. Figure 7.7 shows the fibre RIP measured with a refractive index profiler from Photon Kinetics. The RIP of this fibre compared

---

[1] The commercial Raman laser from IPG Photonics was borrowed from Dr. Trevor Newson's laboratory, who kindly agreed to lend me the device for a couple of weeks to carry out these experiments.

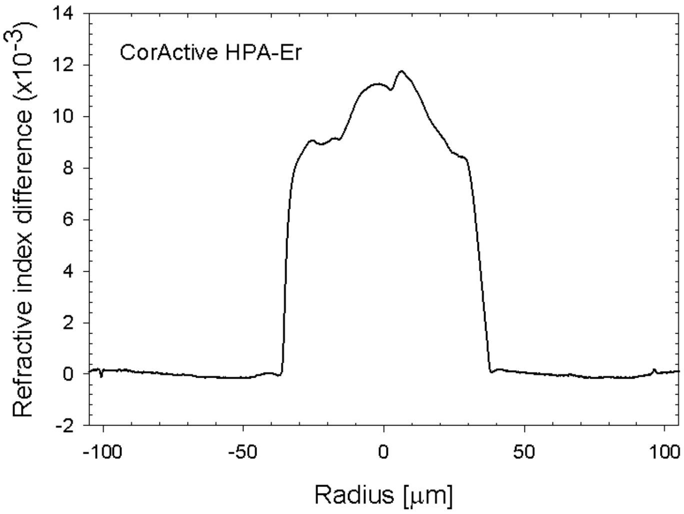

FIGURE 7.7: Refractive index profile of the CorActive LMA Er^{3+}-doped fibre with product identification number HPA Er-35-0.

to that one of Fig. 7.2 (Er^{3+}/Yb^{3+} co-doped fibre), do not present a central deep. Nevertheless, it shows a core asymmetry which can deteriorate the beam quality of the laser. The V-number of the fibre is calculated to be $\sim$ 6.3 at 1550 nm, considering a core NA value of 0.09. A rough estimate of the number of modes N_{modes} propagating in the fibre core yielded a value of $\sim$ 20. As in the previous section, a tapering technique was used to reduce the number of modes in the fibre. Tapering of one of the fibre ends was carried out with a commercial glass processing platform from Vytram technologies (model GPX-3000). The core radius r_{core} of the LMA fibre was tapered to reach a final core radius $r_{final} \sim 6.37$ μm needed for single mode operation.

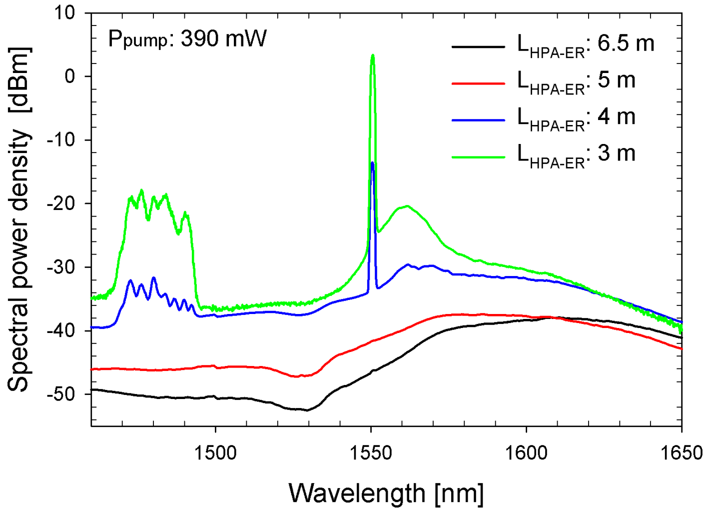

FIGURE 7.8: Laser output spectrum for different fibre lengths.

The pump (1480 nm) and signal wavelengths are launched into the tapered end of the LMA Er^{3+}-doped fibre through a standard single mode fibre (see picture in Fig. 7.1

(b)). The splice loss between the single mode and Er^{3+}-doped fibre was measured to be ∼ 0.3 dB. The other fibre end is cladding-pumped with the multimode diode laser, described in the previous section, through coupling optics. The fibre was angle cleaved to avoid any back reflection and 85% of coupling efficiency was achieved for a pair of aspheric lenses with NA = 0.5 and effective focal length $efl = 8$ mm. The temperature of the laser diode was also adjusted from 27 °C to 22 C °. The temperature adjustment modified the maximum output power delivered by the laser diode and shifted the lasing peak to shorter wavelengths. In this regards, the laser diode output power increased by ∼ 20% and delivered a maximum output power of 7.77 W.

7.2.2.2 Amplification results

Based on the cladding absorption parameters of the fibre at 980 nm, it was decided to have at least 7 metres of fibre to allow a cladding-pump absorption ≥ 10 dB. Nonetheless, based on experimental results the fibre core absorption limited the length of the fibre. Fig. 7.8 shows the output spectrum of the MOPA system while core-pumping the LMA fibre with a single mode laser diode operating at 1480 nm and with a seeding signal formed by the output pulses of the pre-amplifier described in Section 7.2. Measurements taken while cutting back the fibre showed that for 4 metres of fibre length (solid blue trace), the input signal is not completely absorbed by the active ions of the fibre core. Although a higher signal to ASE ratio is achieved for a fibre length of 3 metres, shorter fibre lengths also mean a reduction of the fibre absorption, therefore it was decided to work with a fibre length close to 4 metres in order to maximize the cladding absorption.

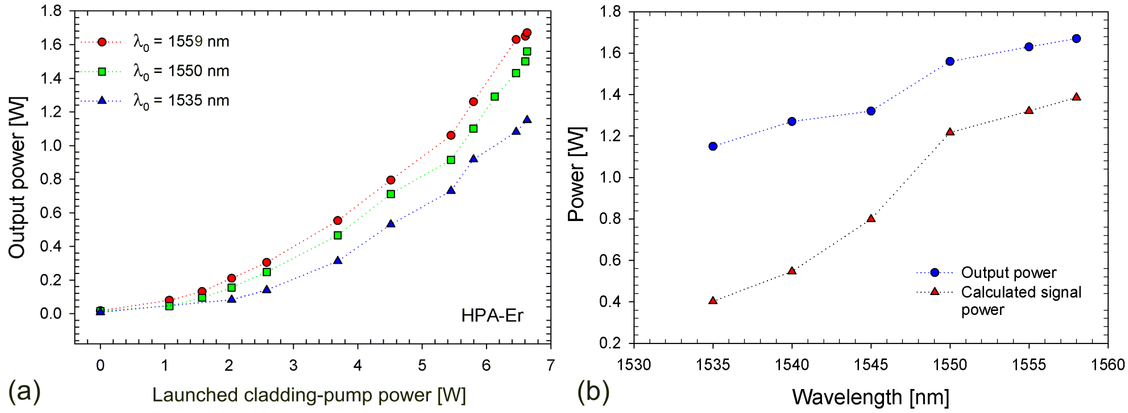

FIGURE 7.9: (a) Output power as a function of launched pump power for three different wavelengths, and (b) Total output power (blue dots) and calculated signal power (red triangles) over the entire tuning range.

The MOPA was seeded with 8.4 ps pulses with repetition rate of 13 MHz and average power of ∼ 33 mW. A maximum of 1 W and 6.6 W was core and cladding-pumped into the LMA fibre, respectively. For $L_{EDF} = 3.7$ m, the 1 W core-pumped light launched into the fibre does not generate enough gain to amplify the seed signal. A maximum average output power of ∼ 20 mW is measured while core-pumping the amplifier with the maximum pump power (1 W) of the Raman laser. Fig. 7.9 (a) shows the amplifier average output power as a function of 980 nm pump power for three different wavelengths: 1559 nm (red circles), 1550 nm (green squares), and 1535 nm (blue triangles). As explained in the previous section, the nonlinear evolution of the output power as a function of the launched power is a consequence of the pump lasing peak shifting towards the 980 nm wavelength. In this configuration, longer wavelengths present a better efficiency compared to shorter wavelengths. Fig. 7.9 (b) shows the average output power (blue dots) and the calculated signal power (red triangles) of the LMA Er^{3+}-doped fibre amplifier over the entire tuning range. A maximum average output power of 1.67 W and 1.15 W is measured at 1559 nm and 1535 nm, respectively. This corresponds to a drop in the output power of ∼ 1.6 dB along the entire tuning range. The signal power (power without ASE) is calculated from the optical spectra measurements in Fig. 7.10. For the 1559 nm and 1535 nm lasing wavelengths the signal power was calculated to be 1.39 W, and 0.4 W, respectively. This represents a drop in the signal power of more than 5 dB. Therefore, pulse amplification at shorter wavelengths is limited by the growth of ASE at 1560 nm. The spectral signal to ASE extinction ratio at longer wavelengths is measured to be ≥ 27 dB while for shorter wavelengths decreases to ∼ 10 dB.

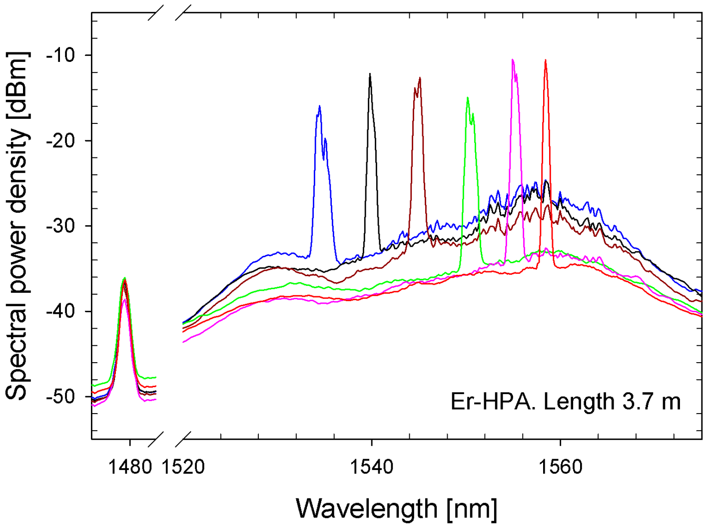

FIGURE 7.10: Output spectrum over the entire tuning-range of the ML laser. The spectrum is measured with a resolution of 0.1 nm.

For low average output powers $P_{out} \leq 700$ mW, the beam quality factor of the MOPA for the x and y- axis were measured to be $M_x^2 \sim 1.2$ and $M_y^2 \sim 1.1$, respectively. Nevertheless, it increased to $M_x^2 \sim 2.45$ and $M_y^2 \sim 2.41$ for the maximum output power (see Fig. 7.11). This result means that even though both the signal and pump (1480 nm) beams propagates in the fundamental mode through the tapering splice technique, at higher cladding-pump powers, the preferential gain for the fundamental mode competes with higher order ASE modes.

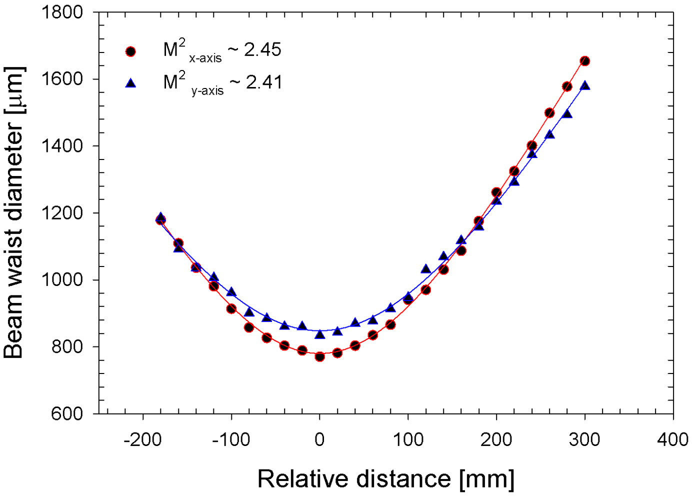

FIGURE 7.11: Beam quality measurement at the output of the LMA Er^{3+}-doped fibre for a maximum output power P_{out} = 1.03 W at 1535 nm.

Figure 7.12 (a) and (b) show the autocorrelation and output spectra measurement at different stages of the amplification system, respectively. The input pulse width of τ_{FWHM} = 8.5 ps does not suffer temporal variations after amplification. However, the pulse spectrum broadens in each amplification stage due to SPM. The initial pulse bandwidth of $\Delta\lambda = 0.26$ nm is broadened to $\Delta\lambda = 0.57$ nm for the maximum average output power. The maximum pulse energy and peak power at 1559 nm is calculated to be 11 kW and 106 nJ, respectively.

7.3 Conclusions

In this Chapter, two different MOPA systems are proposed for amplification of picosecond pulses at different wavelengths. The first configuration comprises a LMA cladding-pumped Er^{3+}/ Yb^{3+} co-doped fibre amplifier delivering pulses with peak powers and pulse energies of ~ 5.7 kW and 74 nJ, respectively. Higher peak powers are limited by the onset of pulse-breaking. The second configuration comprises a LMA Yb^{3+}-free Er^{3+}-doped fibre, delivering pulses with peak powers and pulse energies of ~ 11 kW and 106 nJ, respectively. Higher peak powers can be achieve but are limited by pump power at longer wavelengths, and by ASE at shorter wavelength. The novelty of the second configuration is that it includes a hybrid pumping configuration to tackle the low absorption of the Er^{3+}-doped fibre, enabling to reduce the active fibre length. Thus, it is possible to delay the onset of pulse-breaking, due to excessive nonlinearities. Although the configuration was designed to ensure preferential gain for the fundamental mode by exciting it through the tapered section of the fibre, the cladding-pumped scheme deteriorates the quality beam factor by exciting higher order modes in the fibre. A M^2 factor of 2.4 was achieved for maximum output power. High peak powers with relatively high

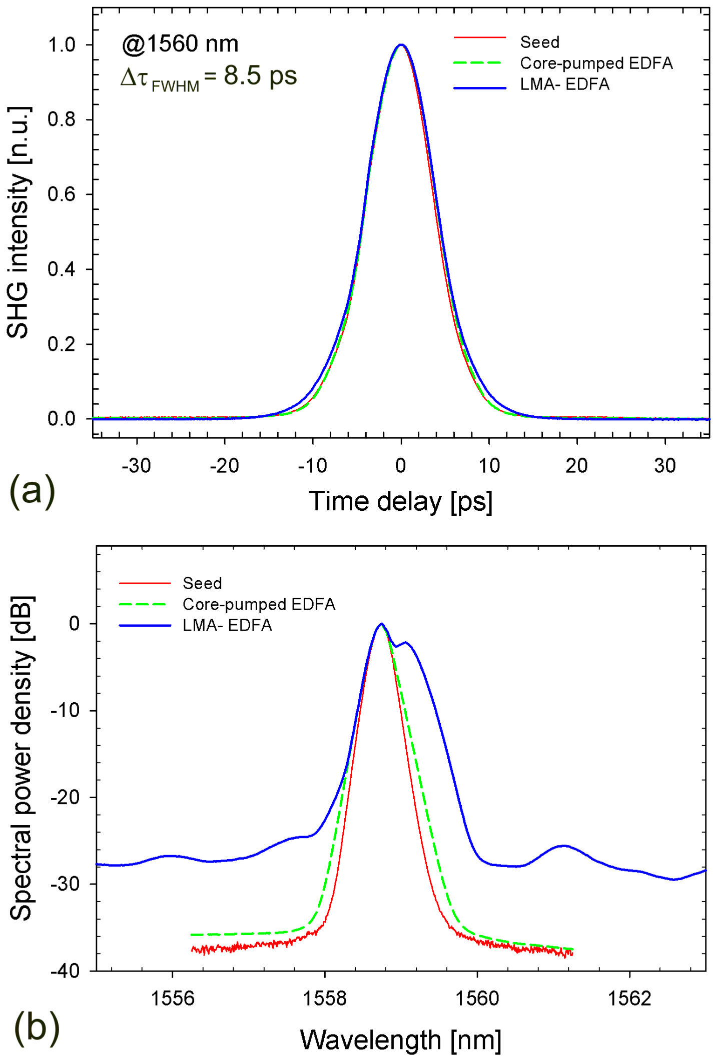

FIGURE 7.12: (a) Autocorrelation traces and (b) pulse spectra measurements at different stages of the Er^{3+} amplification system.

average output power suggest that this compact source can be suitable for applications such as supercontinuum generation or tunable sources by second-harmonic generation. Regarding the latter, in the Future Work section, I will describe in more detail the requirements to achieve a high-efficient second-harmonic generation.

Chapter 8

Broadband Noise-Like Pulse Erbium-Doped Fiber Ring Laser

In this Chapter I propose and implement an all-fiberized Er^{3+}-doped fibre ring laser generating linearly polarized picosecond pulses with 135-nm bandwidth and excellent spectral flatness. The pulse energy and width are readily reconfigurable from 0.7 nJ to 1.1 nJ and from 6.5 ps to 220 ps, respectively, via controlling the cavity finesse and/or pumping power. The relative intensity noise (RIN) characteristics of the source are also investigated and compared to a commercial passively generated super-continuum source. The overall performance of the source is much superior to ASE-based broadband sources in terms of spectral bandwidth as well as power. Such optical source should be useful for many applications, such as optical fiber sensing, or optical coherence tomography that require broadband outputs with relatively high average power.

8.1 Overview of the noise-like pulse regime

Over the past decades fibre-based ultrashort pulse optical sources have received a lot of research attention and a variety of cavity configurations and pulse-generating techniques have been introduced [6, 42, 121]. As explained in Chapter 3 different types of optical pulses can be generated from fiber-based sources depending on the dispersion property of the cavity (solitons, Gaussian pulses, similaritons, etc.). Noise-like pulses (NLP) [137–142], unlike such fixed pulse forms, are another interesting type of pulses that can be extracted from a fiber laser. NLPs may be regarded as a bunch of ultrashort pulses with random pulse widths and peak powers that circulate in the cavity at the fundamental roundtrip frequency [139]. Such pulses eventually form a stable and very broad spectral emission, which is sometimes even broader than the gain bandwidth [140] of the laser medium.

The early extensive study on NLPs was carried out by Horowitz et al. [137]. The authors explained the formation of the pulses in terms of a combination of strong birefringence in the laser cavity and the transmissivity of the nonlinear medium. Later on, the role of the cavity dispersion and cavity length in the NLP duration and spectral bandwidth was also investigated by Horowitz et al. [138] and Kang et al. [139]. In Ref. [138] shorter cavities, with low dispersion, yielded shorter pulses while in Ref. [139] dispersion-mapped cavities with large net cavity dispersion enhanced the spectral bandwidth of the NLPs. More recent studies explained the formation of NLPs in terms of soliton collapse and positive cavity feedback in the laser and showed that NLPs could be generated independently of the dispersion configuration [140, 141]. While there may be better or alternative explanations for the formation of the NLPs in a fibre laser cavity, it is noteworthy that the NLP regime has a unique feature that it can generate broad and smooth optical spectra in a relatively simple and compact configuration. In terms of bandwidth, such fiber-based broadband light sources should be very useful in areas such as optical metrology or optical coherent tomography (OCT), where short coherence lengths are ultimately required. However, it is also necessary to justify the detailed noise characteristics of the NLP-based optical sources because the stability and noise characteristics are crucially linked to the sensitivity and practicality of the optical sources.

Recently, an increasing number of reports on the broadband operation of NLP-based fiber sources have been published [142–144]. Within those, the work of Zhao et al. [142] has a record result in terms of broad bandwidth operation with 120 nm bandwidth with an average power of ∼ 2 mW when pumped at 700 mW. However, its conversion efficiency was limited to below 0.3% and it supported rather long temporal pulses of ∼ 50 ps. In this Chapter I propose and investigate a linearly polarized, all-fiber Er^{3+}-doped fibre ring laser that generates picosecond NLPs at 1570 nm with 135-nm bandwidth, excellent temporal/spectral stability, and improved conversion efficiency of ∼ 3%. The broadband NLPs are obtained by exploiting fiber birefringence and nonlinearity in the cavity combined with a highly nonlinear fibre (HNLF) for Raman gain enhancement. This is to the best of my knowledge, the broadest spectral bandwidth directly generated from an Er^{3+}-doped fibre ring laser. The pulse width and spectral bandwidth of the laser is adjustable with the pump power and/or the internal polarization controller (PC) which determines the cavity birefringence and the output coupling ratio (OCR). The experimental results show that the laser cavity can operates in two clearly different types of regimes apart from a continuous-wave (CW) regime: a self-phase-modulation (SPM)-dominant NLP regime and a Raman-extended NLP regime, which are to be discussed in details in the following section.

8.2 Experimental setup

Figure 8.1 shows the experimental arrangement for the laser source. The cavity consists of $\sim$ 2.5 m polarization maintaining (PM) Er^{3+}-doped fibre with an absorption coefficient of 8.4 dB/m at 1480 nm and a birefringence of 2.2×10^{-4}. The PM Er^{3+}-doped fibre is pumped through a wavelength-division-multiplexed (WDM) coupler (1480/1550 nm) with two laser diodes (LDs) delivering a maximum total power of 270 mW at 1480 nm. The other components in the cavity include a 12-m HNLF with nonlinear coefficient $\gamma = 10\ W^{-1}km^{-1}$, a fiberized isolator to ensure unidirectional lasing, a 99/1 coupler to monitor the intra-cavity signal, a polarization controller to adjust the polarization state inside the cavity and also to control the output-coupling ratio of the laser, and a fiberized polarization beam splitter (PBS) to obtain linearly polarized output pulses and to excite only one of the polarization modes in the PM-Er^{3+}-doped fibre. Excitation of only one polarization mode in the gain fibre was the main reason to counter-pump the laser cavity [1]. The total length of the cavity is $\sim$ 22 m with an overall dispersion value of $\beta_2 = 0.23$ ps^2 at 1550 nm. The GVD parameter of the PM-Er^{3+}-doped fibre and the HNLF are numerically calculated, via analyzing its refractive index profiles (FRIPs), to be $\beta_2^{EDF} = 17.85$ ps^2/km and $\beta_2^{HNLF} = 29.3$ ps^2/km at 1550 nm, respectively. The rest of the cavity is formed of a standard single-mode fiber (Corning SMF-28) with a GVD parameter value of -20 ps^2/km.

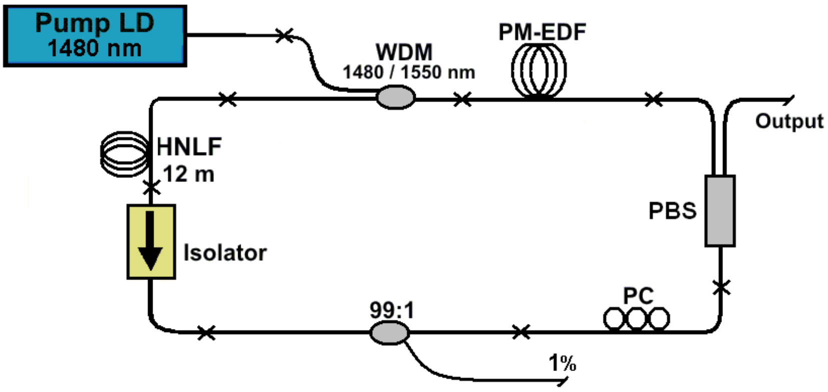

FIGURE 8.1: Schematic diagram of the Er^{3+}-doped fiber ring laser. LD: laser diode, PM-EDF: polarization maintaining Er^{3+}-doped fibre, PBS: polarization beam splitter, PC: polarization controller.

---

[1] The reader should notice that the only polarization maintaining (PM) components in the cavity are the PM- Er^{3+}-doped fibre and the output ports of the fiberized PBS. Therefore, it was decided to align and fusion splice the fast axes of the active fibre and PBS output port. In such configuration, a counter-propagating signal is strictly launched into the fast-axis of the active fibre and its power controlled with help of the PC located before the PBS. These two benefits could not be achieved in a co-propagating configuration because the WDM coupler spliced to the active fibre is not a PM component and therefore control of the polarization state in this component is not possible.

8.3 Experimental results

The laser could operate in two main, clearly different regimes which were controlled by the pump power and the OCR (via adjusting the PC). In the first regime, the laser generated a train of "square-shape" NLPs with a fundamental repetition rate of 9.1 MHz. This regime appeared for pump powers above 120 mW. The average width of the envelope of the NLPs was around 90 ps, measured with a fast photodetector (20 GHz bandwidth) and a digital comunication analyzer (DCA) (20 GHz bandwidth), and could be varied with both, the pump power and the output coupling ratio (see Fig. 8.2). The autocorrelation traces of these pulses are depicted in the inset of Fig. 8.2. The traces show a narrow spike with sub-picosecond width located on top of a broad asymmetric pedestal that covered the maximum scan range of around 110 ps of the autocorrelator. The shape of the autocorrelation indeed represents a "noise-like" feature of the complicated intensity pattern resulting from the bunch of pulses circulating in the cavity at the fundamental roundtrip frequency [140].

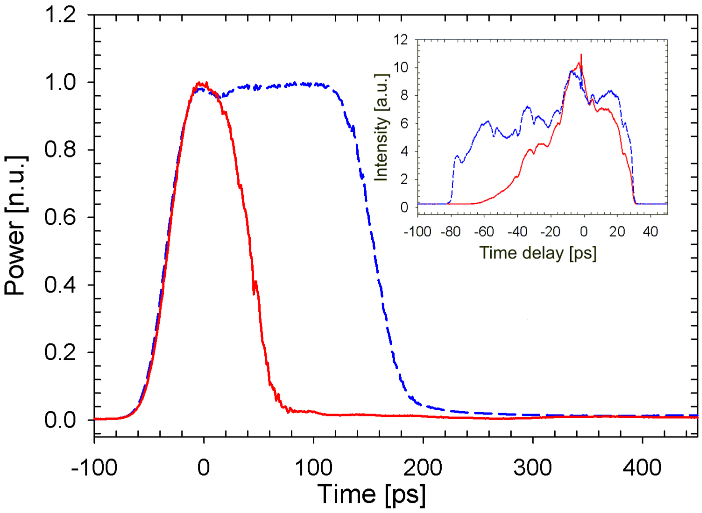

FIGURE 8.2: Time traces of the "square-shape" NLPs generated by the Er^{3+}-doped fibre ring laser. Pulse width is varied with either pump power or output coupling ratio. Inset shows their respective autocorrelation traces.

Figures 8.3 (a) and 8.3 (c) show the behavior of the NLPs in terms of pulse width or peak power as a function of the output power, respectively. It should be noted that for these figures I consider the bunch of pulses as a single entity. For Fig. 8.3 (a) the PC in the cavity remains fixed at the OCR of $\sim 25\%$ as the pump power changes, while for Fig. 8.3(c) the pump power remains constant at $\sim$ 180 mW as the PC is adjusted, thus modifying the OCR of the cavity. In Fig. 8.3 (a) one can see that both the pulse width and the average output power of the laser increase with the pump power, resulting in an approximately constant peak power. For this case, the optical bandwidth of the laser does not show any noticeable changes (see Fig. 8.3 (b)), which agrees with previous results reported in [137] and [141]. However, a slightly different behavior can be observed in Fig. 8.3 (c), where the pulse width decreases at higher output powers, allowing the peak power to increase. Consequently, the increase in the peak power gives rise to an increase in the spectral bandwidth of the laser (see Fig. 8.3 (d)). For instance, one can see that the spectral bandwidth is noticeably increased from 13 nm to 17.2 nm as the pulse width changes from ∼ 220 ps to ∼ 90 ps. This spectral broadening is mainly attributed to the increase of SPM due to the excessive peak power of the individual pulses within the NLP envelope. Therefore, from hereafter I will refere to this regime as the SPM-dominant NLP regime. It should also be noted that the actual peak power of the individual pulse is significantly higher than the peak power of the envelope pulse. In Fig. 8.3 (a), and 8.3 (c), the difference between the maximum output power right before the SPM-regime collapses is related to the polarization state of the cavity. It was observed that slight adjustments in the polarization state of the cavity had more influence on the pulse width and pulse spectrum than adjustments on the pump power. In this sense, pulses were more likely to remain stable by adjusting the pump power (within a range of ∼ 110 mW) rather than the polarization controller.

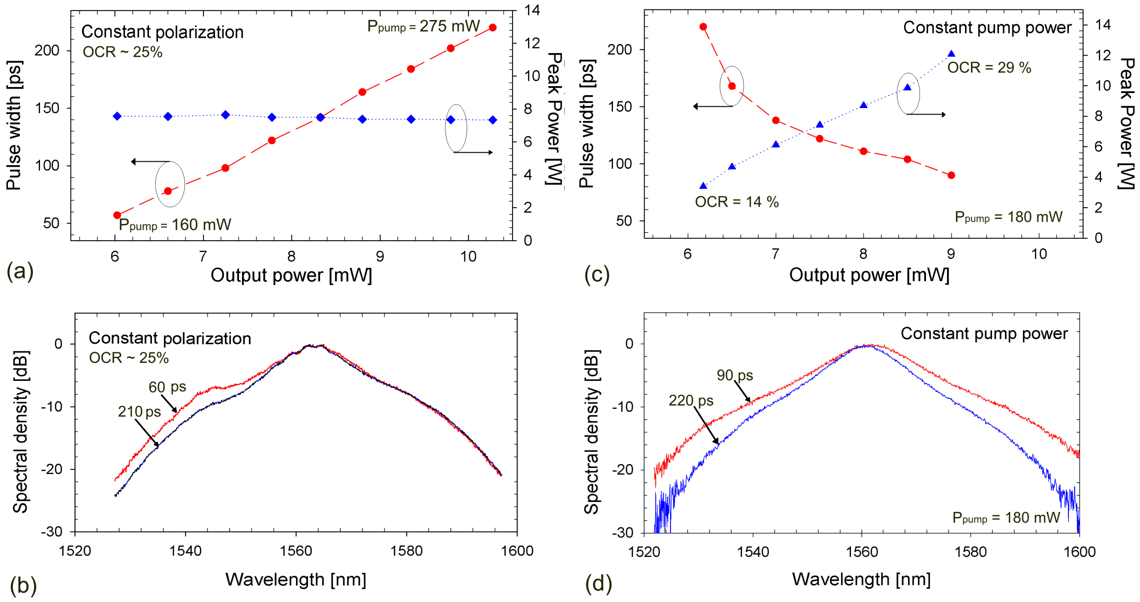

Figure 8.3: Pulse width and peak power as a function of the output power of a bunch of noise-like pulses for a (a) constant polarization state and (c) constant pump power. Behaviour of the optical spectrum of NLPs for (b) constant pump power and (d) a constant polarization state. OCR: Optical coupling ratio, and P_{pump}: Pump power.

A second operating regime was obtained by pumping the laser at its maximum pump power of around 270 mW and by adjusting the polarization state of the cavity to maximize the internal power density. In this regime, a smooth and nearly flat spectral emission with an optical bandwidth of ∼ 135 nm is generated (see Fig. 8.4 (a) black trace). The average output power of the laser in this regime is 6.9 mW and has an OCR ∼ 11%. Fig. 8.4 (b) shows the autocorrelation trace of the output pulses (solid black trace), where a narrow sub-picosecond coherent spike is observed still sitting on the top of a pedestal of $\sim$ 6.5 ps width. The inset of Fig. 8.4 (a) shows the RF spectrum at the fundamental frequency of the laser, measured with a fast photodetector (22 GHz bandwidth) and a spectrum analyzer (22 GHz bandwidth). In this regime, it is only observed a clean and sharp, fundamental frequency component with no significant noise bands at each side of the spectrum (even for higher frequency resolutions), indicating the non-existence of intermodal noise. It is worth saying that the formation of this regime is formed from cw and not from SPM-dominant regime, where pulse formation collapses before reaching a broad flat spectrum. The initial formation of the broader spectrum appears as a series of sharp spikes covering what then becomes the broad bandwidth of the laser output. Slight adjustment of the polarization controller can help to maximize the bandwidth or stabilize the laser. Unstable spectra were usually characterized by a low power level on the longer wavelength side of the spectrum, and for a broader pedestal on the autocorrelation trace. See for example the solid red trace in Fig. 8.4 (a) and (b), respectively. Nevertheless, it should be noted that the direction of the spectral broadening is only towards the longer wavelengths, which clearly indicates that the broadening is due mainly to successive Raman scatterings in the cavity fiber [142]. Thus, this regime is called within this work the Raman-extended NLP regime. In comparison with the SPM-dominant regime, one can clearly see that the spectrum is less noisy in this regime. This improvement is attributed to the fact that the excessive peak powers of the irregular, spiky pulses must be regulated via transferring their excessive energy to the longer wavelengths spectral bands. Consequently, once the peak powers of the NLPs are high enough to break into Raman scatterings, NLPs form a Raman-extended, broad spectral output with relatively improved noise characteristics.

Since the formation of irregular bunches of NLPs results in intensity fluctuation in time, the relative intensity noise (RIN) analysis must be a good measure for quantifying the noise characteristics of NLPs. The RIN is a common quantification of the amplitude noise of a laser system and it is one of the major causes of deterioration of the sensitivity of optical systems. In addition, the RIN of the NLPs was compared to the RIN characteristics of a commercial supercontinuum (SC) source ($\Delta\lambda > 1800$ nm) that is in principle based on the combination of a stable mode-locked fiber laser and a nonlinear optical fibre. The model of the supercontinuum source is a FemtoPower1060 SC400 from Fianium delivering a total output power of 4 W (average spectral power density $>$ 2mW/nm) with a fundamental repetition rate of 40 MHz, and spectral flatness $<$ 6 dB. In general, the intensity noise varies as a function of the optical intensity, optical bandwidth, and spectral shape of the optical input that is incident to the photodetector [145]. Therefore, to carry out a fair comparison of the RIN values of both sources, the optical signal from each of the sources was filtered with a 12 nm bandwidth optical filter centred at a wavelength $\lambda_c = 1550$ nm (see dotted lines in Fig. 8.6 (a)). The experimental setup to measure the RIN of both sources is shown in Fig. 8.5. The filtered light of the broadband source is split in two with help of a 50:50 coupler. The light from one port of the coupler is then launched into a photodetector (5 GHz bandwidth).

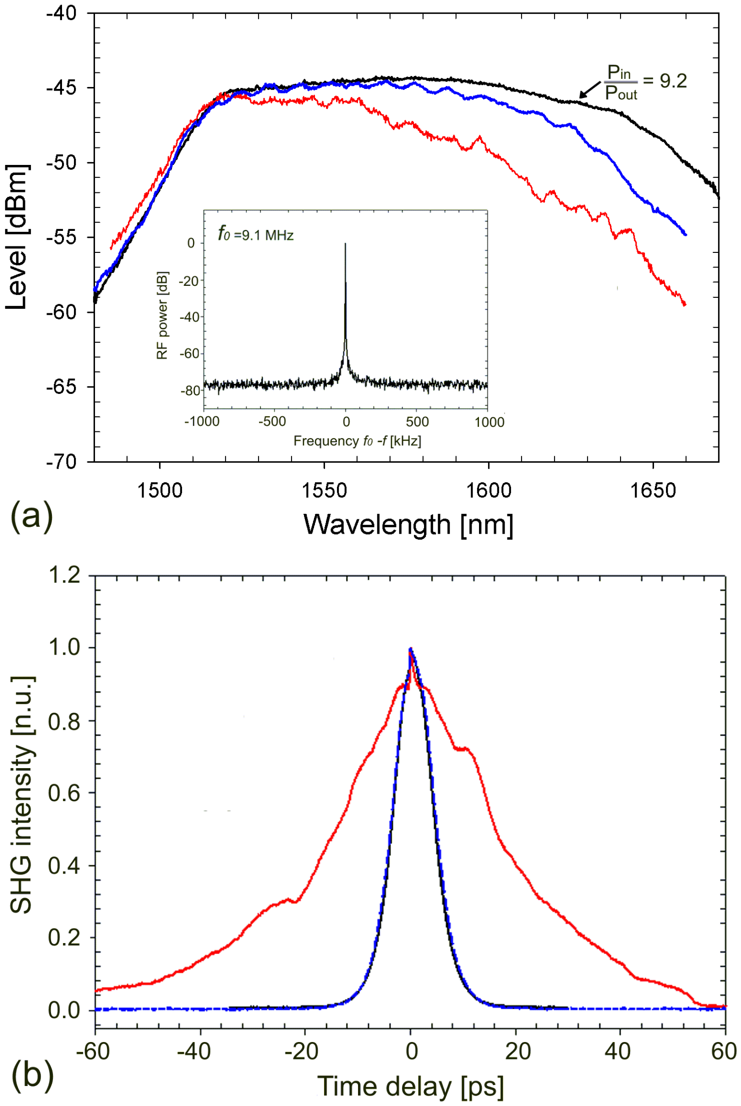

FIGURE 8.4: (a) Optical spectrum and (b) autocorrelation trace of the Raman-extended NLP regime for three intermediate states: stable (black solid trace), noisy-stable (blue solid trace) and quasi-stable (red solid trace), respectively. Inset shows the RF spectrum of the fundamental roundtrip frequency f_o= 9.1 MHz with a resolution bandwidth of 300 Hz. The optical spectrum is measured with a resolution of 0.1 nm. Pin: Intracavity power, Pout: Output power

The DC component of the electrical signal generated by the photodetector is removed with help of a bias-T and monitored with an oscilloscope, while the AC component is launched into an RF-spectrum analyser with 22 GHz bandwidth. The other output port of the optical coupler is used to monitor the optical power and to measure the optical spectrum of the source. During the measurements, light launched into the photodetector was kept at the same optical power. The RIN spectra of the NLP source and SC source were measured at their carrier frequencies ($f_c^{NLP} = 9.1$ MHz and $f_c^SC = 40$ MHz) and normalized to the peak level of the carrier frequency.

Fig. 8.6 (a) shows the normalized optical spectrum of the two broadband sources used

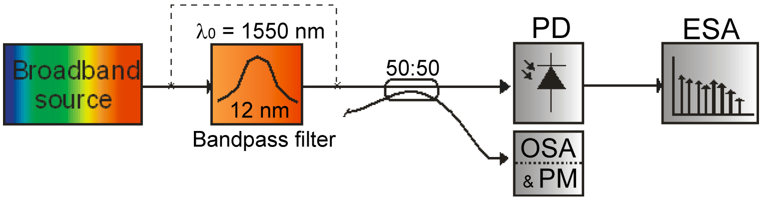

FIGURE 8.5: Experimental setup to measure the RIN of a NLPs source and commerical supercontinuum source. PD: photodetector, OSA: Optical spectrum analyzer, PM: power meter, ESA: Electrical spectrum analyzer.

in the experiment before (solid traces) and after (short-dashed traces) being filtered. Fig. 8.6 (b) shows the RIN of the NLPs source and the SC normalized to their carrier frequencies. The graphic is plotted relative to the fundamental carrier frequency of the source. Fig. 8.6 (b) shows that the noise level of the SC and NLPs sources is roughly the same (-104 dBc/Hz) for a frequency range from 10 kHz to tens of MHz. However, the noise level of the NLPs is higher at low frequencies $\leq$ 1 kHz. The peak at 50 Hz is presumed to be an electrical interference caused by AC power lines. Although there may be many contribution factors to the excessive noise level at low frequencies, including pump power fluctuation, the discrepancy of the noise levels at low frequencies between the SC and NLP sources must be due to the slow fluctuation of the amplitudes of NLPs circulating in the cavity. The high noise level in both sources is expected due to spontaneous Raman emission during the generation of the broad band spectrum for both the SC and the NLPs [146]. However, it is clearly noted that the RIN of the NLP source can substantially improved to a level of a commercial SC source based on a conventional mode-locked laser oscillator if it operates in the Raman-extended regime. In addition, if the NLP source operates at higher power and/or at repetition rate, the RIN can further be improved [147].

8.4 Conclusions

In this Chapter I have presented in detail the design and characterization of a linearly polarized ultra-broadband fiber laser source via exploiting the birefringence and nonlinearity of the fiber in a ring cavity configuration. I showed that not only the adjustment of the pump power but also the laser cavity finesse affects the pulse width of the envelope of the NLPs, where the latter has a bigger impact in the optical bandwidth of the laser. The developed laser could operate in two different regimes, the SPM-dominant regime and the Raman-extended regime, demonstrating with the latter a record bandwidth of 135 nm. The RIN measurement of the NLP source showed that for frequencies > 1kHz the RIN level is comparable to that of a commercial SC source and at low frequencies it shows slightly higher noise levels. However, there is still room for improvement in terms of the RIN if the NLP source is re-configured to operate at higher power and/or at repetition rate [148]. The results obtained here show that simple and compact NLP

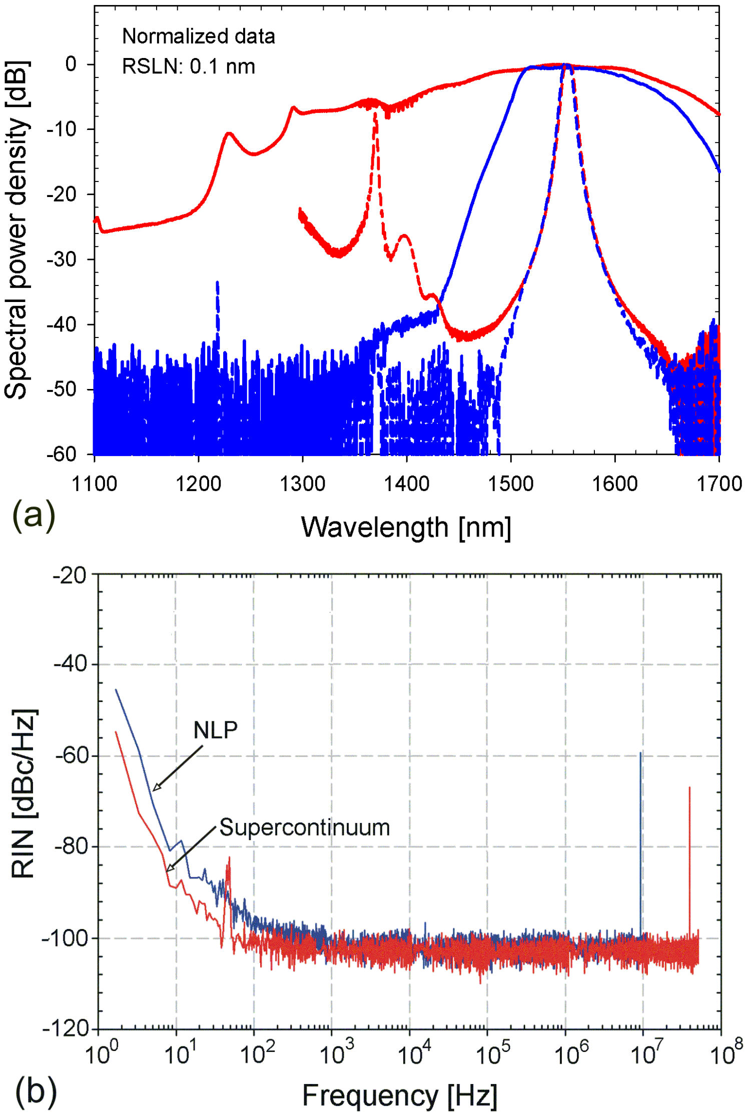

FIGURE 8.6: (a) Optical spectra before (solid traces) and after (short dashed traces) the 12 nm bandpass filter for the NLPs source (blue traces)and supercontinuum source(red trace). (b) RF noise spectra of the filtered signals of the sources mentioned previously

sources operating in the Raman-extended regime can be cost-effective sources for many optical systems that require broadband spectra with intermediate noise characteristics.

Chapter 9

Conclusions

The work presented in this thesis comprises three different research topics: 1) design of self-starting tunable-wavelength picosecond sources using Er^{3+}-doped fibre based technology, 2) amplification of picosecond pulses in LMA fibres, and 3) design of a compact broadband source using Er^{3+} fibre based technology. In Chapter 4 and 5, I described the development of an all-fiberized wavelength-tunable picosecond laser source using the frequency-shifted feedback technique to mode-lock the laser source (Chapter 4). In addition, I performed numerical simulations to understand the dynamics of the laser source (Chapter 5). Next, in Chapter 6 and 7 I described the development of a wavelength-tunable picosecond laser source using a SESAM to mode-lock the laser source (Chapter 6), and a direct amplification system to produce multi-kW peak power pulses with medium average power. Finally, in Chapter 8 I described the development of a compact all-fiberized broadband source which combines Er^{3+} fibre based technology and a HNLF to generate Raman gain. In this Chapter I summarize the work and results presented in this thesis.

Mode-locked laser based on frequency-shifted feedback technique

The development of a tunable-wavelength picosecond sources using a frequency-shifted feedback technique to mode-lock the laser source was presented. Empirical studies were carried out to understand the performance and limitations of the laser source. Results showed that an environmentally stable mode-locked regime was achieved by combining the FSF technique with a NLPE technique provided by a polarizer located between a pair of polarization controllers. For this configuration, the FSFL generated environmentally stable asymmetric picosecond pulses ($\sim$ 40 ps). The stability of the laser source allowed me to carry out different experiments to further characterize the asymmetry of the pulse spectra and pulse intensity as functions of different parameters of the laser cavity (filter bandwidth, frequency shift, and coupling ratio). The results presented here provide novel insights in the behaviour of FSFLs that were not previously addressed in the literature. The results summarized in Chapter 4 showed that for configurations with broad intracavity filter bandwidths the shape of the spectrum tends to split and form a *hump* on the longer (shorter) wavelength side due to the downshift (upshift) frequency mechanism of the AOM. It is also shown that the *hump* formed on the longer (shorter) wavelength side of the spectrum is responsible for the strong asymmetry on the trailing (leading) edge of the pulse in the time domain. Interaction of polarization dependent losses, nonlinear polarization rotation, and frequency shifts lead to adjustments of the pulse shape and pulse width. Therefore, shorter pulses can be achieved for higher frequency shifts and coupling power ratios close to unity. Broader filter bandwidths can also lead to pulse shortening; however it can also lead to multi-wavelength behaviour. Experimental results also showed that for narrow filter bandwidths the pulse spectrum does not split and the side of the spectrum where the spectral components are constantly shifted can be amplified to a level close to the spectral maxima. However, amplification of the far end of the spectrum depends on the frequency-dependent gain/losses of the cavity and the amount of frequency shift applied in the cavity. Furthermore, these results show the possibility to generate multi-functional stable sources by choosing the appropriate parameters in the cavity, for example, mode-locked multi-wavelength sources by means of a Fabry-P*é*rot filter, or use of the benefits of the AOM to amplitude modulate the cavity and generate Q-switched mode-locked laser.

Numerical simulation presented in Chapter 5 showed novel results in terms of pulse formation and spectral asymmetry for FSF lasers for different cavity parameters. For specific parameters of the laser cavity, stable pulses circulating at the fundamental repetition rate of the cavity could be formed. In this mode-locked regime, we also showed that for broad filter bandwidths, the increment in SPM leads to a split of the main pulse spectrum forming a *hump* on the wavelength side where the pulse spectral components are being constantly shifted by the frequency shifter mechanism in the cavity. These results corroborate the spectral shape of the pulses obtained experimentally. As a consequence of the *hump* formation, the spectral maximum of the pulse shifts in the opposite direction of the frequency shift mechanism. In the time domain, pulse asymmetry is strongly related to the *hump* formation on the pulse spectrum. This work can help to understand a few of the complex interactions effects happening in these lasers and that have not been clarified in the literature so far.

Mode-locked lasers based on a semiconductor saturable absorber mirror

Chapter 6 shows the results of a hybrid-mode-locking configuration operating in the 1.5 μm region. Self-starting mode-locking behaviour in all three cavities is achieved by enhancing NLPE and by incorporation of a commercial SESAM. The proposed sigma cavity configuration works in a fundamental mode-locked regime with and without optical filter for pump powers as low as $\leq$ 23 mW. The laser can deliver (without an optical filter) femtosecond pulses ($\leq$ 380 fs) with a maximum average output power of $\sim$ 1.9 mW, at repetition rates of $\sim$ 13 MHz ($E_p \sim$ 105 pJ). Incorporation of an optical filter in the cavity allows for picosecond pulse ($\leq$ 12 ps) generation with maximum average powers of $P_{pump} \sim 1$ mW, at repetition rates of $\sim$ 13 MHz, corresponding to pulse energies $E_p \leq 102$ pJ. The robust mode-locking stability of the laser cavity allows a wavelength (1533 nm to 1558 nm) and bandwidth (7 nm to 1.3 nm) tuning, making the laser a versatile tool for different applications (seeding of Erbium amplifiers or highly non-linear fibres, second harmonic generation, medical applications, etc).

A comparison between the lasers presented in this Chapter and the FSF laser described in Chapter 4 shows a better performance in terms of noise (e.g. see table 6.2), and stability for the former ones. Mode-locked lasers with SESAM showed more resilience to environmental fluctuations (e.g. vibrations or changes in temperature), although both kinds of laser could remain mode-locked for hours. Another advantage observed with the lasers using SESAM is the lack of hysteresis present in FSF lasers to achieve self-starting fundamental mode-locking behaviour (i.e. there is no need to pump at high powers to start the mode-locking mechanism in the cavity).

Amplification of a picosecond bandwidth-tunable laser source

Two different MOPA systems are proposed for amplification of picosecond pulses at different wavelengths. The first configuration comprises a LMA cladding-pumping Er^{3+}/ Yb^{3+} co-doped fibre amplifier which delivered pulses with peak powers and pulse energies of $\sim$ 5.7 kW and 74 nJ, respectively. Higher peak powers are limited by the onset of pulse-breaking. The second configuration comprised a LMA Yb^{3+}-free Er^{3+}-doped fibre, which delivered pulses with peak powers and pulse energies of $\sim$ 11 kW and 106 nJ, respectively. Higher peak powers could be achieved but were limited by pump power at longer wavelengths, and by ASE at shorter wavelength. The novelty of the second configuration is that it includes a hybrid pumping configuration to tackle the low cladding absorption of the Er^{3+}-doped fibre, allowing me to reduce the active fibre length. Thus, it was possible to delay the onset of pulse-breaking, due to excessive nonlinearities. Although the configuration was designed to ensure preferential gain for the fundamental mode by exciting it through the taper section of the fibre, cladding pumping deteriorates the quality beam factor by exciting higher order modes in the fibre. A M^2 factor of 2.4 was achieved at a maximum output power.

Broadband sources for optical coherence tomography

Development and detailed characterization of a lineraly polarized ultra-broadband fibre laser source based on Er^{3+} technology was presented. Broadband spectrum was generated by exploiting the birefringence and nonlinearity of the fiber in a ring cavity configuration. The developed laser could operate in two different regimes: 1) SPM-dominant regime, and 2) Raman-extended regime. Regarding the former, pulse energy and width were readily reconfigurable from 0.7 nJ to 1.1 nJ and from 90 ps to 220 ps, respectively, via controlling the cavity finesse and/or pumping power. Regarding the former, the soure could generate a record bandwidth of 135 nm with 6.9 mW of output power. In addition, the RIN of the source was measured and compared with that of a commercial SC source. Results showed a RIN of -97 dB/Hz at low frequencies up to 100 kHz and -104 dB/Hz at high frequencies up to 5 MHz. In comparison with a commercial SC source, the NLP source has similar noise characteristics except for slightly higher noise levels at low frequencies ($<$ 1 kHz).

Chapter 10

Future Work

In this final Chapter I present possible future directions of research and investigations.

The work carried out in Chapter 4 and 5 provides novel insights into the behaviour of FSFLs that were not previously addressed in the literature. Nevertheless there are still several features of these lasers that are not entirely understood, for example, the mechanisms in the laser cavity that force pulses to propagate in clusters at the fundamental repetition rate when high pump powers are applied. The experimental results, presented in this thesis, showed that separation between pulses is related to the optical filter bandwidth in the cavity. Therefore it would be useful to carry out an empirical research with a bandwidth-tunable filter like the one used in Chapter 6 (Alnair filter) [1]. The experimental results could be useful to determine more precisely the relation between the filter bandwidth, the pulse width and the space between the cluster pulses. Regarding the numerical simulations, the model presented in this thesis does not take into account the polarization state in the cavity. Therefore, future improvements to this model should consider the polarization state of the optical signal to account for the NLPE effect in the experimental cavity.

Regarding the work presented in Chapter 6, the laser configuration used a SESAM mounted on a translation stage which makes the configuration less attractive in terms of compactness and alignment-free. Therefore, a future direction for this research could be the replacement of the "bulk" SESAM by a more attractive one based on a saturable absorber (in transmission mode) mounted on the end face of a single-mode fibre. This will allow for a more compact all-fiberized cavity. In addition, the net dispersion of the cavity was limited by the amount of fibre used in the two manual polarization controllers. Therefore, it was not possible to operate this laser configuration with a net positive dispersion $\beta_2 > 0$ or close to zero. The net positive dispersion will force the

---

[1] At the time these experiments were carried out the Alnair filter was not available.

laser to operate in a stretched-pulse regime, generating pulses with higher energy and broader bandwidth [149].

Results presented in Chapter 7 regarding direct amplification of picosecond pulses in LMA fibres, were mainly limited in terms of efficiency and power scaling by the fibre designs. For the case of the $\mathrm{Er}^{3+}/\mathrm{Yb}^{3+}$ co-doped fibre with core diameter 27 μm, pulse break-up was observed for pulses with peak powers of $P_p \sim 9$ kW after amplification. In this case, the core size of the $\mathrm{Er}^{3+}/\mathrm{Yb}^{3+}$ co-doped fibre was too small. For the Er^{3+}-doped fibre, pulse amplification was only limited by the available pump power. Nevertheless, the low cladding absorption of the fibre also imposes a limit to the minimum length that can be used in the amplifier. Core pumping the fibre with a more powerful Raman laser can improve not only the laser efficiency but also the beam quality at the output of the amplifier. High peak powers with relatively high average output power suggest that this compact source can be suitable for applications such as second-harmonic generation. This technique can be a good option to generate average power wavelength-tunable picosecond pulses in a wavelength region ~ 780 nm. Although second-harmonic generation is a well-established technique in “bulk” solid-state lasers to generate frequency-double sources, in the area of fibre lasers it is still not a consolidated area. Therefore, experimental work can be carried out on this area. Nevertheless, improvements to the laser source should be done in terms of beam quality. Recent publications [150] have shown that conversion efficiency of the second-harmonic generation (SHG) decrease with rising beam propagation factor M^2. In fact, from [150] it can be calculated that for a $M^2 \sim 2.4$ the SHG efficiency will drop by more than 50% compared with a diffraction-limited beam. In addition, the spectral width of the pulse should remain relatively narrow in order to fit into the spectral acceptance bandwidth of a nonlinear crystal.

Broadband sources are quite useful for applications such as metrology, optical component testing or medical imaging such as OCT. Up to date, most work [151] have focused on developing supercontinuum generation sources with the help of MOPAs and nonlinear optical fibres. These systems add complexity, cost and size to the source. In this situation, the broadband source presented in Chapter 8 can be a good candidate as a compact and cost-effective source for OCT. Nevertheless, a clear drawback of the NLP source at this stage is its low output power ($P_{out} \sim 6.9$ mW), which will limit its application to slow acquisition [151]. Therefore, future work on this laser source should be focused on increasing the output power. A cladding-pumping configuration of the NLP source presented in Chapter 8 may provide a way for power-scaling.

Appendix A

Characterization of the noise in mode-locked lasers

This appendix explains the theoretical framework for the characterization of amplitude noise and time jitter in mode-locked lasers based on the work of Von der Linde [9]. The noise contributions calculated in this appendix correspond to the output signal of the wavelength-tunable mode-locked fibre laser described in Section 6.3.2. Although these are the only calculations presented here, the same procedure was carried out to calculate the noise contributions of the different lasers described in Chapter 4 and 6.

The output signal of a mode-locked laser presents small random fluctuations in amplitude and repetition time. In the frequency domain, these random fluctuations contribute in different ways to the formation of the power spectrum of the signal. Therefore, with a proper characterization of the intensity power spectrum it is possible to identify these fluctuations and quantify them through ordinary measurements in an RF spectrum analyser.

The signal of a noisy cw mode-locked laser can be written as:

$$F(t) \;=\; F_0(t) \;+\; F_0(t)A(t) + \dot{F}_0(t)TJ(t) \tag{A.1}$$

Where $F_0(t)$ represents a perfectly (noise-free) mode-locked laser signal (e.g. $F_0(t) = \sum_\mu f(t+\mu T)$ with $f(t)$ being the temporal profile of the individual pulses in the signal, and T the pulse repetition time), $F_0(t)A(t)$ represents amplitude fluctuations characterized by a random function A(t), and $\dot{F}_0(t)T\,J(t)$ represents small random variations of the pulse repetition time.

The power spectrum of A.1 can be obtained by applying the Fourier transform of the intensity autocorrelation function of $F(t)$:

$$P_F(\omega) = (2\pi/T)^2 \left|\tilde{f}(\omega)\right|^2 \sum_{\mu} \left[\delta(\omega - 2\pi\mu/T) + P_A(\omega - 2\pi\mu/T) + (2\pi\mu)^2\, P_J(\omega - 2\pi\mu/T)\right], \tag{A.2}$$

where $P_A(\omega)$ and $P_J(\omega)$ are the power spectra of $A(t)$ and $J(t)$, respectively, $\tilde{f}(\omega)$ is the Fourier transform of the slowly temporal intensity profile of the individual free-noise pulses, and μ is an integer from minus to plus infinity. Fig. A.1 depicts the rapidly varying terms defined by the sum in Eq. A.2. The terms comprising the sum are formed by a series of frequency bands centred at $(\omega - 2\pi\mu/T)$ with a constant spacing $2\pi/T$. Each band has a contribution from the ideal pulses (δ-function) and contributions from the amplitude noise $P_A(\omega)$ and the temporal jitter $P_J(\omega)$. As shown in Fig. A.1, the μ^2 dependence of the temporal jitter on Eq. A.2 allows one to distinguish the two noise contributions (i.e. components centred around $\omega = 0$ are dominated by amplitude noise, while higher order components are dominated by timing jitter).

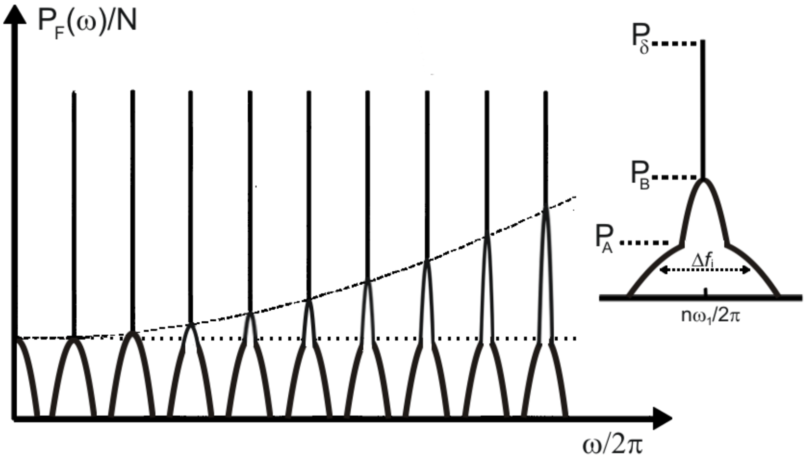

FIGURE A.1: Power spectrum $P_F(\omega)$ of a train of pulses with random fluctuations in amplitude and repetition time. The dotted line indicates the maxima of the amplitude noise frequency band, while the dashed line represents the maxima of the temporal jitter frequency band. Inset shows an sketch of the structure of an arbitrary frequency component of $P_F(\omega)$. Figure and inset taken and modified from [9].

For stochastic processes, the amount of random fluctuations is characterized by the root-mean-square (rms) deviation of the noisy signal (e.g. the area of the noise spectrum). Therefore, for amplitude fluctuations, the rms deviation ΔE_p of the average pulse energy E_p, is calculated as

$$\Delta E_p/E_p = \int_{-\infty}^{+\infty} P_A(\omega) d\omega, \tag{A.3}$$

and for temporal fluctuations, the rms deviation Δt of the average pulse repetition time T is given by

$$\Delta t/T \;=\; \int_{-\infty}^{+\infty} P_J(\omega) d\omega \tag{A.4}$$

In a practical experiment, the amplitude noise and time jitter contributions to the laser signal can be extracted from its RF spectrum by measuring the power densities (P_δ, P_B, P_A, and the frequency width Δf_i of the noise bands (see inset of Fig. A.1). P_δ represents the maximum power of the spikes in a specific frequency band (i.e. the δ-function defined in A.2), P_B is the peak power of the fully resolved noise band (timing jitter contribution), and P_A is the peak power of the broad noise band (amplitude noise contribution). Taking into account these values, and from Eq. A.2 it is possible to calculate the power ratio of the n-th order spectral side band for high frequency (P_A) and low frequency (P_B) contributions as:

$$(P_A/P_\delta)_n \;=\; 2\pi\Delta f_{res} \left[P_A(0) + (2\pi n)^2\, \acute{P}_J(0)\right], \tag{A.5}$$

$$(P_B/P_\delta)_n \;=\; 2\pi\Delta f_{res} \left[P_A(0) + (2\pi n)^2\, P_J(0)\right], \tag{A.6}$$

where Δf_{res} is the resolution bandwidth given by the spectrum analyser.

Using Eq. A.3, and A.5 it is possible to write an expression for energy fluctuations at the fundamental frequency component ($n = 0$) as:

$$\Delta E_p/E_p \;=\; \left[(P_A/P_\delta)_{n=0} \Delta f_A/\Delta f_{res}\right]^{1/2}, \tag{A.7}$$

For the case of the RF-spectrum of the wavelength-tunable mode-locked fibre laser shown in 6.4 (a), I obtained a value of $P_\delta =$ -39.16 dBm and $P_A =$ -110.21 dBm, with a frequency width $\Delta f_A = 83$ kHz and a resolution frequency $\Delta f_{res} = 300$ Hz . The frequency band noise includes the base of the spectrum at the fundamental frequency and the noise bands located at -125 kHz and 125 kHz. Using Eq. A.7 I calculated a value $\Delta E_p/E_p =$ 0.47 %.

The low amplitude noise obtained in this laser allows neglecting it while calculating the timing jitter from the high-order noise components. Thus, using A.4, and A.6 the low frequency timing jitter contribution is given as

$$\Delta t/T \;=\; (2\pi n)^{-1} \left[(P_B/P_\delta)_n \Delta f_J/\Delta f_{res}\right]^{1/2}, \tag{A.8}$$

The inset in 6.4 (b) shows the RF spectrum of the 10^{th} harmonic. From this figure values of P_δ = -39 dBm, P_B = -101 dBm, and $\Delta f_J = 0.41$ kHz with a frequency resolution $\Delta f_{res} = 10$ Hz were measured. Using Eq. A.8 I calculated a value $\Delta t \cdot T = 6.09$ ps, with $T = (13.28 \text{ MHz})^{-1}$.

Appendix B

Equipment data sheets

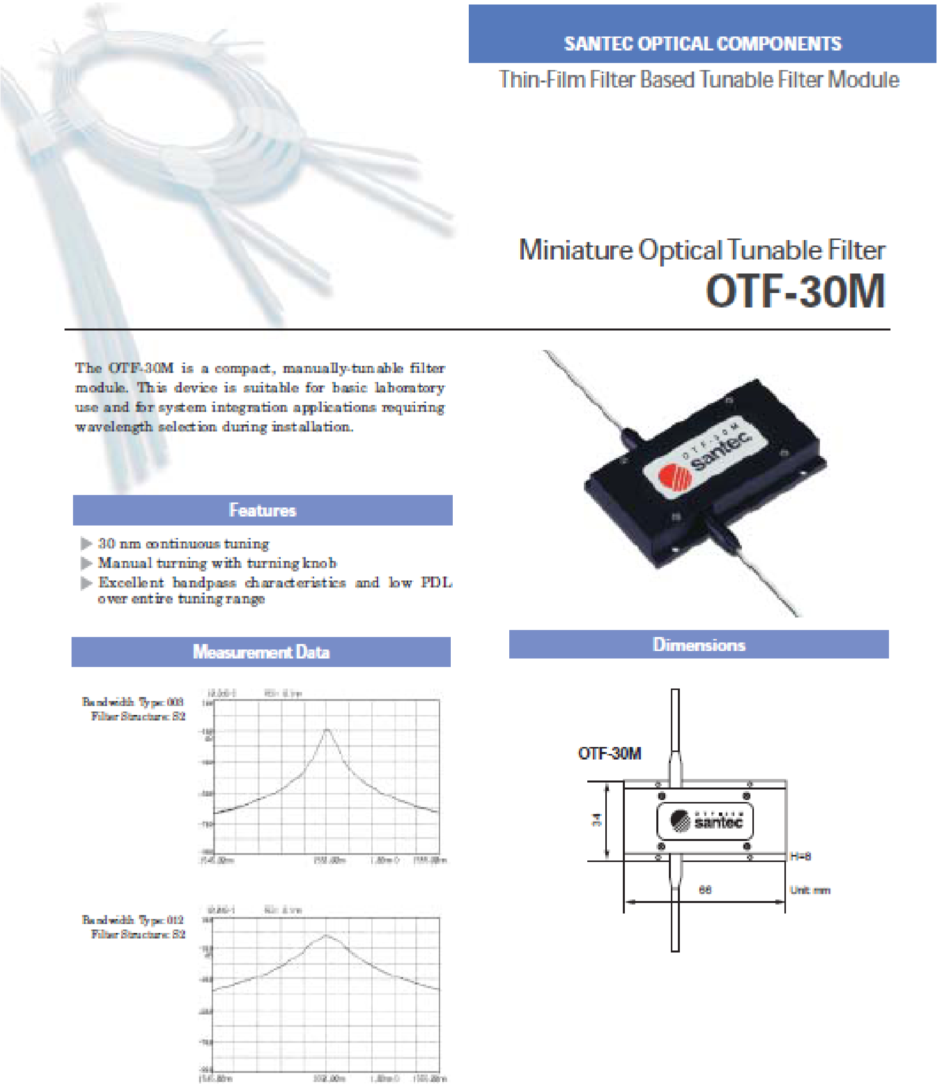

SANTEC OPTICAL COMPONENTS

Thin-Film Filter Based Tunable Filter Module

Miniature Optical Tunable Filter

OTF-30M

The OTF-30M is a compact, manually-tunable filter module. This device is suitable for basic laboratory use and for system integration applications requiring wavelength selection during installation.

Features

- 30 nm continuous tuning
- Manual turning with turning knob
- Excellent bandpass characteristics and low PDL over entire tuning range

Measurement Data

Bandwidth Type: 003
Filter Structure: S2

Bandwidth Type: 012
Filter Structure: S2

Dimensions

FIGURE B.1: **Specifications for bandwidth-variable tunable filter BVF-200CL**

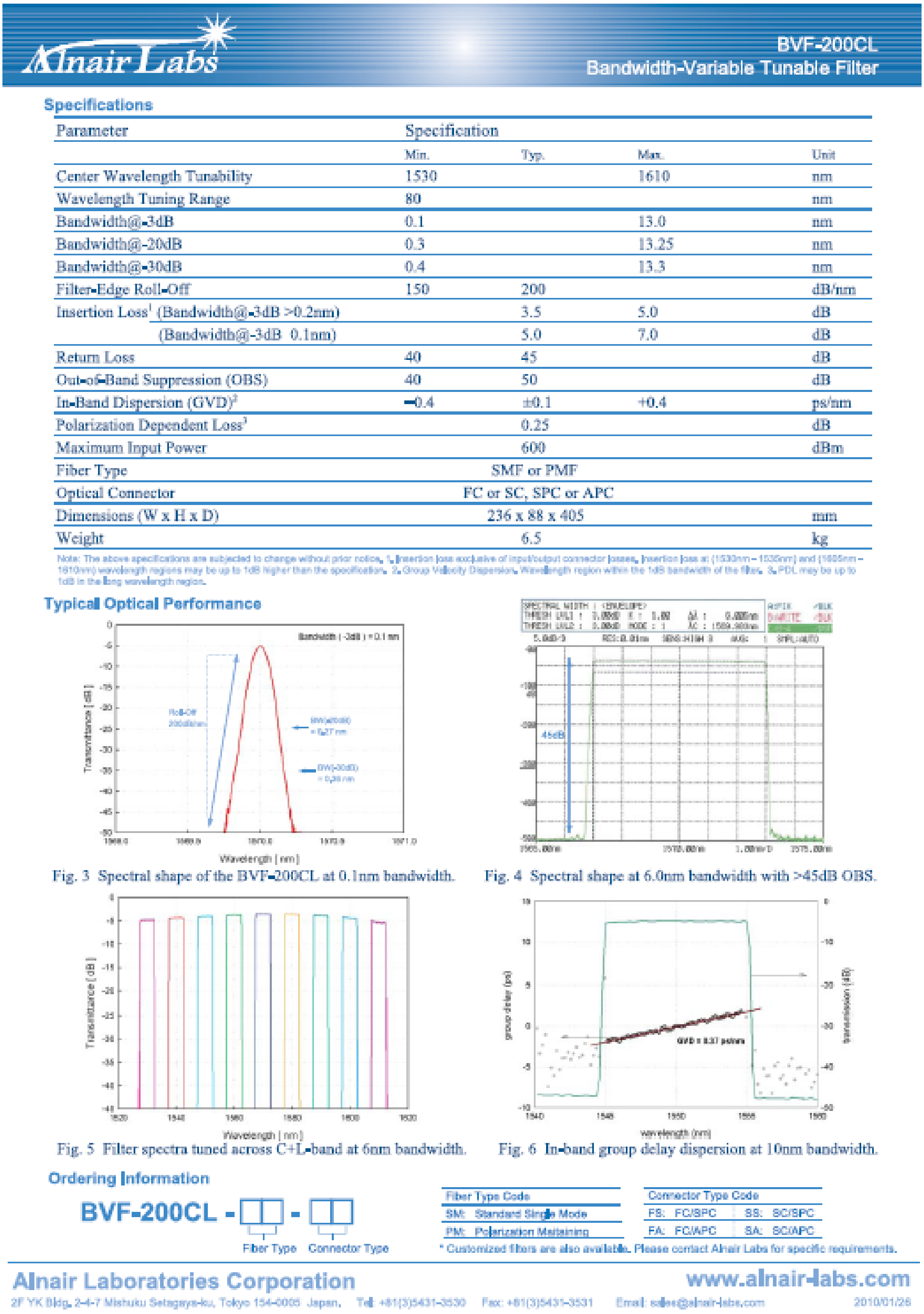

BVF-200CL
Bandwidth-Variable Tunable Filter

Specifications

Parameter	Specification			
	Min.	Typ.	Max.	Unit
Center Wavelength Tunability	1530		1610	nm
Wavelength Tuning Range	80			nm
Bandwidth@-3dB	0.1		13.0	nm
Bandwidth@-20dB	0.3		13.25	nm
Bandwidth@-30dB	0.4		13.3	nm
Filter-Edge Roll-Off	150	200		dB/nm
Insertion Loss[1] (Bandwidth@-3dB >0.2nm)		3.5	5.0	dB
(Bandwidth@-3dB 0.1nm)		5.0	7.0	dB
Return Loss	40	45		dB
Out-of-Band Suppression (OBS)	40	50		dB
In-Band Dispersion (GVD)[2]	−0.4	±0.1	+0.4	ps/nm
Polarization Dependent Loss[3]		0.25		dB
Maximum Input Power		600		dBm
Fiber Type		SMF or PMF		
Optical Connector		FC or SC, SPC or APC		
Dimensions (W x H x D)		236 x 88 x 405		mm
Weight		6.5		kg

Note: The above specifications are subjected to change without prior notice. 1. Insertion loss exclusive of input/output connector losses. Insertion loss at (1530nm – 1535nm) and (1605nm – 1610nm) wavelength regions may be up to 1dB higher than the specification. 2. Group Velocity Dispersion. Wavelength region within the 1dB bandwidth of the filter. 3. PDL may be up to 1dB in the long wavelength region.

Typical Optical Performance

Fig. 3 Spectral shape of the BVF-200CL at 0.1nm bandwidth.

Fig. 4 Spectral shape at 6.0nm bandwidth with >45dB OBS.

Fig. 5 Filter spectra tuned across C+L-band at 6nm bandwidth.

Fig. 6 In-band group delay dispersion at 10nm bandwidth.

Ordering Information

BVF-200CL - ☐☐ - ☐☐
Fiber Type Connector Type

Fiber Type Code
SM: Standard Single Mode
PM: Polarization Maintaining

Connector Type Code	
FS: FC/SPC	SS: SC/SPC
FA: FC/APC	SA: SC/APC

* Customized filters are also available. Please contact Alnair Labs for specific requirements.

Alnair Laboratories Corporation **www.alnair-labs.com**
2F YK Bldg. 2-4-7 Mishuku Setagaya-ku, Tokyo 154-0005 Japan. Tel: +81(3)5431-3530 Fax: +81(3)5431-3531 Email: sales@alnair-labs.com 2010/01/26

SAM™ Data Sheet SAM-1550-23-2ps-x, λ = 1550 nm

Laser wavelength	λ = 1550 nm
High reflection band	λ = 1460 .. 1600 nm
Absorbance	A_0 = 23 %
Modulation depth	ΔR = 14 %
Non-saturable loss	A_{ns} = 9 %
Saturation fluence	Φ_{sat} = 25 µJ/cm^2
Relaxation time constant	τ ~ 2 ps
Damage threshold	500 MW/cm^2
Chip area	4mm x 4mm; other dimensions on request
Chip thickness	400 µm; optional: 150 µm on request
Protection	the SAM is protected with a dielectric front layer

Mounting option **x** denotes the type of mounting as follows:

x = 0	unmounted
x = 12.7 g	glued on a gold plated Cu-cylinder with 12.7 mm ∅
x = 25.4 g	glued on a gold plated Cu-cylinder with 25.4 mm ∅
x = 12.7 s	soldered on a gold plated Cu-cylinder with 12.7 mm ∅
x = 25.4 s	soldered on a gold plated Cu-cylinder with 25.4 mm ∅
x = FC	mounted on a 1 m monomode fiber cable with FC connector

Low intensity spectral reflectance

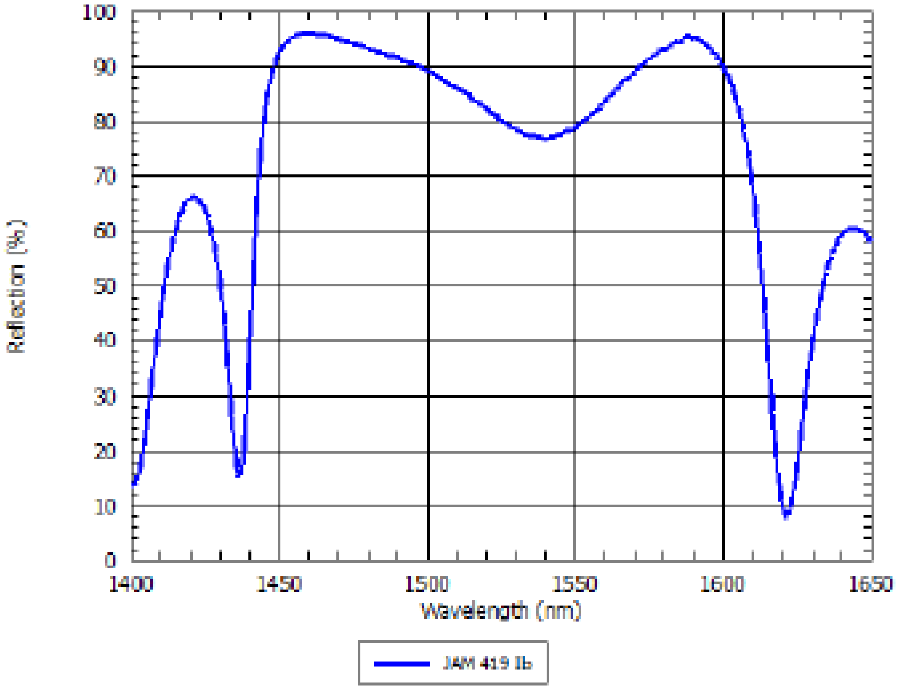

BATOP GmbH
Wildenbruchstraße 15
D-07745 Jena
Germany

Tel: +49 3641 634009 - 0
Fax: +49 3641 634009 - 20
E-mail: info@ batop.de

Deutsche Bank Jena
Bank Code: 82070024
Account No: 3922655
IBAN: DE49 8207 0024 0392 2655 00

VAT Reg.No: DE813698804
Tax Acc. No: 162/106/01639
Local Court Jena HRB 112769

BATOP
optoelectronics

Relaxation time

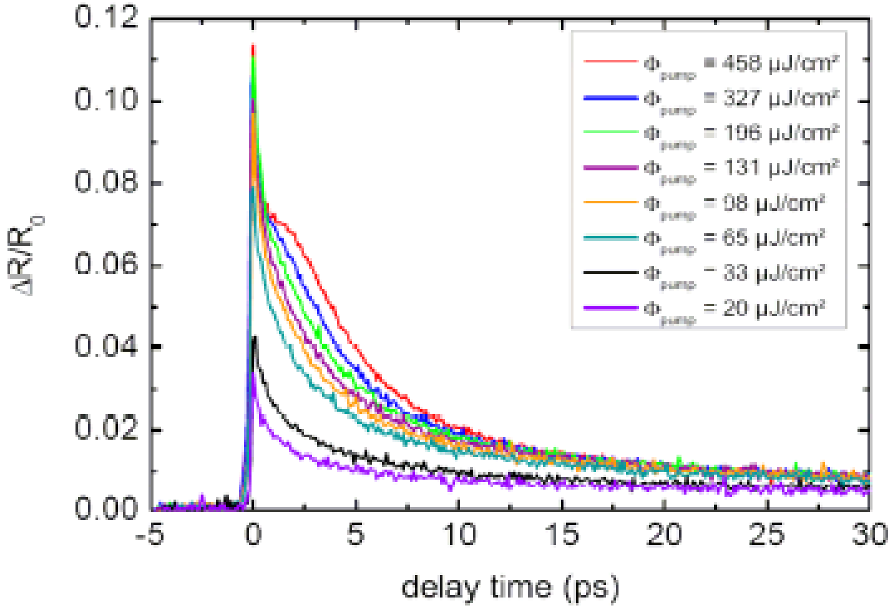

The pump-probe measurements has been carried out by Florian Adler, Physics, University of Konstanz, Germany

Saturation

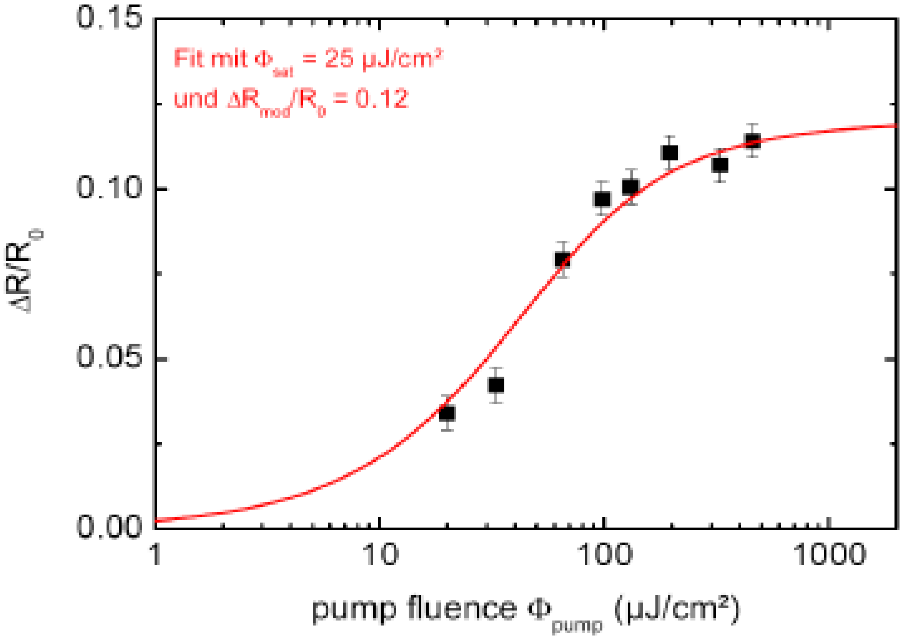

The pump-probe measurements has been carried out by Florian Adler, Physics, University of Konstanz, Germany

BATOP GmbH
Wildenbruchstraße 15
D-07745 Jena
Germany

Tel: +49 3641 634009 - 0
Fax: +49 3641 634009 - 20
E-mail: info@batop.de

Deutsche Bank Jena
Bank Code: 82070024
Account No: 3922655
IBAN: DE49 8207 0024 0392 2655 00

VAT Reg. No: DE 813698804
Tax Acc. No: 161/106/02514
Local Court Jena HRB 112769

Appendix C

List of publications

This appendix contains the list of published work during my research stay at the ORC

Journal publications

1. L.A. Vazquez-Zuniga, S. Chung, and Y. Jeong, "Thermal Characteristics of an Ytterbium-Doped Fiber Amplifier Operating at 1060 and 1080 nm", Japanese Journal of Applied Physics, 2010. 49(2).
2. L.A. Vazquez-Zuniga, and Y. Jeong, "Super-Broadband Noise-Like Pulse Erbium-Doped Fiber Ring Laser with a Highly Nonlinear Fiber for Raman Gain Enhancement" **Submitted to IEEE Photonics Technology Letters**
3. L.A. Vazquez-Zuniga, and Y. Jeong, "On the study of a mode-locked Er-doped frequency-shifted-feedback fiber laser. Part 1: Numerical simulation results" **To be submitted**
4. L.A. Vazquez-Zuniga, and Y. Jeong, "On the study of a mode-locked Er-doped frequency-shifted-feedback fiber laser. Part 2: Experimental results" **To be submitted**

Conferences

1. L.A. Vazquez-Zuniga, and Y. Jeong, "Spectral and temporal behavior of a mode-locked Er-doped frequency shifted feedback fiber laser", 2011 16th Opto-Electronics and Communications Conference (OECC 2011), 2011.
2. L.A. Vazquez-Zuniga, H. Jeong, and Y. Jeong, "Linearly Polarized, 135-nm Bandwidth Pulse Generation in an Erbium-Doped Fiber Ring Laser", 2010 Conference on Lasers and Electro-Optics (CLEO), 2010.

3. Y. Jeong, C. A. Codemard, J. Ji,L. A. Vazquez-Zuniga, G. van der Westhuizen, S. Yoo, A. J. Boyland, M. Petrovich, F. Poletti, G. M. Ponzo, J. K. Sahu, J. Nilsson, D. J. Richardson, D. N. Payne, "Novel fibre technology for high-power lasers", 2010 Asia Communications and Photonics Conference and Exhibition (ACP 2010), 2010.

4. L.A. Vazquez-Zuniga, S. Chung, and Y. Jeong, "Temperature dependence of a high-power ytterbium-doped fiber amplifier operating at 1060 nm and 1080 nm", 2009 14th OptoElectronics and Communications Conference (OECC), 2009.

5. J. Nilsson, Y. Jeong, C. A. Codemard, C. Farrell, L.A. Vasquez J. Ji, M. S. Z. Abidin, G. van der Westhuizen, S. Yoo, J.K. Sahu. High power fibre lasers: Exploitation of unique properties. Lasers and Electro-Optics 2009 and the European Quantum Electronics Conference. CLEO Europe - EQEC 2009.

6. L. A. Vazquez-Zuniga, P. Petropoulos, D. J. Richardson, "Design of a fiber Bragg grating for decoding DPSK signals", e-PhotonONe+/COST 291 Brest 16-20 Jul 2007.

Bibliography

[1] M. J. Digonnet, *Rare-earth-doped fiber lasers and amplifiers.* New York: Plenum Press, 4th ed., —1998—.

[2] D. J. Richardson, J. Nilsson, and W. A. Clarkson, “High power fiber lasers: current status and future perspectives,” *Journal of the Optical Society of America B-Optical Physics*, vol. 27, no. 11, pp. B63–B92, 2010.

[3] C. Codemard, *High-power cladding-pumped Raman and Erbium-Ytterbium doped fibre sources.* PhD thesis, University of Southampton, UK, 2007.

[4] G. P. Agrawal, “Nonlinear fiber optics: its history and recent progress invited,” *Journal of the Optical Society of America B-Optical Physics*, vol. 28, no. 12, pp. A1–A10, 2011.

[5] G. R. Agrawal, *Applications of Nonlinear Fiber Optics.* San Diego: Academic, —2001—.

[6] L. E. Nelson, D. J. Jones, K. Tamura, H. A. Haus, and E. P. Ippen, “Ultrashort-pulse fiber ring lasers,” *Applied Physics B: Lasers and Optics*, vol. 65, no. 2, pp. 277–294, 1997.

[7] E. R. Thoen, E. M. Koontz, M. Joschko, P. Langlois, T. R. Schibli, F. X. Kartner, E. P. Ippen, and L. A. Kolodziejski, “Two-photon absorption in semiconductor saturable absorber mirrors,” *Applied Physics Letters*, vol. 74, no. 26, pp. 3927–3929, 1999.

[8] H. Sabert and E. Brinkmeyer, “Pulse generation in fiber lasers with frequency shifted feedback,” *Journal of Lightwave Technology*, vol. 12, no. 8, pp. 1360–1368, 1994.

[9] D. von der Linde, “Characterization of the noise in continuously operating mode-locked lasers,” *Applied Physics B-Photophysics and Laser Chemistry*, vol. 39, no. 4, pp. 201–217, 1986.

[10] Y. Jeong, J. K. Sahu, D. N. Payne, and J. Nilsson, “Ytterbium-doped large-core fibre laser with 1 kW of continuous-wave output power,” *Electronics Letters*, vol. 40, no. 8, pp. 470–472, 2004.

[11] J. Limpert, F. Röser, S. Klingebiel, T. Schreiber, C. Wirth, T. Peschel, R. Eberhardt, and A. Tünnermann, "The rising power of fiber lasers and amplifiers," *IEEE Journal of Selected Topics in Quantum Electronics*, vol. 13, no. 3, pp. 537–545, 2007.

[12] R. Paschotta, J. Nilsson, A. C. Tropper, and D. C. Hanna, "Ytterbium-doped fiber amplifiers," *IEEE Journal of Quantum Electronics*, vol. 33, no. 7, pp. 1049–1056, 1997.

[13] J. K. Sahu, Y. Jeong, D. J. Richardson, and J. Nilsson, "A 103-W Erbium-Ytterbium co-doped large-core fiber laser," *Optics Communications*, vol. 227, no. 1-3, pp. 159–163, 2003.

[14] C. Alegria, Y. Jeong, C. Codemard, J. K. Sahu, J. A. Alvarez-Chavez, L. Fu, M. Ibsen, and J. Nilsson, "83-W single-frequency narrow-linewidth MOPA using large-core Erbium-Ytterbium co-doped fiber," *IEEE Photonics Technology Letters*, vol. 16, no. 8, pp. 1825–1827, 2004.

[15] Y. Jeong, S. Yoo, C. A. Codemard, J. Nilsson, J. K. Sahu, D. N. Payne, R. Horley, P. W. Turner, L. Hickey, A. Harker, M. Lovelady, and A. Piper, "Erbium:Ytterbium codoped large-core fiber laser with 297-W continuous-wave output power," *IEEE Journal of Selected Topics in Quantum Electronics*, vol. 13, no. 3, pp. 573–579, 2007.

[16] J. Nilsson, S. U. Alam, J. A. Alvarez-Chavez, P. W. Turner, W. A. Clarkson, and A. B. Grudinin, "High-power and tunable operation of Erbium-Ytterbium co-doped cladding-pumped fiber lasers," *IEEE Journal of Quantum Electronics*, vol. 39, no. 8, pp. 987–994, 2003.

[17] J. C. Jasapara, M. J. Andrejco, A. DeSantolo, A. D. Yablon, Z. Varallyay, J. W. Nicholson, J. M. Fini, D. J. DiGiovanni, C. Headley, E. Monberg, and F. V. DiMarcello, "Diffraction-limited fundamental mode operation of core-pumped very-large-mode-area Er fiber amplifiers," *IEEE Journal of Selected Topics in Quantum Electronics*, vol. 15, no. 1, pp. 3–11, 2009.

[18] I. P. Webpage, "http://www.ipgphotonics.com," December 2011.

[19] J. Limpert, T. Schreiber, A. Liem, S. Nolte, H. Zellmer, and A. Tuennermann, "Megawatt peak power level fiber laser system based on compression in air-guiding photonic bandgap fiber," in *Advanced Solid-State Photonics*, p. MD1, Optical Society of America, 2004.

[20] E. Snitzer, "Optical maser action of Nd^{+3} in a barium crown glass," *Physical Review Letters*, vol. 7, no. 12, pp. 444–446, 1961.

[21] E. Snitzer, "Proposed fiber cavities for optical masers," *Journal of Applied Physics*, vol. 32, no. 1, p. 36, 1961.

[22] C. J. Koester and E. Snitzer, "Amplification in a fiber laser," *Appl. Opt.*, vol. 3, no. 10, pp. 1182–1186, 1964.

[23] J. Stone and C. A. Burrus, "Neodymium-doped silica lasers in end-pumped fiber geometry," *Applied Physics Letters*, vol. 23, no. 7, pp. 388–389, 1973.

[24] S. B. Poole, D. N. Payne, and M. E. Fermann, "Fabrication of low-loss optical fibers containing rare-earth ions," *Electronics Letters*, vol. 21, no. 17, pp. 737–738, 1985.

[25] R. J. Mears, L. Reekie, S. B. Poole, and D. N. Payne, "Neodymium-doped silica single-mode fiber lasers," *Electronics Letters*, vol. 21, no. 17, pp. 738–740, 1985.

[26] R. J. Mears, L. Reekie, I. M. Jauncey, and D. N. Payne, "Low-noise erbium-doped fiber amplifier operating at 1.54-μm," *Electronics Letters*, vol. 23, no. 19, pp. 1026–1028, 1987.

[27] Y. Jeong, J. K. Sahu, D. N. Payne, and J. Nilsson, "Ytterbium-doped large-core fiber laser with 1.36 kW continuous-wave output power," *Optics Express*, vol. 12, no. 25, pp. 6088–6092, 2004.

[28] E. Stiles, "New developments in IPG fiber laser technology," in *The Fifth International Workshop on Fiber Lasers*, September 30-October1 2009.

[29] S. D. Jackson, "The spectroscopic and energy transfer characteristics of the rare earth ions used for silicate glass fibre lasers operating in the shortwave infrared," *Laser & Photonics Reviews*, vol. 3, no. 5, pp. 466–482, 2009.

[30] D. C. Brown and H. J. Hoffman, "Thermal, stress, and thermo-optic effects in high average power double-clad silica fiber lasers," *IEEE Journal of Quantum Electronics*, vol. 37, no. 2, pp. 207–217, 2001.

[31] C. R. Giles and E. Desurvire, "Modeling Erbium-doped fiber amplifiers," *Journal of Lightwave Technology*, vol. 9, no. 2, pp. 271–283, 1991.

[32] J. D. Minelly, W. L. Barnes, R. I. Laming, P. R. Morkel, J. E. Townsend, S. G. Grubb, and D. N. Payne, "Diode-array pumping of Er^{3+}/Yb^{3+} co-doped fiber lasers and amplifiers," *IEEE Photonics Technology Letters*, vol. 5, no. 3, pp. 301–303, 1993.

[33] G. G. Vienne, J. E. Caplen, L. Dong, J. D. Minelly, J. Nilsson, and D. N. Payne, "Fabrication and characterization of Yb^{3+}:E r^{3+} phosphosilicate fibers for lasers," *Journal of Lightwave Technology*, vol. 16, no. 11, pp. 1990–2001, 1998.

[34] Y. Jeong, D. Lee, J. W. Lee, and K. Oh, "Fiber-optic color synthesizer," *Optics Letters*, vol. 31, no. 14, pp. 2112–2114, 2006.

[35] D. Young and C. Roychoudhuri, "Results and comparison of a cladding pumped fiber simulation using a decagon-shaped fiber," *Optics Express*, vol. 11, no. 7, pp. 830–837, 2003.

[36] P. Blixt, J. Nilsson, T. Carlnas, and B. Jaskorzynska, "Concentration-dependent upconversion in Er^{3+}-doped fiber amplifiers - experiments and modeling," *IEEE Photonics Technology Letters*, vol. 3, no. 11, pp. 996–998, 1991.

[37] E. Delevaque, T. Georges, M. Monerie, P. Lamouler, and J. F. Bayon, "Modeling of pair-induced quenching in erbium-doped silicate fibers," *IEEE Photonics Technology Letters*, vol. 5, no. 1, pp. 73–75, 1993.

[38] J. C. Jasapara, A. DeSantolo, J. W. Nicholson, A. D. Yablon, and Z. Varallyay, "Diffraction limited amplification of picosecond pulses in 1170 μm^2 effective area erbium fiber," *Optics Express*, vol. 16, no. 23, pp. 18869–18874, 2008.

[39] K. H. Yla-Jarkko, C. Codemard, J. Singleton, P. W. Turner, I. Godfrey, S. U. Alam, J. Nilsson, J. K. Sahu, and A. B. Grudinin, "Low-noise intelligent cladding-pumped L-band EDFA," *Photonics Technology Letters, IEEE*, vol. 15, no. 7, pp. 909–911, 2003.

[40] D. J. DiGiovanni and A. D. Yablon, "Cladding pumped optical fiber gain devices," *U.S. Patent No. 6,970,624 B2*, 2005.

[41] G. P. Agrawal, *Nonlinear fiber optics.* San Diego: Academic Press, 3rd ed., —2001—.

[42] M. E. Fermann and I. Hartl, "Ultrafast fiber laser technology," *IEEE Journal of Selected Topics in Quantum Electronics*, vol. 15, no. 1, pp. 191–206, 2009.

[43] F. W. Wise, A. Chong, and W. H. Renninger, "High-energy femtosecond fiber lasers based on pulse propagation at normal dispersion," *Laser & Photonics Reviews*, vol. 2, no. 1-2, pp. 58–73, 2008.

[44] A. E. Siegman, *Lasers.* Mill Valley, CA.: University Science Books, —1986—.

[45] K. Tamura, H. A. Haus, and E. P. Ippen, "Self-starting additive pulse mode-locked erbium fiber ring laser," *Electronics Letters*, vol. 28, no. 24, pp. 2226–2228, 1992.

[46] M. Hofer, M. E. Fermann, F. Haberl, M. H. Ober, and A. J. Schmidt, "Mode-locking with cross-phase and self-phase modulation," *Optics Letters*, vol. 16, no. 7, pp. 502–504, 1991.

[47] M. E. Fermann, M. Hofer, F. Haberl, A. J. Schmidt, and L. Turi, "Additive-pulse-compression mode-locking of a neodymium fiber laser," *Optics Letters*, vol. 16, no. 4, pp. 244–246, 1991.

[48] D. J. Richardson, R. I. Laming, D. N. Payne, M. W. Phillips, and V. J. Matsas, "320 fs soliton generation with passively mode-locked erbium fiber laser," *Electronics Letters*, vol. 27, no. 9, pp. 730–732, 1991.

[49] M. Nakazawa, K. Suzuki, H. Kubota, and Y. Kimura, "Self-Q-switching and mode-locking in a 1.53-μm fiber ring laser with saturable absorption in erbium-doped fiber at 4.2K," *Optics Letters*, vol. 18, no. 8, pp. 613–615, 1993.

[50] B. C. Barnett, L. Rahman, M. N. Islam, Y. C. Chen, P. Bhattacharya, W. Riha, K. V. Reddy, A. T. Howe, K. A. Stair, H. Iwamura, S. R. Friberg, and T. Mukai, "High-power erbium-doped fiber laser mode locked by a semiconductor saturable absorber," *Optics Letters*, vol. 20, no. 5, pp. 471–473, 1995.

[51] S. Y. Set, H. Yaguchi, Y. Tanaka, and M. Jablonski, "Laser mode locking using a saturable absorber incorporating carbon nanotubes," *Journal of Lightwave Technology*, vol. 22, no. 1, pp. 51–56, 2004.

[52] S. Yamashita, Y. Inoue, S. Maruyama, Y. Murakami, H. Yaguchi, M. Jablonski, and S. Y. Set, "Saturable absorbers incorporating carbon nanotubes directly synthesized onto substrates and fibers and their application to mode-locked fiber lasers," *Optics Letters*, vol. 29, no. 14, pp. 1581–1583, 2004.

[53] F. Fontana, L. Bossalini, P. Franco, M. Midrio, M. Romagnoli, and S. Wabnitz, "Self-starting sliding-frequency fiber soliton laser," *Electronics Letters*, vol. 30, no. 4, pp. 321–322, 1994.

[54] M. E. Fermann, F. Haberl, M. Hofer, and H. Hochreiter, "Nonlinear amplifying loop mirror," *Optics Letters*, vol. 15, no. 13, pp. 752–754, 1990.

[55] V. J. Matsas, T. P. Newson, D. J. Richardson, and D. N. Payne, "Self-starting passively mode-locked fiber ring soliton laser exploiting nonlinear polarization rotation," *Electronics Letters*, vol. 28, no. 15, pp. 1391–1393, 1992.

[56] V. J. Matsas, T. P. Newson, and M. N. Zervas, "Self-starting passively mode-locked fiber ring laser exploiting nonlinear polarization switching," *Optics Communications*, vol. 92, no. 1-3, pp. 61–66, 1992.

[57] U. Keller, "Recent developments in compact ultrafast lasers," *Nature*, vol. 424, no. 6950, pp. 831–838, 2003.

[58] U. Keller, K. J. Weingarten, F. X. Kartner, D. Kopf, B. Braun, I. D. Jung, R. Fluck, C. Honninger, N. Matuschek, and J. A. derAu, "Semiconductor saturable absorber mirrors (SESAM's) for femtosecond to nanosecond pulse generation in solid-state lasers," *IEEE Journal of Selected Topics in Quantum Electronics*, vol. 2, no. 3, pp. 435–453, 1996.

[59] E. A. Desouza, C. E. Soccolich, W. Pleibel, R. H. Stolen, J. R. Simpson, and D. J. Digiovanni, “Saturable absorber modelocked polarization-maintaining erbium-doped fiber laser,” *Electronics Letters*, vol. 29, no. 5, pp. 447–449, 1993.

[60] M. Guina, N. Xiang, A. Vainionp, O. G. Okhotnikov, T. Sajavaara, and J. Keinonen, “Self-starting stretched-pulse fiber laser mode locked and stabilized with slow and fast semiconductor saturable absorbers,” *Optics Letters*, vol. 26, no. 22, pp. 1809–1811, 2001.

[61] J. H. V. Price, *The development of high power, pulsed fiber laser systems and their applications.* PhD thesis, University of Southampton, UK, 2003.

[62] M. Guina, N. Xiang, and O. G. Okhotnikov, “Stretched-pulse fiber lasers based on semiconductor saturable absorbers,” *Applied Physics B-Lasers and Optics*, vol. 74, pp. S193–S200, 2002.

[63] A. Chong, W. H. Renninger, and F. W. Wise, “All-normal-dispersion femtosecond fiber laser with pulse energy above 20 nJ,” *Optics Letters*, vol. 32, no. 16, pp. 2408–2410, 2007.

[64] S. M. J. Kelly, “Characteristic side-band instability of periodically amplified average soliton,” *Electronics Letters*, vol. 28, no. 8, pp. 806–807, 1992.

[65] H. A. Haus, E. P. Ippen, and K. Tamura, “Additive-pulse modelocking in fiber lasers,” *IEEE Journal of Quantum Electronics*, vol. 30, no. 1, pp. 200–208, 1994.

[66] M. E. Fermann, K. Sugden, and I. Bennion, “Generation of 10 nJ picosecond pulses from a modelocked fiber laser,” *Electronics Letters*, vol. 31, no. 3, pp. 194–195, 1995.

[67] K. Tamura, E. P. Ippen, H. A. Haus, and L. E. Nelson, “77-fs pulse generation from a stretched-pulse mode-locked all-fiber ring laser,” *Optics Letters*, vol. 18, no. 13, pp. 1080–1082, 1993.

[68] V. I. Kruglov, A. C. Peacock, J. D. Harvey, and J. M. Dudley, “Self-similar propagation of parabolic pulses in normal-dispersion fiber amplifiers,” *Journal of the Optical Society of America B-Optical Physics*, vol. 19, no. 3, pp. 461–469, 2002.

[69] V. I. Kruglov, A. C. Peacock, and J. D. Harvey, “Exact self-similar solutions of the generalized nonlinear schrödinger equation with distributed coefficients,” *Physical Review Letters*, vol. 90, no. 11, 2003.

[70] J. R. Buckley, F. W. Wise, F. O. Ilday, and T. Sosnowski, “Femtosecond fiber lasers with pulse energies above 10 nJ,” *Optics Letters*, vol. 30, no. 14, pp. 1888–1890, 2005.

[71] A. Ruehl, H. Hundertmark, D. Wandt, C. Fallnich, and D. Kracht, “0.7 W all-fiber erbium oscillator generating 64 fs wave breaking-free pulses,” *Optics Express*, vol. 13, no. 16, pp. 6305–6309, 2005.

[72] D. J. Taylor, S. E. Harris, S. T. K. Nieh, and T. W. Hansch, “Electronic tuning of a dye laser using acousto-optic filter,” *Applied Physics Letters*, vol. 19, no. 8, pp. 269–271, 1971.

[73] F. V. Kowalski, S. J. Shattil, and P. D. Hale, “Optical pulse generation with a frequency shifted feedback laser,” *Applied Physics Letters*, vol. 53, no. 9, pp. 734–736, 1988.

[74] M. Stellpflug, G. Bonnet, B. W. Shore, and K. Bergmann, “Dynamics of frequency shifted feedback lasers: simulation studies,” *Optics Express*, vol. 11, no. 17, pp. 2060–2080, 2003.

[75] D. O. Culverhouse, D. J. Richardson, T. A. Birks, and P. S. J. Russell, “All-fiber sliding-frequency Er^{3+}/yb^{3+} soliton laser,” *Optics Letters*, vol. 20, no. 23, pp. 2381–2383, 1995.

[76] W. Streifer and J. R. Whinnery, “Analysis of a dye laser tuned by acousto-optic filter,” *Applied Physics Letters*, vol. 17, no. 8, pp. 335–337, 1970.

[77] I. C. M. Littler, H. M. Keller, U. Gaubatz, and K. Bergmann, “Velocity control and cooling of an atomic-beam using a modeless laser,” *Zeitschrift Fur Physik D-Atoms Molecules and Clusters*, vol. 18, no. 4, pp. 307–308, 1991.

[78] V. V. Ogurtsov, V. M. Khodakovskyy, L. P. Yatsenko, B. W. Shore, G. Bonnet, and K. Bergmann, “An all-fiber frequency-shifted feedback laser for optical ranging; signal variation with distance,” *Optics Communications*, vol. 281, no. 6, pp. 1679–1685, 2008.

[79] L. P. Yatsenko, B. W. Shore, and K. Bergmann, “An intuitive picture of the physics underlying optical ranging using frequency shifted feedback lasers seeded by a phase-modulated field,” *Optics Communications*, vol. 282, no. 11, pp. 2212–2216, 2009.

[80] O. G. Okhotnikov, “Multiwavelength picosecond frequency-shifted feedback laser with pulse control by a shaped-gain fiber amplifier,” *Optics Letters*, vol. 23, no. 18, pp. 1459–1461, 1998.

[81] A. Bellemare, M. Sek, M. Rochette, S. LaRochelle, and M. Tu, “Room temperature multifrequency erbium-doped fiber lasers anchored on the ITU frequency grid,” *J. Lightwave Technol.*, vol. 18, no. 6, p. 825, 2000.

[82] J. N. Maran, S. LaRochelle, and P. Besnard, “Erbium-doped fiber laser simultaneously mode locked on more than 24 wavelengths at room temperature,” *Optics Letters*, vol. 28, no. 21, pp. 2082–2084, 2003.

[83] C. S. Jun and B. Y. Kim, "Mode-locking and Q-switching in multi-wavelength fiber ring laser using low frequency phase modulation," *Optics Express*, vol. 19, no. 7, pp. 6298–6303, 2011.

[84] S. K. Kim, M. J. Chu, and J. H. Lee, "Wideband multiwavelength erbium-doped fiber ring laser with frequency shifted feedback," *Optics Communications*, vol. 190, no. 1-6, pp. 291–302, 2001.

[85] M. Romagnoli, S. Wabnitz, P. Franco, M. Midrio, F. Fontana, and G. E. Town, "Tunable erbium ytterbium fiber sliding-frequency soliton laser," *Journal of the Optical Society of America B-Optical Physics*, vol. 12, no. 1, pp. 72–76, 1995.

[86] M. Romagnoli, S. Wabnitz, P. Franco, M. Midrio, L. Bossalini, and F. Fontana, "Role of dispersion in pulse emission from a sliding-frequency fiber laser," *Journal of the Optical Society of America B-Optical Physics*, vol. 12, no. 5, pp. 938–944, 1995.

[87] S. U. Alam and A. B. Grudinin, "Tunable picosecond frequency-shifted feedback fiber laser at 1550 nm," *IEEE Photonics Technology Letters*, vol. 16, no. 9, pp. 2012–2014, 2004.

[88] N. G. R. Broderick, H. L. Offerhaus, D. J. Richardson, and R. A. Sammut, "Power scaling in passively mode-locked large-mode area fiber lasers," *IEEE Photonics Technology Letters*, vol. 10, no. 12, pp. 1718–1720, 1998.

[89] J. Porta, A. B. Grudinin, Z. J. Chen, J. D. Minelly, and N. J. Traynor, "Environmentally stable picosecond ytterbium fiber laser with a broad tuning range," *Optics Letters*, vol. 23, no. 8, pp. 615–617, 1998.

[90] J. M. Sousa and O. G. Okhotnikov, "Short pulse generation and control in er-doped frequency-shifted-feedback fibre lasers," *Optics Communications*, vol. 183, no. 1-4, pp. 227–241, 2000.

[91] L. Lefort, A. Albert, V. Couderc, and A. Barthelemy, "Highly stable 68-fs pulse generation from a stretched-pulse yb^{3+}-doped fiber laser with frequency shifted feedback," *IEEE Photonics Technology Letters*, vol. 14, no. 12, pp. 1674–1676, 2002.

[92] A. M. Heidt, J. P. Burger, J. N. Maran, and N. Traynor, "High power and high energy ultrashort pulse generation with a frequency shifted feedback fiber laser," *Optics Express*, vol. 15, no. 24, pp. 15892–15897, 2007.

[93] M. P. Nikodem, E. Kluzniak, and K. Abramski, "Wavelength tunability and pulse duration control in frequency shifted feedback er-doped fiber lasers," *Opt. Express*, vol. 17, no. 5, pp. 3299–3304, 2009.

[94] P. D. Hale and F. V. Kowalski, “Output characterization of a frequency shifted feedback laser - theory and experiment,” *IEEE Journal of Quantum Electronics*, vol. 26, no. 10, pp. 1845–1851, 1990.

[95] C. C. Cutler, “Why does linear-phase shift cause mode-locking,” *IEEE Journal of Quantum Electronics*, vol. 28, no. 1, pp. 282–288, 1992.

[96] L. F. Mollenauer, J. P. Gordon, and S. G. Evangelides, “The sliding-frequency guiding filter - an improved form of soliton jitter control,” *Optics Letters*, vol. 17, no. 22, pp. 1575–1577, 1992.

[97] C. M. de Sterke and M. J. Steel, “Simple model for pulse formation in lasers with a frequency-shifting element and nonlinearity,” *Optics Communications*, vol. 117, no. 5-6, pp. 469–474, 1995.

[98] G. Bonnet, S. Balle, T. Kraft, and K. Bergmann, “Dynamics and self-modelocking of a titanium-sapphire laser with intracavity frequency shifted feedback,” *Optics Communications*, vol. 123, no. 4-6, pp. 790–800, 1996.

[99] D. Y. Tang, L. M. Zhao, B. Zhao, and A. Q. Liu, “Mechanism of multisoliton formation and soliton energy quantization in passively mode-locked fiber lasers,” *Physical Review A*, vol. 72, no. 4, p. 043816, 2005.

[100] M. Nakazawa, E. Yoshida, and Y. Kimura, “Low threshold, 290-fs erbium-doped fiber laser with a nonlinear amplifying loop mirror pumped by ingaasp laser-diodes,” *Applied Physics Letters*, vol. 59, no. 17, pp. 2073–2075, 1991.

[101] Y. Kodama and S. Wabnitz, “Analysis of soliton stability and interactions with sliding filters,” *Optic Letters*, vol. 19, no. 3, p. 162, 1994.

[102] L. P. Yatsenko, B. W. Shore, and K. Bergmann, “Coherence in the output spectrum of frequency shifted feedback lasers,” *Optics Communications*, vol. 282, no. 2, pp. 300–309, 2009.

[103] K. Nakamura, T. Miyahara, M. Yoshida, T. Hara, and H. Ito, “A new technique of optical ranging by a frequency-shifted feedback laser,” *IEEE Photonics Technology Letters*, vol. 10, no. 12, pp. 1772–1774, 1998.

[104] Y. Kodama and A. Hasegawa, “Generation of asymptotically stable optical solitons and suppression of the gordon–haus effect,” *Optics Letters*, vol. 17, no. 1, pp. 31–33, 1992.

[105] A. Hasegawa and Y. Kodama, “Guiding-center soliton in fibers with periodically varying dispersion,” *Optics Letters*, vol. 16, no. 18, pp. 1385–1387, 1991.

[106] Y. Kodama, M. Romagnoli, and S. Wabnitz, “Soliton stability and interactions in fibre lasers,” *Electronics Letters*, vol. 28, pp. 1981 –1983, oct. 1992.

[107] C. R. Giles and E. Desurvire, “Modeling erbium-doped fiber amplifiers,” *Journal of Lightwave Technology*, vol. 9, no. 2, pp. 271–283, 1991.

[108] E. Desourvire, C. Giles, and J. Simpson, *Erbium doped fiber amplifiers. Principles and Applications.* New Jersey: Wiley & Sons, —2002—.

[109] J. D. Lambert, *Numerical methods for ordinary differential systems: the initial value problem.* New York, NY, USA: John Wiley & Sons, Inc., —1991—.

[110] U. Keller, D. A. B. Miller, G. D. Boyd, T. H. Chiu, J. F. Ferguson, and M. T. Asom, “Solid-state low-loss intracavity saturable absorber for Nd-YLF lasers - an antiresonant semiconductor fabry-perot saturable absorber,” *Optics Letters*, vol. 17, no. 7, pp. 505–507, 1992.

[111] O. G. Okhotnikov, L. Gomes, N. Xiang, T. Jouhti, and A. B. Grudinin, “Mode-locked ytterbium fiber laser tunable in the 980-1070-nm spectral range,” *Optics Letters*, vol. 28, no. 17, pp. 1522–1524, 2003.

[112] M. Rusu, S. Karirinne, M. Guina, A. B. Grudinin, and O. G. Okhotnikov, “Femtosecond neodymium-doped fiber laser operating in the 894-909-nm spectral range,” *Photonics Technology Letters, IEEE*, vol. 16, no. 4, pp. 1029–1031, 2004.

[113] R. Gumenyuk, I. Vartiainen, H. Tuovinen, and O. G. Okhotnikov, “Dissipative dispersion-managed soliton 2 μ m thulium/holmium fiber laser,” *Optics Letters*, vol. 36, no. 5, pp. 609–611, 2011.

[114] M. Jiang, G. Sucha, M. E. Fermann, J. Jimenez, D. Harter, M. Dagenais, S. Fox, and Y. Hu, “Nonlinearly limited saturable-absorber mode locking of an erbium fiber laser,” *Optics Letters*, vol. 24, no. 15, pp. 1074–1076, 1999.

[115] A. Rutz, V. Liverini, R. Grange, M. Haiml, S. Schn, and U. Keller, “Parameter tunable gainnas saturable absorbers for mode locking of solid-state lasers,” *Journal of Crystal Growth*, vol. 301-302, no. 0, pp. 570–574, 2007.

[116] O. G. Okhotnikov, T. Jouhti, J. Konttinen, S. Karirinne, and M. Pessa, “1.5 μm monolithic GaInNAs semiconductor saturable-absorber mode locking of an erbium fiber laser,” *Optics Letters*, vol. 28, no. 5, pp. 364–366, 2003.

[117] F. X. Kartner, J. A. D. Au, and U. Keller, “Mode-locking with slow and fast saturable absorbers - what’s the difference?,” *IEEE Journal of Selected Topics in Quantum Electronics*, vol. 4, no. 2, pp. 159–168, 1998.

[118] J. J. McFerran, L. Nenadovic, W. C. Swann, J. B. Schlager, and N. R. Newbury, “A passively mode-locked fiber laser at 1.54 μm with a fundamental repetition frequency reaching 2 ghz,” *Optics Express*, vol. 15, no. 20, pp. 13155–13166, 2007.

[119] C. Honninger, R. Paschotta, F. Morier-Genoud, M. Moser, and U. Keller, “Q-switching stability limits of continuous-wave passive mode locking,” *Journal of the Optical Society of America B-Optical Physics*, vol. 16, no. 1, pp. 46–56, 1999.

[120] B. O. Products, “http://www.batop.de/products/products.html,” June 2010.

[121] H. A. Haus, E. P. Ippen, and K. Tamura, “Additive-pulse modelocking in fiber lasers,” *Quantum Electronics, IEEE Journal of*, vol. 30, no. 1, pp. 200–208, 1994.

[122] S. M. J. Kelly, K. Smith, K. J. Blow, and N. J. Doran, “Average soliton dynamics of a high-gain erbium fiber laser,” *Optics Letters*, vol. 16, no. 17, pp. 1337–1339, 1991.

[123] C. D. Brooks and F. Di Teodoro, “Multimegawatt peak-power, single-transverse-mode operation of a 100 mu m core diameter, yb-doped rodlike photonic crystal fiber amplifier,” *Applied Physics Letters*, vol. 89, no. 11, 2006.

[124] J. Limpert, F. Roser, D. N. Schimpf, E. Seise, T. Eidam, S. Hadrich, J. Rothhardt, C. J. Misas, and A. Tunnermann, “High repetition rate gigawatt peak power fiber laser-systems: Challenges, design, and experiment,” *IEEE Journal of Selected Topics in Quantum Electronics*, vol. 15, no. 1, pp. 159–169, 2009.

[125] A. Tünnermann, T. Schreiber, and J. Limpert, “Fiber lasers and amplifiers: an ultrafast performance evolution,” *Appl. Opt.*, vol. 49, no. 25, pp. F71–F78, 2010.

[126] N. G. R. Broderick, D. J. Richardson, D. Taverner, J. E. Caplen, L. Dong, and M. Ibsen, “High-power chirped-pulse all-fiber amplification system based on large-mode-area fiber gratings,” *Optics Letters*, vol. 24, no. 8, pp. 566–568, 1999.

[127] M. E. Fermann, V. I. Kruglov, B. C. Thomsen, J. M. Dudley, and J. D. Harvey, “Self-similar propagation and amplification of parabolic pulses in optical fibers,” *Physical Review Letters*, vol. 84, no. 26, pp. 6010–6013, 2000.

[128] J. Limpert, A. Liem, M. Reich, T. Schreiber, S. Nolte, H. Zellmer, A. Tünnermann, J. Broeng, A. Petersson, and C. Jakobsen, “Low-nonlinearity single-transverse-mode ytterbium-doped photonic crystal fiber amplifier,” *Optics Express*, vol. 12, no. 7, pp. 1313–1319, 2004.

[129] L. Dong, J. Li, and X. Peng, “Bend-resistant fundamental mode operation in ytterbium-doped leakage channel fibers with effective areas up to 3160 m2,” *Optics Express*, vol. 14, no. 24, pp. 11512–11519, 2006.

[130] J. Limpert, O. Schmidt, J. Rothhardt, F. Rser, T. Schreiber, A. Tünnermann, S. Ermeneux, P. Yvernault, and F. Salin, “Extended single-mode photonic crystal fiber lasers,” *Optics Express*, vol. 14, no. 7, pp. 2715–2720, 2006.

[131] L. Chi-Hung, C. Guoqing, L. Natasha, G. Almantas, G. Doug, J. Nick, and T. Kanishka, “Effectively single-mode chirally-coupled core fiber,” OSA Technical Digest Series (CD), p. ME2, Optical Society of America, 2007.

[132] P. Dupriez, A. Piper, A. Malinowski, J. K. Sahu, M. Ibsen, B. C. Thomsen, Y. Jeong, L. M. B. Hickey, M. N. Zervas, J. Nilsson, and D. J. Richardson, “High average power, high repetition rate, picosecond pulsed fiber master oscillator power amplifier source seeded by a gain-switched laser diode at 1060 nm,” *IEEE Photonics Technology Letters*, vol. 18, no. 9-12, pp. 1013–1015, 2006.

[133] F. Helmchen and W. Denk, “Deep tissue two-photon microscopy,” *Nat Meth*, vol. 2, no. 12, pp. 932–940, 2005.

[134] K. K. Chen, S. U. Alam, J. H. V. Price, J. R. Hayes, D. J. Lin, A. Malinowski, C. Codemard, D. Ghosh, M. Pal, S. K. Bhadra, and D. J. Richardson, “Picosecond fiber mopa pumped supercontinuum source with 39 w output power,” *Optics Express*, vol. 18, no. 6, pp. 5426–5432, 2010.

[135] G. P. Agrawal, “Amplification of ultrashort solitons in erbium-doped fiber amplifiers,” *IEEE Photonics Technology Letters*, vol. 2, no. 12, pp. 875–877, 1990.

[136] W. Hodel, J. Schtz, and H. P. Weber, “Limits to the amplification efficiency of ultrashort fundamental solitons using er-doped fibers,” *Optics Communications*, vol. 88, no. 23, pp. 173–179, 1992.

[137] M. Horowitz, Y. Barad, and Y. Silberberg, “Noiselike pulses with a broadband spectrum generated from an erbium-doped fiber laser,” *Optics Letters*, vol. 22, no. 11, pp. 799–801, 1997.

[138] M. Horowitz and Y. Silberberg, “Control of noiselike pulse generation in erbium-doped fiber lasers,” *Ieee Photonics Technology Letters*, vol. 10, no. 10, pp. 1389–1391, 1998.

[139] J. U. Kang, “Broadband quasi-stationary pulses in mode-locked fiber ring laser,” *Optics Communications*, vol. 182, no. 4-6, pp. 433–436, 2000.

[140] L. M. Zhao, D. Y. Tang, and J. Wu, “Gain-guided soliton in a positive group-dispersion fiber laser,” *Optics Letters*, vol. 31, no. 12, pp. 1788–1790, 2006.

[141] L. M. Zhao, D. Y. Tang, J. Wu, X. Q. Fu, and S. C. Wen, “Noise-like pulse in a gain-guided soliton fiber laser,” *Optics Express*, vol. 15, no. 5, pp. 2145–2150, 2007.

[142] L. M. Zhao, D. Y. Tang, T. H. Cheng, H. Y. Tam, and C. Lu, “120 nm bandwidth noise-like pulse generation in an erbium-doped fiber laser,” *Optics Communications*, vol. 281, no. 1, pp. 157–161, 2008.

[143] D. J. Lei, H. Yang, H. Dong, S. C. Wen, H. W. Xu, and J. G. Zhang, "Effect of birefringence on the bandwidth of noise-like pulse in an erbium-doped fiber laser," *Journal of Modern Optics*, vol. 56, no. 4, pp. 572–576, 2009.

[144] O. Pottiez, R. Grajales-Coutino, B. Ibarra-Escamilla, E. A. Kuzin, and J. C. Hernandez-Garcia, "Adjustable noiselike pulses from a figure-eight fiber laser," *Applied Optics*, vol. 50, no. 25, pp. E24–E31, 2011.

[145] D. Derickson, *Fiber optic test and measurement.* New Jersey: Prentice Hall PTR, —1998—.

[146] K. L. Corwin, N. R. Newbury, J. M. Dudley, S. Coen, S. A. Diddams, B. R. Washburn, K. Weber, and R. S. Windeler, "Fundamental amplitude noise limitations to supercontinuum spectra generated in a microstructured fiber," *Applied Physics B-Lasers and Optics*, vol. 77, no. 2-3, pp. 269–277, 2003.

[147] S. Shin, U. Sharma, H. H. Tu, W. Jung, and S. A. Boppart, "Characterization and analysis of relative intensity noise in broadband optical sources for optical coherence tomography," *IEEE Photonics Technology Letters*, vol. 22, no. 14, pp. 1057–1059, 2010.

[148] K. N. Wong, *Broadband sources and fibre delay line for the functionality enhancement of optical coherence tomography application.* PhD thesis, University of Southampton, UK, 2007.

[149] K. Tamura, E. P. Ippen, and H. A. Haus, "Pulse dynamics in stretched-pulse fiber lasers," *Applied Physics Letters*, vol. 67, no. 2, pp. 158–160, 1995.

[150] M. Uebernickel, R. Guther, G. Blume, C. Fiebig, K. Paschke, and G. Erbert, "Study of the properties of the shg with diode lasers," *Applied Physics B-Lasers and Optics*, vol. 99, no. 3, pp. 457–464, 2010.

[151] A. Unterhuber, B. Povazay, K. Bizheva, B. Hermann, H. Sattmann, A. Stingl, T. Le, M. Seefeld, R. Menzel, M. Preusser, H. Budka, C. Schubert, H. Reitsamer, P. K. Ahnelt, J. E. Morgan, A. Cowey, and W. Drexler, "Advances in broad bandwidth light sources for ultrahigh resolution optical coherence tomography," *Physics in Medicine and Biology*, vol. 49, no. 7, pp. 1235–1246, 2004.